Wideband Balun Design for the Pyramidal Sinuous Antenna

by

Michael Johnston

Thesis submitted in partial fulfilment of the requirements for the degree of Master of Engineering in Electrical and Electronic Engineering in the Department of Electrical and Electronic Engineering at the University of Stellenbosch

Supervisor: Dr. C. Van Niekerk

Co-supervisor: Prof. D.I.L. de Villiers

April 2019

Declaration

By submitting this thesis electronically, I declare that the entirety of the work contained therein is my own, original work, that I am the sole author thereof (save to the extent explicitly otherwise stated), that reproduction and publication thereof by Stellenbosch University will not infringe any third party rights and that I have not previously in its entirety or in part submitted it for obtaining any qualification.

Date: April **2019**

Abstract

This thesis presents the design of wideband baluns for integration with the pyramidal sinuous antenna. Two different realizations of the Marchand balun are studied, namely a planar coupled-line balun and a rectangular coaxial balun.

The planar balun implementation makes use of ground plane apertures to enhance the coupling coefficient of the coupled-line sections, so that higher bandwidths can be achieved compared to standard implementations. It is designed to be able to accommodate a single or dual-linearly polarized sinuous antenna. The designed prototype displays a bandwidth ratio of 3:1 with a 50-300 Ω single-ended to differential impedance transformation. The simulated return loss is better than 10 dB, and the simulated insertion loss is better than 0.84 dB. The amplitude balance is better than ±0.2 dB across most of the band, and the phase balance is better than ±2° across half the band. The performance of the manufactured prototype is shown to be consistent with simulated predictions.

The coaxial implementation makes use of a shunted resonate line to provide frequency independent unbalanced current cancellation, and is able to achieve a bandwidth ratio of about 5:1 with a 50-300 Ω singled-ended to differential impedance transformation. The return loss of the final coaxial design is better than 10 dB with an insertion loss better than 0.91 dB. The amplitude balance is better than ±0.2 dB and the phase balance is better than ±1.5° across the entire band. The performance of the manufactured prototype did not agree with simulated predictions and therefore a short follow-up study is conducted explaining the differing results.

Performance of the prototype baluns is further verified through simulated integration with the single-linearly polarized pyramidal sinuous antenna. Both balun implementations integrate with the antenna in a straightforward manner with relatively small reflections. Reasonably symmetric radiation patterns are achieved for the planar integration with some variation in the reported gain at broadside. Symmetric radiation patterns are also achieved across the band for the coaxial integration, but better consistency is reported for the gain at broadside.

Opsomming

Hierdie tesis ondersoek die ontwerp van breëband baluns vir integrasie met die piramidale sinuous antenna. Twee verskillende realiserings van die Marchand balun word bestudeer, naamlik ‘n planêre gekoppelde lyn balun en ‘n reghoekige koaksiale balun.

Die implementering van die planêre balun maak gebruik van slote op die grondvlak om die koppeling koëffisiënt van die gekoppelde lyn seksies te versterk. Hoër bandwydtes kan met hierdie implementering bereik word, in vergelyking met standaard implementerings. Dit word ontwerp om ‘n enkel of duale-linière gepolariseerde sinuous antenna te akkommodeer. Die ontwerpte prototipe toon ‘n bandwydte ratio van 3:1 met ‘n enkel-einde tot differensiële impedansie transformasie van 50-300 Ω. Die gesimuleerde terugkeer verlies is beter as 10 dB, en die gesimuleerde invoer verlies is beter as 0.84 dB. Die amplitude balans is beter as ±0.2 dB oor die meerderheid van die band, en die fase balans is beter as ±2° oor die helfte van die band. Daar word getoon dat die effektiwiteit van die vervaardigde prototipe konsekwent is met gesimuleerde voorspellings.

Die koaksiale implementering maak gebruik van ‘n afgetakte resonante lyn om frekwensie-onafhanklike kansellasie van ongebalanseerde stroom te verseker. Die implementering kan ook ‘n bandwydte ratio van omtrent 5:1 bereik met ‘n 50-300 Ω enkel-einde tot differensiële impedansie transformasie. Die terugkeer verlies van die finale koaksiale ontwerp is beter as 10 dB met ‘n invoer verlies wat beter is as 0.91 dB. Die amplitude balans is beter as ±0.2 dB en die fase balans is beter as ±1.5° oor die totale bandwydte. Die effektiwiteit van die vervaardigde prototipe het nie ooreengestem met die gesimuleerde voorspellings nie en om hierdie rede word ‘n kort opvolgstudie onderneem om die verskil in resultate te ondersoek.

Die effektiwiteit van die prototipe baluns word verder geverifieer deur gesimuleerde integrasie met die enkel-linière gepolariseerde piramidale sinuous antenna. Beide balun implementerings integreer met die antenna op ‘n eenvoudige wyse met relatief min refleksie. Redelike simmetriese stralingspatrone word bereik met die planêre integrasie met ‘n mate van variasie in die gerapporteerde verhoging in die vertikale as. Simmetriese stralingspatrone word ook bereik regoor die band vir die koaksiale integrasie, maar groter konsekwentheid word rapporteer vir die verhoging in die vertikale as.

Acknowledgements

I'd like to extend my heartfelt gratitude to the following people for their invaluable contributions during the course of this project:

- My supervisors, Dr. Carlo Van Niekerk and Prof. Dirk De Villiers, for their guidance, support and willingness to help. Thank you for the enthusiasm and interest shown, and for giving me the freedom to explore various research avenues.
- My parents, Helene and Anthony, for their unwavering love and support. Thank you for being such amazing role models in my life. This would not have been possible without you.
- To Lieze, for everything you've done, and continue to do for me. Your boundless love, advice and encouragement means the world to me. I welcome the constant source of distraction that you provide. Although, I probably would have finished my thesis much sooner!
- To my brother and sister, Chris and Caroline, for your support and advice and for being excellent siblings in general.
- My fellow students in the Radar Lab for their camaraderie and for enabling an enjoyable working environment.
- Special thanks to Mr. Gift Lecholo, Mr. Wessel Croucamp and Mr. Van Eeden for their assistance during the manufacturing process.

I'd also like to extend my gratitude to the organizations that made this project possible. This research was supported by the South African Radio Astronomy Observatory, which is a facility of the National Research Foundation, an agency of the Department of Science and Technology.

Finally, I'd like to thank the City of Cape Town for their financial assistance during the course of my undergraduate studies.

Contents

List of Figures

List of Tables

Chapter 1

Introduction

1.1 Background

The Square Kilometre Array (SKA), as described in [1], is an enormous international project to build the world's largest radio interferometer. The countries involved include Australia, China, Germany, The Netherlands, South Africa and the United Kingdom. The radio telescopes will boast a collecting area over a square kilometre upon completion of the project with unrivalled resolution and sensitivity. Taking advantage of advancements in radio frequency devices and digital processing, it will achieve a sky imaging capacity 10,000 times faster than our current best imaging radio telescopes. The project aims to answer fundamental questions about dark energy, magnetic waves, galaxy evolution and cosmology. To that end, the contribution of researchers and engineers in areas such as wideband antennas, signal transport and networking, high-performance computing and radio frequency interference (RFI) mitigation is critical to the success of the project. The reader may find a more detailed description of the SKA in [2].

The ultra-wideband (UWB) single pixel feeds for reflector antennas being investigated for the SKA include the log periodic dipole array feed [3], the eleven feed [4], the conical sinuous antenna [5] and the Quasi self-complementary (QSC) antenna [6]. In radio astronomy, UWB performance refers to feeds with a bandwidth of more than 2:1, or an octave. The pyramidal sinuous antenna, capable of dual linear or circular polarization, is another UWB pixel feed that displayed promising results [7]. A visual representation of existing conical and pyramidal sinuous feeds is shown in Fig. 1.1.

The initial study of the pyramidal case was expanded in [8]. The focus of the study was on the characterization of the dual-polarized sinuous antenna as a reflector feed. A primitive feeding network was designed to enable characterization of the practical antenna, but further investigation into the development of wideband compact baluns was suggested.

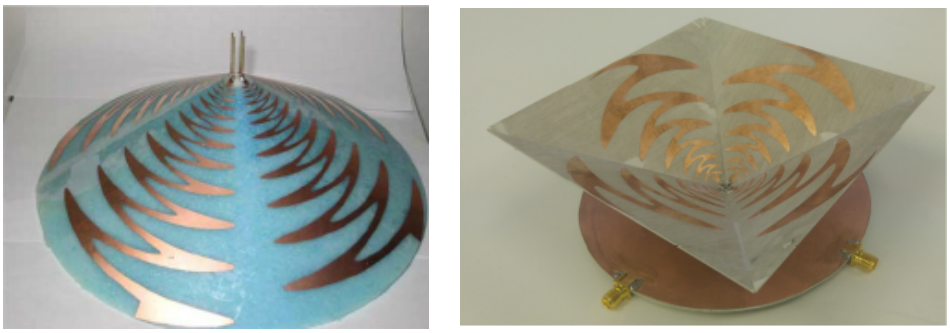

(a) (b)

Figure 1.1: The various forms of the sinuous antenna in (a) The conical sinuous antenna [5]. (b) The pyramidal sinuous antenna [9].

1.2 About this Thesis

The underlying theme for this research is the design and implementation of Marchand baluns with an existing optimized pyramidal sinuous antenna solution. Ultra wideband baluns are desired to match the achievable bandwidth of the antenna. The proposed baluns should be low-loss, compact solutions that integrate with the antenna in a straightforward manner. Successful implementation of a UWB balun for the antenna may lead to improvements in resolution, sensitivity and field-of-view for the entire receiving system. The cost of implementation is also reduced because fewer feeds are then required.

The full-wave model of the dual-polarized sinuous antenna is first generated and analyzed in simulation, so that the radiation characteristics and input impedance can be verified. Next, the analysis, design and implementation of a microstrip coupled-line Marchand balun is considered for the 2 - 6 GHz pyramidal sinuous antenna. The target specifications for the baluns in this work are a return loss better than 10 dB, an insertion loss better than 1 dB and an amplitude and phase balance that ensure symmetric radiation field patterns. The SKA specifies an insertion loss of 0.1 dB [10] to minimize the receiver noise temperature. This can be achieved through the use of cryogenics, but it is outside the scope of this thesis. The design and implementation of a rectangular coaxial Marchand balun is also considered to better match the achievable bandwidth of the antenna. The target specifications for the coaxial case remain the same as for the planar solution. Finally, the designed baluns are simulated in conjunction with the pyramidal sinuous antenna and the results are presented.

The contributions of this thesis are summarized as follows:

- The design and verification of a fourth order rectangular coaxial Marchand balun for integration with a balanced antenna, such as the pyramidal sinuous antenna.
- The design and verification of a prototype compact planar Marchand balun for integration with a balanced antenna such as the pyramidal sinuous antenna. A design procedure for incorporating ground plane modifications to enhance the coupling factor is included.

- Brief study and verification of balun integration techniques for the sinuous antenna.

1.3 Thesis Layout

This thesis starts with an overview of feeding balanced antennas in Chapter 2. Important definitions relating to balun functionality are outlined in this chapter, followed by an overview of existing feed solutions for wideband antennas. Finally, a theoretical overview of the planar sinuous antenna is presented with an emphasis on the feeding procedure.

Chapter 3 extends the theory behind the planar sinuous antenna to the pyramidal antenna case. The differences are explained and new parameters describing the pyramidal case are introduced. A full-wave model of the pyramidal sinuous antenna is generated in CST MWS and its input impedance and radiation patterns are analyzed.

Chapter 4 details the analysis, design and fabrication of a printed coupled-line Marchand balun with ground plane modifications. A separate study of the proposed ground plane modifications is conducted, and the findings are incorporated into the design of the balun. Special consideration is given to the configuration and location of the transmission lines that make up the balun to ensure straightforward integration with the antenna.

Chapter 5 details the analysis, design and fabrication of a rectangular coaxial Marchand balun. It provides better bandwidth and balance capabilities compared to the printed coupled-line balun. Closed-form expressions describing the necessary impedances of the balun are provided, and ideal and full-wave models are designed accordingly. The performance of the simulated model is then confirmed via fabrication and testing.

Chapter 6 builds on the work presented in preceding chapters. Full-wave models of the pyramidal sinuous antennas covering different frequency bands are generated and the designed baluns are tested in combination with the antennas. The simulated performance of the integrated system is analyzed and the effectiveness of the proposed solution is investigated.

Chapter 7 concludes the thesis, providing a short summary of the most notable results, limitations, improvements and some recommendations for future work.

Chapter 2

Literature Study

The two underlying themes of this work relate to the sinuous antenna and how to feed it. Literature relevant to these themes is therefore studied. This is accomplished by first providing a general description of a balun and examining the behaviour of some narrow-band baluns. This is followed by an overview of potential wideband balun candidates commonly found feeding wideband antennas. The benefits and drawbacks of these baluns are discussed and compared. A detailed description of the background, operation and geometry of the planar sinuous antenna is also given, so that a suitable wideband balun may be selected for integration. Concepts relating to the impedance and feeding region of antenna are especially important.

2.1 General Balun Theory

There are two main challenges typically associated with feeding antennas. The first is that antennas generally do not have input impedances that match to a 50 Ω standard feed, like a coaxial cable. Therefore an impedance mismatch occurs between the antenna and feed, resulting in degraded return loss. The second challenge is that there are different types of antennas, namely: unbalanced, also referred to as single-ended, and balanced, also referred to as differential. These antennas need to be excited by corresponding single-ended or differential transmission lines. Examples of balanced and unbalanced transmission lines are shown in Fig. 2.1 and Fig. 2.2 respectively.

The co-planar stripline (CPS) structure shown in Fig. 2.1 has a symmetric structure, and therefore similar impedances along its length and with respect to ground. In contrast, the structures shown in Fig. 2.2a and 2.2b are unbalanced because the impedance of the signal and the return path is different with respect to ground.

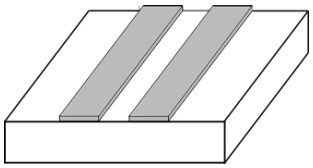

Figure 2.1: Balanced co-planar stripline structure.

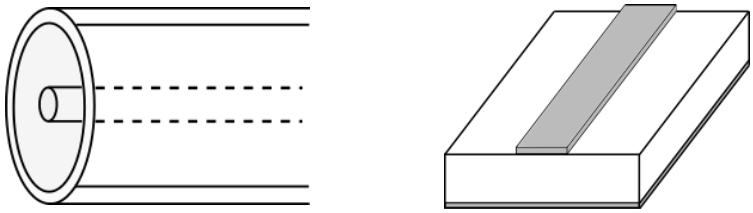

(a) (b)

Figure 2.2: Unbalanced transmission lines. (a) Coaxial line (b) Microstrip line.

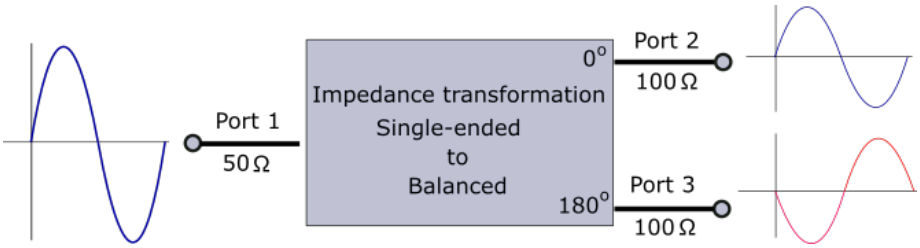

Figure 2.3: Diagram of balun functionality.

A balun, a portmanteau for "balanced-to-unbalanced", is a three-port device that is used to transform an unbalanced transmission line to a balanced transmission line. General balun operation is depicted in Fig. 2.3. The input signal at Port 1 is divided in an equal and anti-phase manner at Port 2 and Port 3. Some baluns are able to provide impedance transformation, but it is not a requirement. A balun is comparable to a Wilkinson power divider, resistive power divider, or quadrature hybrid coupler in that it acts as a -3 dB power divider. The difference is that baluns provide a 180° phase difference between the outputs, while the other power dividers have 0° phase difference, and the coupler has a 90° phase difference. Baluns are key components in devices such as mixers, antenna feeds and push-pull amplifiers.

When a balanced antenna, like a dipole antenna, is fed via an unbalanced transmission line, like coaxial cable, the outside of the outer conductor acts as a separate conductor. The current in the centre conductor of the coaxial flows into the left half of the dipole. The equal and opposite current on the inside of the outer conductor flows partly into the right half of the dipole, and partly along the outside of the outer conductor, causing the imbalance. Balanced feeds are therefore required to excite the antenna arm pairs in an equal magnitude and anti-phase manner.

There are two main issues when balanced antennas are not excited in balanced way: the first is that uncontrolled currents, also known as unbalanced currents, cause radiation of the transmission line itself, in a potentially unexpected direction and/or polarization. Secondly, the imbalance of the current will cause the antennas radiation pattern to change due to the uneven current distribution in the antenna arms. Having an unbalanced transmission line feeding a symmetric antenna is clearly unproductive and highlights the need for a balun.

A basic understanding of baluns and how they operate is important in the context of this thesis. Consequently, some relatively simple balun configurations are investigated and their basic operation is examined. The first balun configuration described in [11] is the sleeve balun shown in Fig. 2.4a. It is identified by a $\lambda/4$ length conducting sleeve surrounding the coaxial line and is shorted at one end. It is connected to a balanced dipole antenna. The operation of the sleeve balun is described below.

The impedance of a shorted lossless transmission with length l line can be written as,

$$Z_{in} = jZ_0 \tan \beta l. \tag{2.1}$$

where Z_0 is the characteristic impedance of the transmission line and β is the propagation constant. If $l = \lambda/4$, it follows that $Z_{in} = \infty$. This high impedance limits or "chokes" the current on the outside of the outer conductor resulting in a balanced system. In other words, the conducting sleeve introduces a high input impedance at the open end of the shorted transmission line which limits the current. Infinitely high impedances are not practically realizable, and therefore real systems will not be perfectly balanced.

The second balun is the quarter-wave coaxial balun configuration which is presented in Fig. 2.4b. It is constructed by connecting an extra quarter-wave coaxial section between the outer conductor of the main coaxial transmission line and the dipole arm. The dipole arm is then connected to the centre conductor of the main transmission line. The additional coaxial section, together with the outer conductor of the main transmission line, form another equivalent transmission line which is shorted at the connection point. Thus, the short circuit is transformed into an infinite impedance which forms a parallel connection with reference to the antenna terminals. The antenna impedance is therefore unaffected by the addition of the coaxial section. The voltages on either side of the dipoles are equal and anti-phase with reference to ground. Hence, equal and opposite currents are induced in the equivalent coaxial section. The current flow on the outer conductor of the main transmission line is effectively cancelled below the shorted connection point by the equal magnitude anti-phase currents in the equivalent coaxial section, resulting in a balanced system.

The baluns described above are suitable for applications above 1 GHz, as implementation at lower frequencies results in inconveniently large structures. However, because these baluns are designed to operate at a single frequency, they are inherently narrowband solutions. These baluns also do not provide impedance transformation, hence they can be labelled as "one-to-one" baluns.

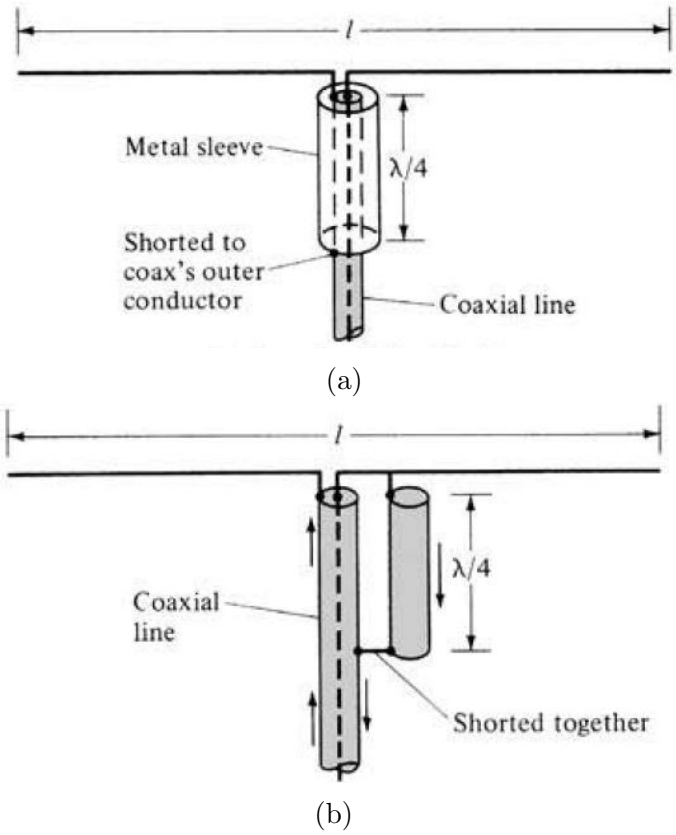

Figure 2.4: Common balun configurations. (a) The sleeve balun (b) The quarter-wave coaxial balun [11].

2.2 Wideband Baluns

The pyramidal sinuous antenna requires a solution with high bandwidth capabilities, while simultaneously providing impedance transformation. The narrowband one-to-one baluns discussed in the previous section do not meet these requirements. Therefore, various wideband baluns are investigated for use with the sinuous antenna. Characterization of balun performance in this work is described in Appendix A.

2.2.1 Tapered Balun

The tapered balun is a wideband balun which gradually converts an unbalanced transmission line to a balanced transmission line over several wavelengths. The structure of a conventional exponentially tapered microstrip balun is shown in Fig. 2.5. The unbalanced microstrip line is systematically tapered to form a balanced parallel line at the balanced side. This balun is derived from the coaxial tapered line implementation where the transition is accomplished by cutting away most of the outer conductor to leave a thin form of a parallel transmission line along with the centre conductor.

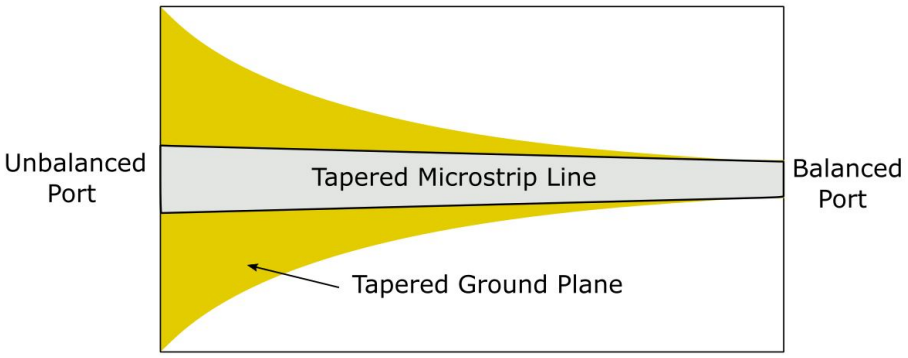

Figure 2.5: Exponentially tapered microstrip balun.

Many different forms of wideband tapered baluns for integration with wideband antennas have been reported in literature. Linear and Klopfenstein tapered solutions are developed for the Eleven feed across the 2-14 GHz band in [12]. However, strong reflections at input port of the antenna lead to degraded return loss. A similar balun was also proposed for the ATA feed in [13]. There are also numerous reported examples of tapered baluns feeding the sinuous antenna [14–16]. The popularity of tapered baluns is in part due its wideband impedance transformation capabilities, as well as its relative ease of integration with balanced antennas.

The main disadvantage of this type of balun is that it has to be electrically long to achieve good balance results [12–16]. This is not ideal for radio receiver applications that require a short path between the antenna and first receiving component, so that the receiver noise temperature can be minimized [17]. The physical size of the tapered balun also makes it cumbersome to cool the device using cryogenics. Custom-made cryogenics are expensive and difficult to come by, so a more compact solution with a short path length is therefore required.

2.2.2 Marchand Balun

The Marchand balun, originally introduced in 1944 [18], is shown in Fig. 2.6. The microwave component is frequently used in broadband double-balanced mixers, push-pull amplifiers and frequency doublers [19]. The wideband potential of Marchand baluns means that it is also often used to feed wideband antennas. Bandwidth ratios of 10:1 or more can be achieved in the coaxial version by careful selection of the balun parameters [20]. Examples of Marchand baluns feeding wideband antennas can be found in [14, 21].

The inherent symmetry of the balun structure facilitates frequency independent balanced operation. The return currents for common-mode excitation of the balanced output lines flow along the inside of the cavity wall and meet at the centre of the structure. These currents will be cancelled due to destructive interference, thus ensuring differential propagation of the balanced output lines.

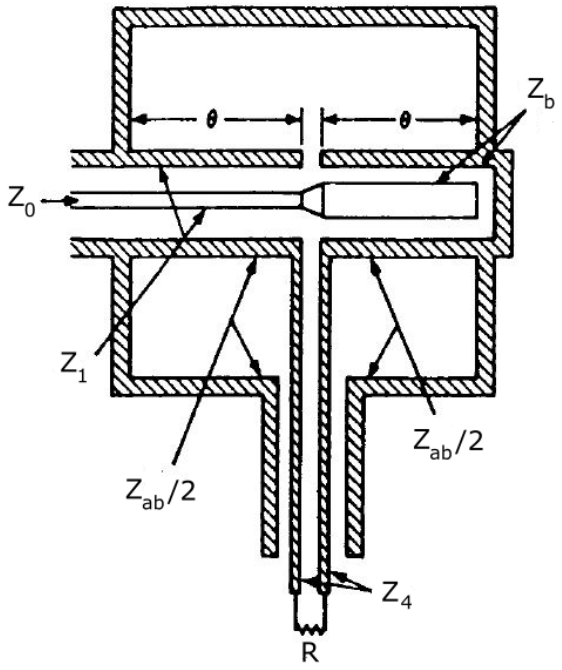

Figure 2.6: Series-connected compensated coaxial Marchand balun [18].

The structure in Fig. 2.6 consists of two inner coaxial lines and a balanced transmission line pair enclosed by a shielded box. The unbalanced coaxial input, Z_0, connects to the first impedance transforming section, Z_1. The centre conductors of Z_1 and the open-circuit stub, Z_b, are joined together at the balun junction, while the respective outer conductors separate and form the balanced transmission line transforming section Z_4. The resonant cavity impedance shunting the junction is given by $Z_{ab}/2$. Optimal performance is achieved for $\theta = \pi/2$, relative to wavelength.

The Marchand balun can also be implemented in planar form using printed circuit board (PCB) technology. The desired configuration of the balun is usually based on the requirements of the application i.e. size requirements, required bandwidth, or integration procedure with other microwave components. Printed implementations have the advantage of being inexpensive and easy to manufacture, as standard PCB printing techniques can be employed. However, they are unable to achieve bandwidths as high as their coaxial counterparts.

A basic microstrip to slotline balun is shown in Fig. 2.7. It consists of a microstrip input, and slotline output which can be tapered into a co-planar stripline for integration with a balanced antenna. Microstrip to slotline balun concepts may be extended to various other planar implementations of the Marchand balun. Symmetric edge, or broadside, coupled-line structures may be employed to achieve mode and impedance transformation required for balun operation. This can be achieved using microstrip coupled lines [19], broadside multi-layer coupled structures [18], or Lange couplers [22].

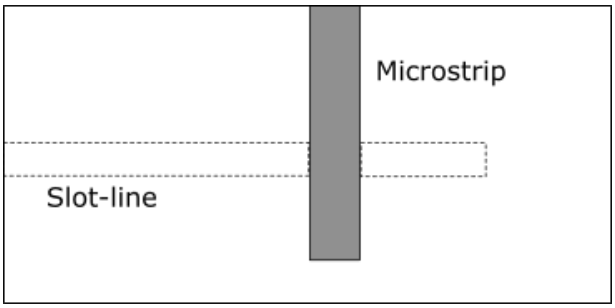

Figure 2.7: Planar microstrip/slotline Marchand balun.

The planar baluns presented in [23] and [24] are also based symmetric coupled-line sections, but additionally, make use of ground plane apertures placed directly underneath coupled-line sections. This enhances the coupling factor, and consequently, the bandwidth. The reported baluns both achieve an approximate bandwidth ratio of 3:1 and exhibit good balance performance.

2.2.3 Phelan Balun

The parallel-connected balun, or Phelan balun [25], is a type of resonant balun derived from the uncompensated coaxial Marchand balun. It may be realized in a variety of different ways as shown by the schematics in Fig. 2.8.

A basic description of the balun is given with reference to Fig. 2.8a. The structure consists of three interconnected coaxial line sections enclosed by a shielded box. The centre conductor of the coaxial input is connected to a solid rod to ensure that the symmetry of the structure is maintained. The outer conductors of the input and top coaxial sections are also joined together. The solid rod is then soldered to the outer conductor of the bottom coaxial output, and connects to the centre conductor of the top output coaxial line section. The centre conductor of the bottom output coaxial section is connected to the outer conductor of the input coaxial section.

The equivalent circuit of the parallel connected balun is shown in Fig. 2.9. Z_{in} is the balun input impedance, R_A and R_B are the input resistances of the parallel connected output cables and Z_C is the characteristic impedance of the cavity. The balanced outputs are shown to be in parallel with the cavity impedance and the balun junction, thus ensuring balanced frequency independent balun operation. If the output coaxial sections are bent together to form a balanced coaxial-line section, then the resistance presented at balun junction simplifies to

$$R = \frac{R_A R_B}{R_A + R_B} = \frac{Z_L}{4}, \tag{2.2}$$

where Z_L is the balanced load impedance.

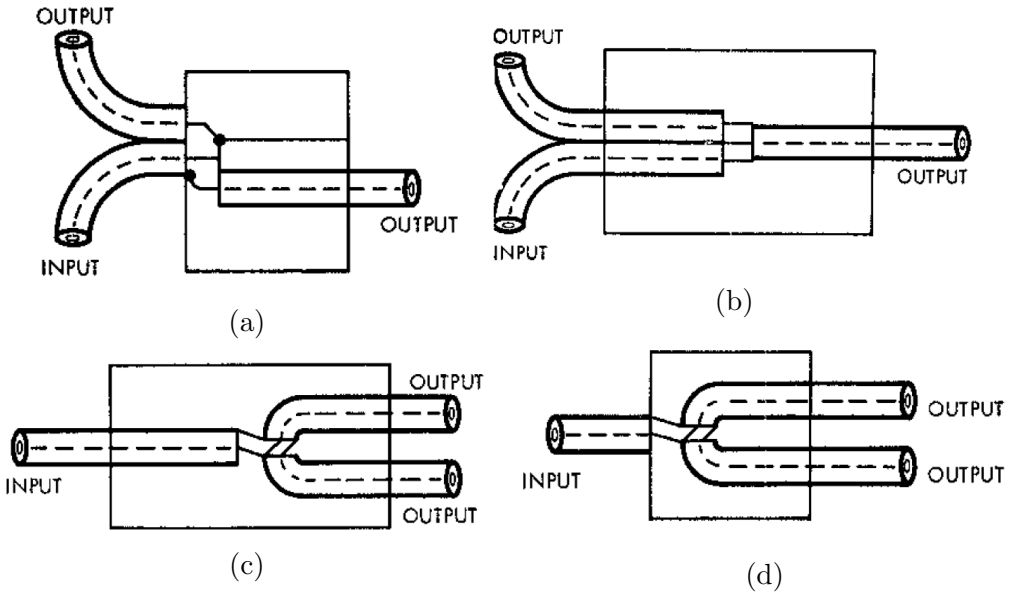

Figure 2.8: Parallel-connected baluns [25]. The different realizations provide flexibility during the design process of feeding a balanced antenna.

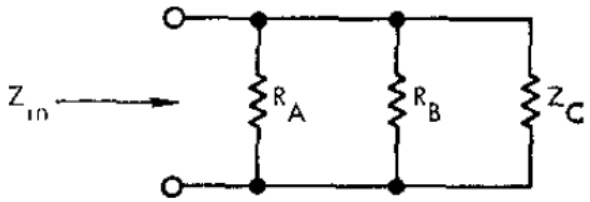

Figure 2.9: Equivalent circuit of a parallel-connected balun [25].

The equation shows that a 4:1 impedance transformation is automatically obtained for parallel-connected baluns. This is useful for feeding wideband, high-impedance balanced antennas like the sinuous. The parallel-connected balun also has approximately four times the bandwidth capability of the series-connected balun for similar cavity impedances [25]. While promising in theory, literature regarding parallel-connected baluns with wideband antennas is scarce, often being overlooked in favour of the series-connected compensated Marchand balun.

2.3 Planar Sinuous Antenna

The planar dual-polarized cavity backed sinuous antenna was invented by R. H. Du Hamel in 1987 [26]. Its inception came as a result of Du Hamel's work relating to frequency independent (FI) and high frequency antennas [27–29]. The sinuous antenna is a log-periodic structure which is defined by angles instead of lengths. It supports dual senses of linear or circular polarization, depending on how the antenna is excited. These qualities

allow it to have a constant input impedance, beam-width and phase centre over a large range of frequencies [5]. Because of this, these antennas are typically used in applications like electronic warfare, radio astronomy and remote sensing [30]. This section starts by introducing concepts relating to FI antennas.

2.3.1 Frequency Independent Antennas

The fundamentals of FI antennas were proposed by Rumsey during the 1950s, and it facilitated the research and discovery of some useful wideband antennas. A frequency independent antenna can be defined as an antenna that retains its properties even after an arbitrary change in scale. This only holds if the scaled structure is identical to the original, or a rotated form of the original [31]. It follows that if the shape of an antenna is entirely determined by angles, then the performance is also independent of frequency. This supports the notion that a change in scale does not influence defining angles of the antenna's shape. A discussion of important aspects relating to FI antennas is presented below.

Truncation Principle

An FI antenna with an infinitesimal feeding region and infinite size could operate over an unlimited band. However, the finite size of practical antennas suggests that FI behaviour only occurs over a limited band. The lowest frequency of operation is determined by the frequency at which the active region is shifted to the outside edge of the antenna. The highest frequency of operation is determined by the size and precision of the feeding region.

Radiation fields are created by surface currents distributed over a finite section of the antenna surface known as the active region. The active region changes as the frequency varies and currents are suppressed beyond the limits of the active region. The truncation principle therefore implies that surface currents approach zero at a certain distance away from the feeding region.

Self-complementary Condition

Antennas with self-complementary structures have constant input impedances which are independent of frequency and shape of the structure [32]. The self-complementary condition states that the interchange of the conducting and non-conducting surfaces of a planar antenna results in a rotated version of the original structure. Volakis [30] states that this rotation must be equal to half of the angular periodicity.

The Log-Periodic Concept

Log-periodicity refers to the logarithmic spacing between consecutive elements in a log-periodic antenna. A log-periodic dipole antenna is shown in Fig. 2.10. It illustrates how the distances and lengths of adjacent dipoles increase with a specified scaling factor.

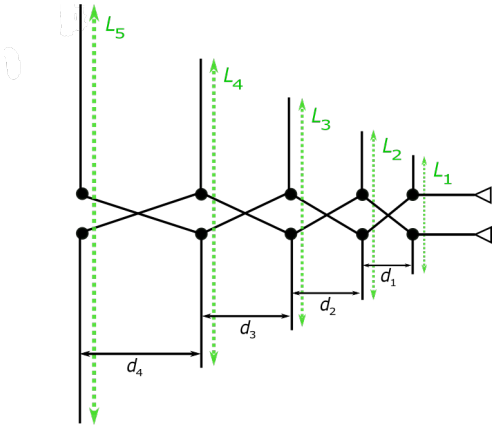

Figure 2.10: Log-periodic dipole antenna.

The scaling factor, τ, is defined as

$$\tau = \frac{L_{n+1}}{L_n} = \frac{d_{n+1}}{d_n}, \tag{2.3}$$

where L_n and d_n are the respective lengths and distances between adjacent dipoles. According to [4], this implies that the electrical properties, such as impedance and radiation pattern, of the antenna are identical at frequencies that are scaled by τ,

$$f_{n+1} = \tau f_n. \tag{2.4}$$

Taking the logarithm of (2.4) gives,

$$\log(f_{n+1}) = \log(f_n) + \log(\tau), \tag{2.5}$$

which shows logarithmic growth by a factor $\log(\tau)$, hence the name log-periodic antenna.

2.3.2 Fundamental Theory

This section reviews the fundamental theory of the planar sinuous antenna. The geometric aspects of the planar case are discussed first, followed by a simple explanation of the antenna's radiation characteristics, bandwidth and input impedance.

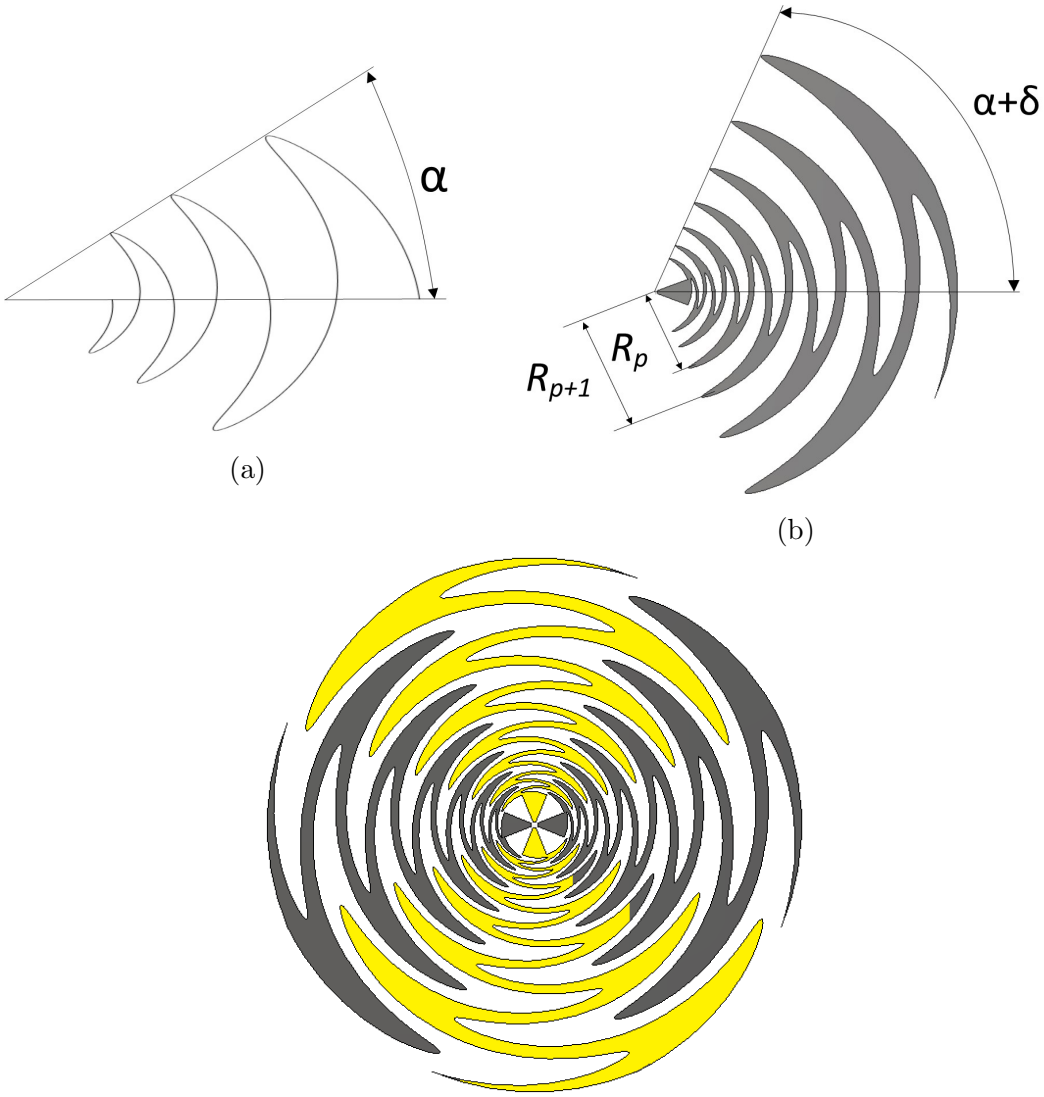

(a) (b) (c)

Figure 2.11: Geometry of the planar sinuous antenna. (a) Planar sinuous curve. (b) Planar sinuous arm. (c) $N = 4$ arm planar sinuous antenna.

The geometry of the planar sinuous antenna is shown in Fig. 2.11. The geometry of the planar sinuous arm in Fig. 2.11b is derived from the sinuous curve in Fig. 2.11a and is given by [26],

$$\phi(r) = (-1)^p \alpha_p \sin\left[\pi \cdot \frac{\ln(r/R_p)}{\ln(\tau)}\right] \pm \delta, \qquad R_{p+1} \leq r \leq R_p, \tag{2.6}$$

where ϕ is the polar angle and r is the radius of the planar curve in cylindrical coordinates.

The radius R_p is given by

$$R_{p+1} = \tau R_p, \qquad 0 \leq \tau \leq 1, \tag{2.7}$$

where τ is the growth rate and can be seen as the scaling ratio between adjacent cells. The growth rate is kept constant in order to achieve a log-periodic frequency independent structure. The angular width of the antenna is denoted by α_p, and the rotation angle is denoted by δ. The thickness of the sinuous arm depends on δ and the sinuous curve is rotated by $\pm\delta$ to form the sinuous arm shown in Fig. 2.11b. The antenna contains an even number of N-arms placed $(360°/N)$ around a centre point. The N sinuous arms each consists of p cells and the innermost, or minimum, radius is then denoted by R_p.

The achievable bandwidth of the sinuous antenna follows from the discussion regarding the truncation principle in Section 2.3.1. The active cells or resonators are given by

$$r(\alpha_p + \delta) \approx \frac{\lambda}{4}, \tag{2.8}$$

where α_p and δ are expressed in radians. Therefore, the length of each resonator, to the bend and back, is approximately equal to $\lambda/2$. The active region of the sinuous antenna can then be defined as a circular band with a circumference of about one wavelength. This is illustrated in Fig. 2.12 which shows how the active region recedes as the frequency increases. The low and high-frequency cutoff radii, R_l and R_h, represent in the inner and outer radii of the structure and can be established by making use of (2.8):

$$R_h = \frac{\lambda_h}{4(\alpha_p + \delta)}, \tag{2.9}$$

$$R_l = \frac{\lambda_l}{4(\alpha_p + \delta)}. \tag{2.10}$$

R_l is normally extended by approximately 20% beyond the low-frequency cutoff before truncation. This allows the low-frequency band to form properly and reduces the influence of edge effects. Similarly, R_h is generally reduced by a factor of two to provide a transition region between the feed terminals and the first active region [9, 33, 34]. The general performance, mainly the directivity and return loss, of the antenna deteriorates quickly outside the specified frequency range.

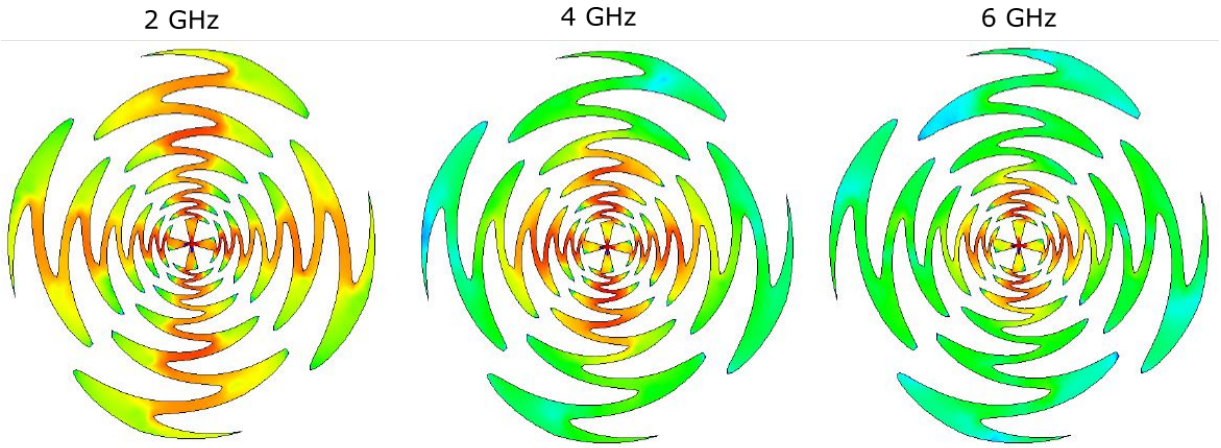

Figure 2.12: Active cell regions shown as a function of frequency [9]. All cell regions are active at the lowest frequency.

A self-complementary sinuous antenna with $N = 4$ is shown in Fig. 2.11c. The condition of self-complementarity for an N-arm sinuous structure is $\delta = \pi/2N$ [5]. The frequency independent input impedance, Z_m, with respect to ground, for a self-complementary antenna is given by Deschamps formula [35],

$$Z_m = \frac{30\pi}{\sin(\frac{m\pi}{N})}, \tag{2.11}$$

where Z_m is equal to 133 Ω for a four-arm antenna which is excited in mode $m = 1$. The voltage excitation for a normal mode is defined by

$$V_{n,m} = A_m e^{j2\pi mn/N}, \tag{2.12}$$

where $n = 1, 2.., N$ relates to the arm number, $m = 1, 2.., (N-1)$ is the mode number and A_m is the excitation amplitude of the mode m. Different radiation patterns are achieved by varying the mode number. Applying the same mode number to each arm results in a symmetric radiation pattern.

Mode m=1 is the only mode with a broadside radiating component, while all other modes have a null on broadside, with each higher-order mode peaking further from the null [30]. Thus, the antenna is driven in mode m=1 for radio receiver applications. If each arm is excited in mode m=1, the excitation phases according to (2.12) will be [90° ; 180°; 270° ; 360°]. The results indicate a 180° phase difference between opposite pairs of arms which means they need to be driven differentially.

It is now convenient to define differential impedance for a balanced transmission line pair that feeds a single sinuous arm pair. According to [9], the differential impedance of symmetric uncoupled-lines is given by

$$Z_{diff} = 2Z_0, \tag{2.13}$$

which states that the differential impedance is twice the characteristic impedance, Z_0, of a transmission line.

2.3.3 Unidirectional Radiation

The classic sinuous antenna, as proposed by Du Hamel [26], makes use of an absorbing cavity to absorb back radiation, thus achieving unidirectional radiation. A cross-section of the feeding network and absorbing cavity structure is shown in Fig. 2.13. Antennas with an absorbing back-cavity exhibit unidirectional radiation patterns and very large bandwidths with close to constant input impedance. However, the absorbing cavity reduces radiation efficiency and increases the system temperature, which is not suitable for noise critical applications such as radio astronomy [36]. One alternative is to make use of a reflecting ground plane to achieve unidirectional radiation. The ground plane reflects back-radiation and offers a significant improvement of the system temperature [5].

Unfortunately, the reflecting ground plane implementation comes at the expense of bandwidth [5], but nonetheless, it still remains the preferred solution in terms of the reduced system temperature. An example of the implementation of a reflecting ground plane with an antenna in the ideal case is shown in Fig. 2.14.

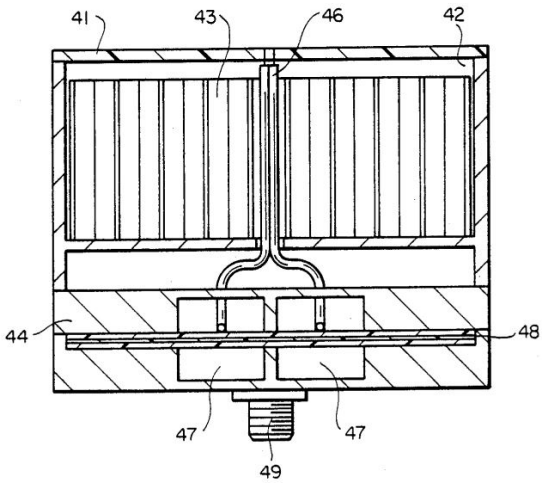

Figure 2.13: Absorbing cavity and feed network structure described in [26].

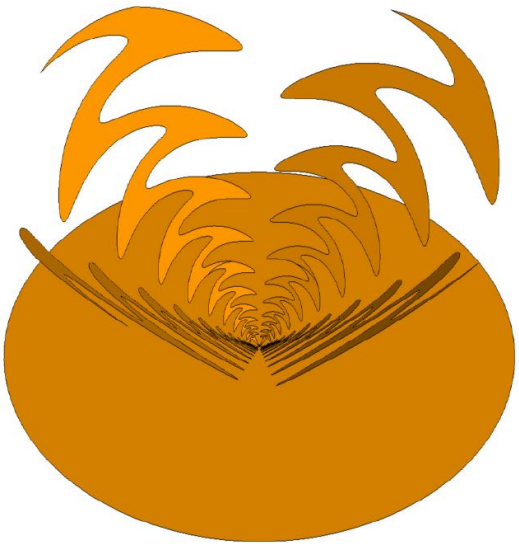

Figure 2.14: Reflecting ground plane for unidirectional radiation [9].

2.3.4 Feeding Procedure

There are some important aspects to consider when joining the sinuous antenna to a suitable feeding network. The integration of the feeding network and antenna is complicated by the geometry of the sinuous antenna at the feeding region, and the requirement that opposite arm pairs need to be differentially excited. These difficulties will be highlighted next with reference to Fig. 2.15. The antenna, with emphasis on its feeding region, is shown in Fig. 2.15a. The arms, or petals, of the sinuous antenna originate from distinct feed point locations which are numbered in a clockwise fashion.

The differential feeding requirement means that the first and third arms form a single arm pair, and the second and fourth arms form a separate arm pair. A schematic of the feeding network recommended by Du Hamel [26] is presented in Fig. 2.15b. The feeding scheme contains two baluns, one for each arm pair, connected to a 90° hybrid coupler. The purpose of the 90° hybrid component is to provide circular polarization if required. The schematic shows that an overlap occurs between feed point 3 and 4 when connecting the feeding points to the associated baluns. Careful planning and design from a feeding scheme perspective is required to make sure that an overlap does not occur.

A different, more convenient, approach can also be taken to bypass the overlapping arm pairs. This method involves untangling the antenna arm pairs by modifying the feeding region of the antenna. The feeding region, which is essentially contained within the radius of R_h in (2.9), and modifications made in close proximity to it should be considered carefully. Minor changes may have significant effects on antenna performance at high frequencies, especially differences in symmetry and transmission line length leading to the feed points.

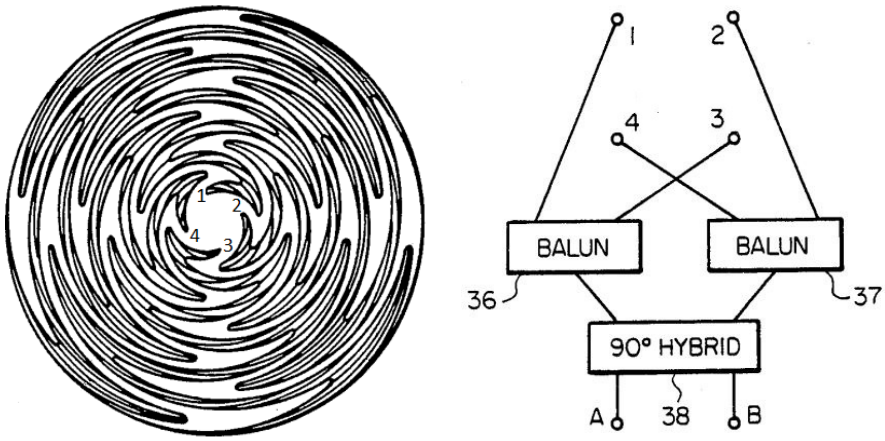

(a) (b)

Figure 2.15: The planar sinuous antenna by Du Hamel [26]. (a) Default feeding region. (b) Default feeding scheme.

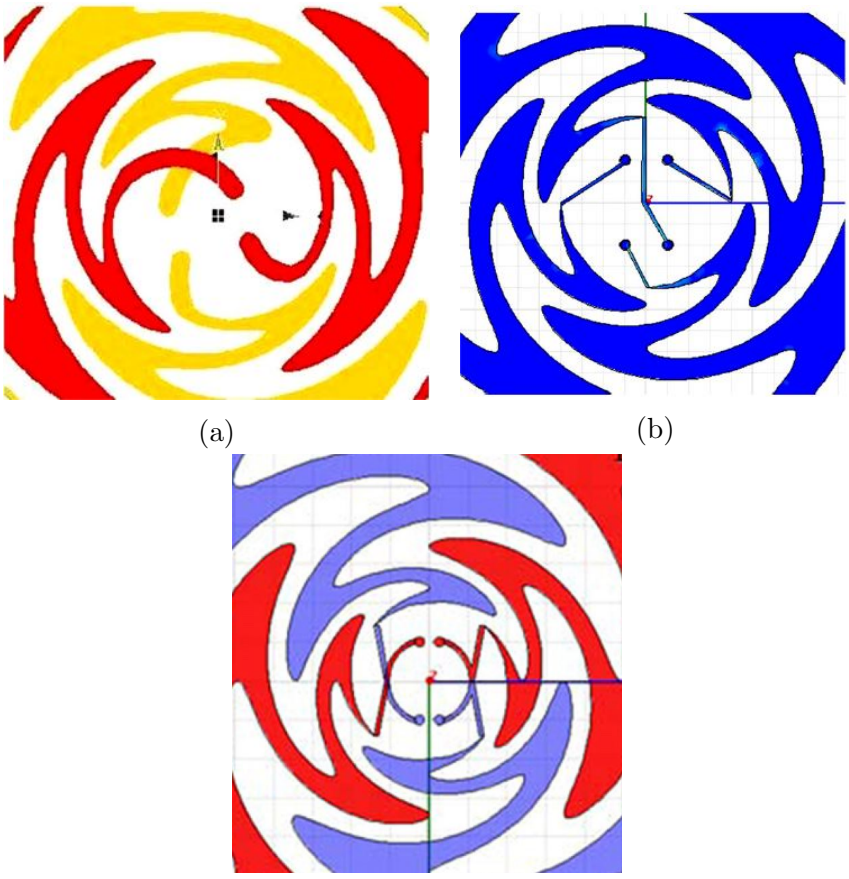

(a) (b)

(c)

Figure 2.16: Some existing feeding region modifications [15].

Examples of these modifications are shown in Fig. 2.16. These examples show different methods of untangling the antenna arms, so that opposite arms can be paired together. It is important to notice that the changes made to the feeding points in Fig 2.16a and Fig 2.16b distort the phase progression between at least one antenna-arm pair. The modifications also destroy the symmetry at the feeding region of the antenna. This asymmetry and difference in phase progression results in a non-symmetrical radiation pattern and high axial ratio (AR) when compared to Du Hamel's standard feed region [15].

The overlapping sinuous arms shown in Fig. 2.16a are achieved by printing them on opposite sides of a substrate. The top layer is indicated in red, and the bottom layer is indicated in yellow. The advantage of the sinuous antenna in Fig 2.16b is that it can be printed on one side of the substrate. The feeding region modifications in Fig. 2.16c resolve some of the issues regarding the asymmetry in Fig. 2.16a and 2.16b. The phase progression between opposite arms is maintained and consequently, the symmetry of the radiation pattern and the AR are better than the previous cases.

The feeding problem is further exacerbated by the high input impedance of the antenna. As mentioned in Section 3.2.1, the input impedance of each arm with respect to ground is 133 Ω, which means that differential input impedance of each arm pair is approximately 266 Ω. The impedance transformation of a single-ended impedance to a differential impedance of 266 Ω over a 10:1 bandwidth requires a balun with good impedance matching capabilities, such as the Marchand balun.

Chapter 3

Antenna Characterization

This chapter focuses on the aspects related to the design and simulation of the pyramidal sinuous antenna. A comprehensive understanding of the pyramidal sinuous antenna is required before the design of a suitable balun is attempted. A full-wave model of the sinuous antenna is also required in Chapter 6 for integration with the designed baluns.

The existence of the pyramidal sinuous antenna and how it came about is discussed in Section 3.1. Additional design parameters that are responsible for the geometry of the pyramidal antenna are considered in Section 3.2, followed by a section on the feeding points and feeding procedure of the antenna in Section 3.3. The pyramidal antenna is then generated using existing design parameters and the performance is characterized and verified in Section 3.4.

3.1 Pyramidal Sinuous Antenna

The pyramidal sinuous antenna can be traced back to the planar version of the antenna and consequently, many of the concepts and definitions relating to the planar antenna are still valid for the pyramidal antenna. However, the pyramidal version is really an alternate form of the conical sinuous antenna, created with the intention of easing the fabrication process. The fabrication of a conical sinuous antenna was presented in [33] and several difficulties experienced during construction were described. The prevailing issue related to the consistent projection of the sinuous arms onto the curved surface of the conical structure. The solution proposed by [8], was to project the sinuous arms on four separate planar surfaces, offset at an angle. The four surfaces are then joined together to form an inverted pyramidal structure. This allows for the antenna to be easily manufactured using standard, low cost PCB processes. The design parameters of the pyramidal version were taken from the optimized 2-6 GHz conical version in [33], so that the different versions could be compared. It was found that the theoretical aperture efficiency of the pyramidal antenna closely resembled the conical case, but the differential reflection coefficient did not, even though it was still better than -10 dB.

The reason was that the conical antenna had been optimized, while the pyramidal antenna had not. The pyramidal antenna outperformed the conical antenna where practical measurements were concerned. This was because the manufactured model matched the simulated model fairly accurately thanks to the simplified manufacturing process.

3.2 Structure Description

The pyramidal sinuous antenna is created by projecting the planar sinuous antenna onto an inverted pyramidal structure and then placing a reflecting plane behind the apex of the pyramidal structure. The reflecting plane is chosen to be circular and its radius is chosen to match the low frequency radius of (2.10). This is done in order to preserve the rotational symmetry of the antenna at the cost of high sidelobe levels at lower frequencies [33].

Image theory can be used to analyze the radiation performance of pyramidal antenna above a reflecting plane. A pair of $\lambda/2$ resonators, from opposite arms of the antenna, are selected as the radiating element sources. The images then appear the same distance below the reflecting plane. The resulting symmetry means that the phase centre is constant around the reflecting plane. Maximum broadside radiation is achieved when the resonators are placed a quarter wavelength above the reflecting plane. It is important that the offset angle, θ, is chosen to facilitate this for radiating elements at different frequencies. Essentially, the backward travelling wave travels a quarter wavelength, gets reflected, and then travels a quarter wavelength back to the source, after which it travels in phase with the forward travelling wave produced by the resonator. The side-view of the pyramidal antenna shown in Fig. 3.1a indicates the cone, or offset, angle θ and the height h of the antenna above the reflecting plane.

Note that the antenna depicted in Fig. 3.1 is not self-complementary. This is attributed to the fact that $\delta \neq \pi/2N$, and the presence of the reflecting ground plane. The self-complementary nature of the structure is lost resulting in impedance variation over frequency. From the top view angle in Fig. 3.1b, the antenna looks identical to the planar version of the sinuous antenna. Therefore, all the design parameters and definitions applicable to the planar version can be extended to the pyramidal version. The height of the antenna above the reflecting plane, and the pyramid's offset angle in the pyramidal version are the only other additional parameters. A summary of the design parameters of the pyramidal sinuous antenna is presented in Table 3.1

Table 3.1: Description of design parameters for the pyramidal sinuous antenna.

Design Parameter	**Description**
Angular width (α)	The sinuous curve swings between the polar angels $\pm\alpha$.
Rotation angle (δ)	Determines the thickness of sinuous arms.
Growth rate (τ)	Scaling ratio between adjacent cells.
Height (h)	Height of pyramidal structure above reflecting plane.
Offset angle (θ)	Tilt angle of the pyramidal structure.

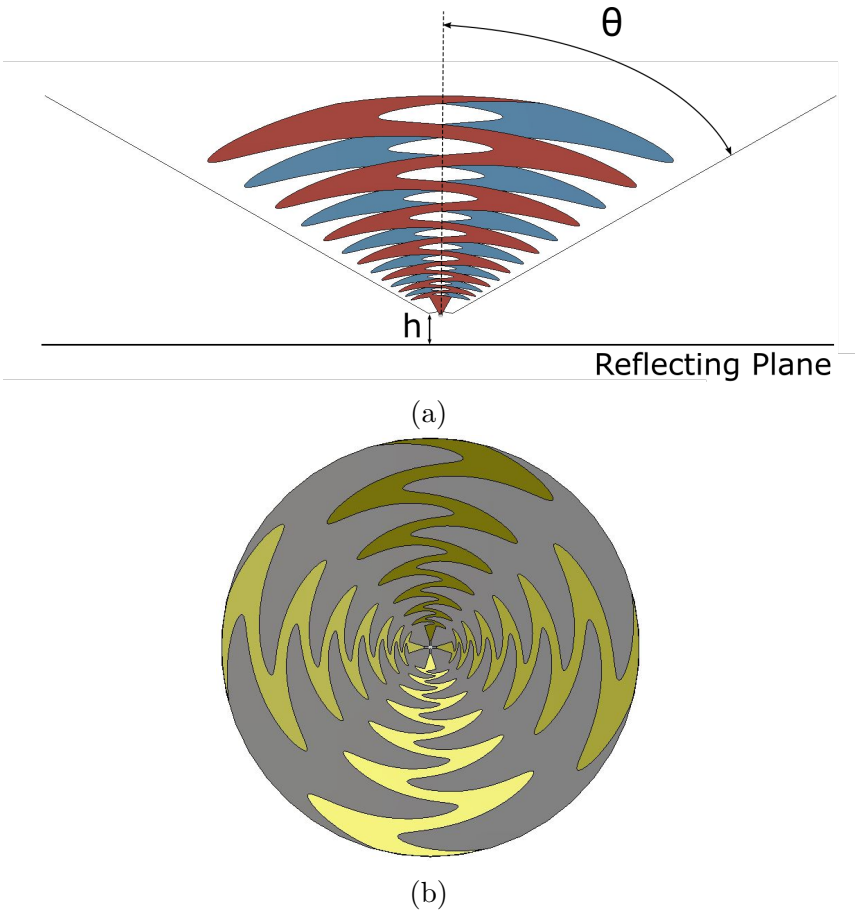

(a)

(b)

Figure 3.1: Geometric description of the pyramidal sinuous antenna. (a) Side view. (b) Top view.

3.3 Feeding Considerations

The feeding region modifications discussed in Chapter 2.3.4 are also valid for the pyramidal sinuous antenna. The only difference is that the feeding region will not be in the same plane as the antenna arms which are tilted. Following this, the feeding region of the pyramidal sinuous antenna may take a similar form as those shown in Fig. 2.16. However, the geometry of these feeding regions may change significantly when parameters of the antenna, mentioned in Table 3.1, are changed or optimized to achieve certain goals. To accommodate the various forms in which the antenna can occur, the eventual baluns that connect to opposite arm pairs should be designed in a general or open-ended fashion.

The input impedance of an antenna, which is not self-complementary, varies with frequency and cannot be determined by Deschamp's formula in (2.11). The input impedance is instead calculated using full-wave electromagnetic (EM) simulations.

3.4 Simulation of Pyramidal Sinuous Antenna

The ideal case of a dual-polarized pyramidal sinuous antenna is modelled in 3D full-wave EM software, so that the input impedance of the antenna can be determined. The theory described in previous sections is also verified. The process of generating the geometry is briefly described next for the purpose of reproducing the modelling process.

3.4.1 Generating the Geometry

The pyramidal structure was modelled using the design parameters presented in Table 3.2, which were taken from the optimized conical antenna presented in [33]. These parameters were also used in the modelling of the pyramidal structure in [9], and produced satisfactory, but not optimal, results. The improvement of the structure and results of the antenna are outside the scope of this thesis and therefore further design and optimization of the antenna is avoided. The process of generating the geometry of the antenna is discussed next.

Table 3.2: Design parameters of the pyramidal sinuous antenna.

Design Parameter	**Value**
Angular width (α)	24.85°
Rotation angle (δ)	14.95°
Growth rate (τ)	0.842
Height (h)	5 mm
Offset angle (θ)	56.48°
f_{min}	2 GHz
f_{max}	6 GHz

FEKO [37], a full-wave simulation software based on the Method of Moments (MoM), was the first choice considered for modelling the antenna. However, a similar antenna had already been created using this software [9], and during the course of that study a great deal of effort was spent finding ways of reducing the exceedingly long simulation times. This was because the desired accuracy of the MoM solver lead to inefficient simulation times. Instead, CST Microwave Studio [38] was considered thanks to its variety of available solvers.

The sinuous curve was first projected vertically onto a planar surface at an angle of 33.52° with reference to the horizontal plane. A single sinuous arm is then obtained which is then duplicated and rotated in 90° increments to form four sinuous arms. The isometric view of the modelled pyramidal sinuous antenna is shown in Fig. 3.2a. A close up of the feeding region is given in Fig. 3.2b. It shows how opposite arm pairs are ideally excited using differential 300 Ω ports. Note that the arm pairs do not cross; one arm pair crosses above the other.

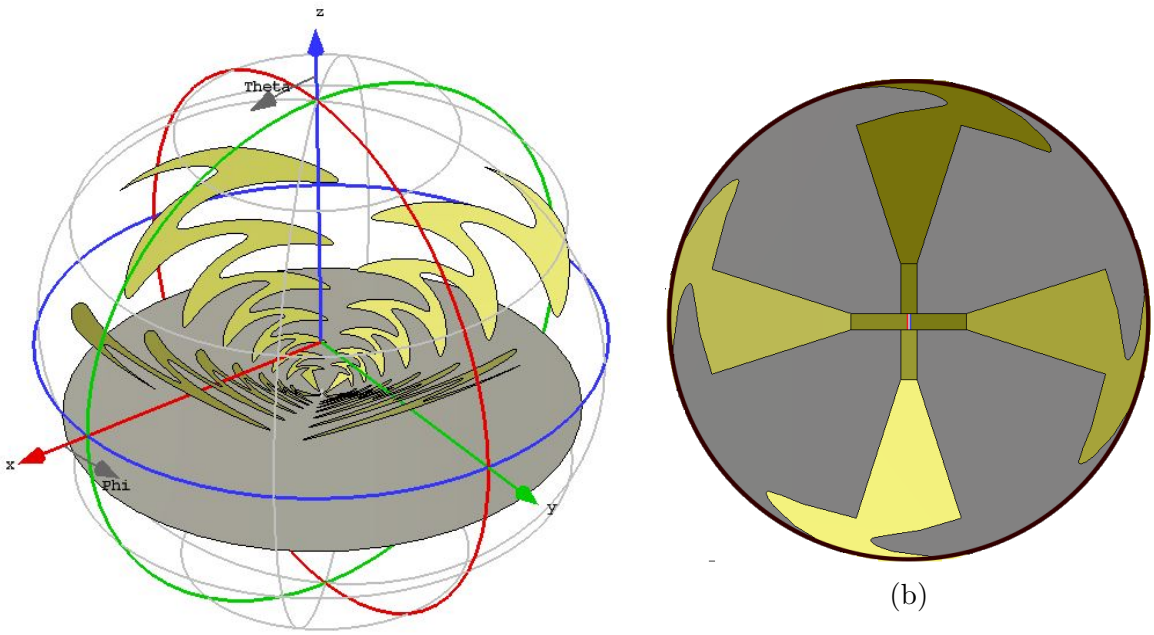

(a) (b)

Figure 3.2: Simulated pyramidal sinuous antenna (a) Isometric view of modelled antenna in CST Microwave Studio (b) Zoomed in feeding region and differential port definition.

3.4.2 Results

The transient and frequency domain solvers in CST MWS are described next with reference to [39, 40]. Both solvers are considered general purpose 3D EM analysis tools. The transient solver in particular can achieve arbitrarily fine frequency resolution during simulation without additional computational cost. Both solvers are capable of providing broadband electromagnetic nearfields and farfields as well as S-Parameters results, and adaptive mesh refinement options are available for both solvers. Because of this, both the transient and frequency domain solvers are frequently used in this work. The structures are analyzed using both solvers for validation and comparison purposes. The simulation times for both solvers are dependant on the desired simulation accuracy (transient solver) or number of samples (frequency domain solver) and can be set to provide coinciding results for similar simulation times. In this section, the transient solver is used to provide S-parameter and farfield results, and the frequency domain solver is used to validate these results.

The real and imaginary components of the input impedance of the antenna are shown in Fig. 3.3a. The input impedance varies with frequency, which is expected, and it has a mean input impedance of 301.4 Ω. The input impedance is subject to change, but for the purpose of this work, it will be specified as 300 Ω.

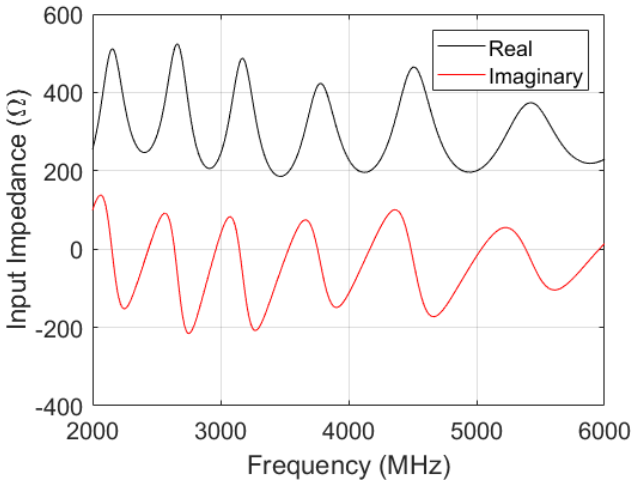

(a)

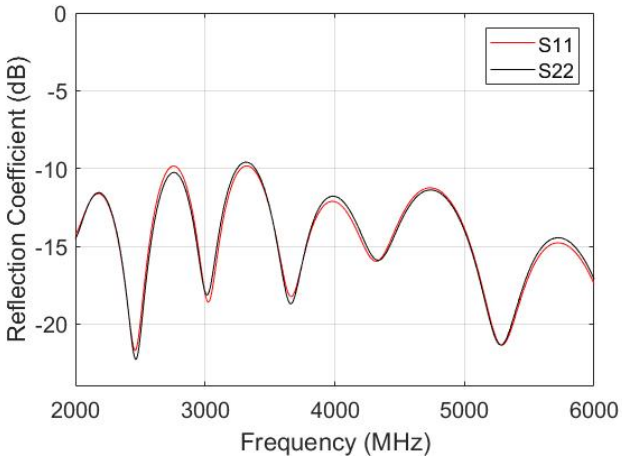

(b)

Figure 3.3: Selected frequency dependent results (a) Input impedance (b) Differential reflection coefficient.

The impedance of both differential ports exciting the antenna is therefore chosen as 300 Ω. Following this, the differential reflection coefficient of both ports is illustrated in Fig. 3.3b. The reflection coefficients are almost identical to each other, with a return loss better than 10 dB across the band from 2-6 GHz. The strong similarity between the reflection coefficients is due to the separate identical arm pairs.

The simulated antenna gain with respect to frequency is analyzed in Fig. 3.4, which shows the maximum gain at broadside ($\theta = 0°$) for an ideally excited dual-polarized antenna. The maximum gain is shown to be consistent, which is a prerequisite for a wideband antenna, and is generally better than 10 dB, except for a dip at 2.375 GHz.

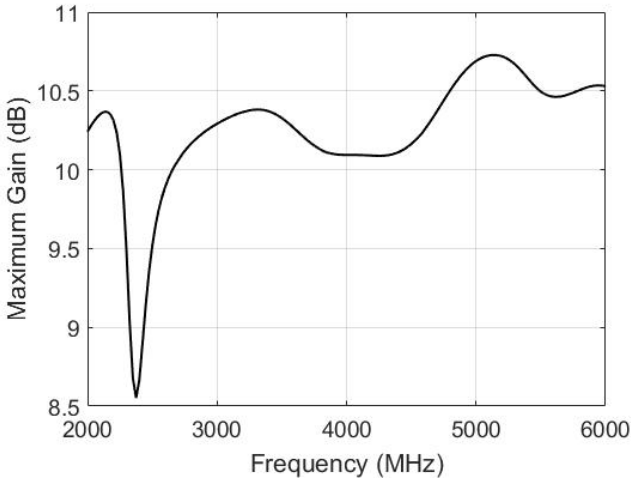

Figure 3.4: Maximum gain at broadside for ideal dual polarized pyramidal sinuous antenna.

The radiation patterns of the dual-polarized antenna are analysed in order to determine a reason for the reduced gain at 2.35 GHz. The normalized farfield, as a function of the elevation angle, θ, is given in Fig. 3.5. The farfield E-field is normalized to the maximum E-field. The fields for the principle azimuth cut of 180° are given in Fig. 3.5a. Additionally, the fields for the principle azimuth cut of $\phi = 90°$ are given in Fig. 3.5b for select frequencies of interest. The radiation fields are shown to be equal amplitude, unidirectional and symmetric for each azimuth cut. As expected, the sidelobe levels at the lower frequencies are quite high.

Analysis of the co-polar and cross-polar E-fields should provide some insight into the degraded performance. The co-polar and cross-polar fields, normalized to the maximum co-polar field, across the 2-6 GHz band for an azimuth cut of $\phi = 90°$ is shown in Fig. 3.5c. Symmetric radiation fields are obtained with cross-polarization better than -20 dB, except at 2.35 GHz which reaches a maximum of - 15 dB. High levels of cross-polarization, due to the specific design parameters of the antenna, affect the amplitude and phase of radiating waves at 2.35 GHz. The interference results in increased sidelobe energy which reduces the on-axis gain as seen in Fig. 3.5c.

Overall, the results shown in Fig. 3.3 and 3.5 agree well with the theory presented in previous sections and provide valuable insight into the design of a suitable feed.

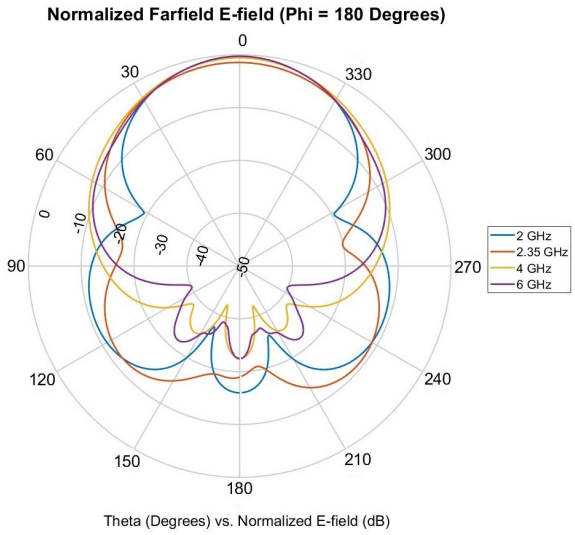

(a)

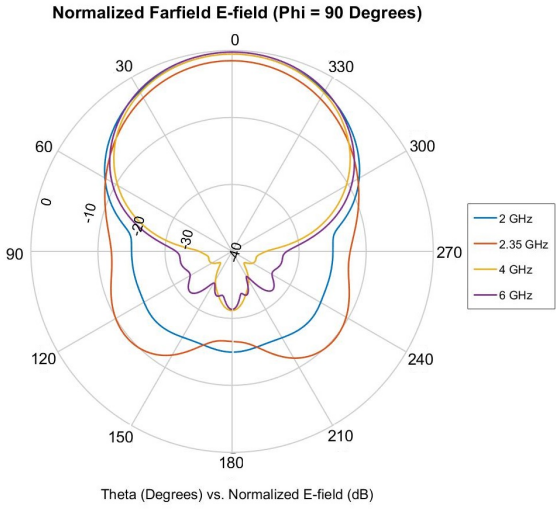

(b)

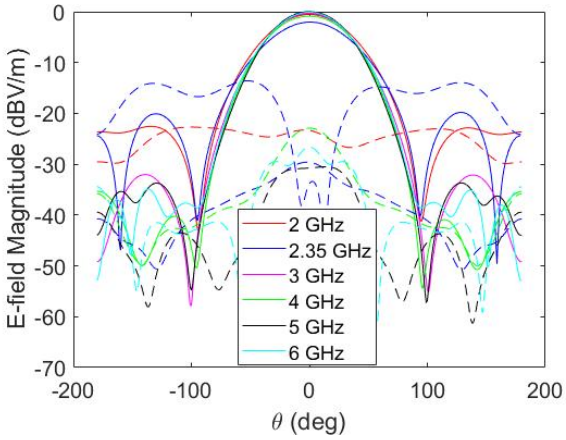

(c)

Figure 3.5: Radiation chatacteristics (a) Normalized farfield for $\phi = 180°$ (b) Normalized farfield for $\phi = 90°$ (c) Co-polar (solid lines) and cross-polar (dashed lines) E-fields at select frequencies.

3.5 Summary

The various concepts discussed in this chapter establish a starting point and approach for the design of a suitable balun. The arrangement of the feeding region and the impedance of the antenna, for instance, provide core restrictions/specifications to the balun design. The pyramidal antenna is yet to be optimized and therefore the design of the balun should be somewhat open ended. Future modifications/changes to the geometry of the antenna may then be accommodated with this flexible design.

The evaluated antenna coincided well with theoretical predictions, extending some of the results as noted in [9]. The antenna had a return loss better than 10 dB across the desired band for each polarization, and the resulting co-polar and cross-polar fields were symmetric with low cross-polarization. The maximum antenna gain was generally better than 10 dB over the band from 2-6 GHz, thanks to the frequency independent nature of the sinuous antenna. This characteristic is ideal for a wideband reflector feed. The input impedance of the antenna was determined through full-wave simulations and was found to be approximately 300 Ω.

Chapter 4

Planar Marchand Balun

The planar, or etched, derivative of the Marchand balun using coupled-lines was briefly discussed in Chapter 2.2.2. This type of printed balun is low-profile and would provide seamless integration with an antenna like the sinuous one. It also has the advantages of low-cost manufacturing and wideband performance. The problem, however, with the standard coupled-line Marchand balun is that bandwidth relies on the associated coupling factor of the quarter-wave lines, and cannot achieve the bandwidth needed for integration with the sinuous antenna. In this chapter, a modified version of the microstrip-coupled line Marchand balun is investigated to improve the coupling factor and consequently, the achievable bandwidth.

The contents of this chapter include the analysis, design, simulation and fabrication of a Marchand balun with ground plane apertures. Section 4.1 includes an introduction to the standard coupled-line Marchand balun, followed by a study of microstrip coupled-lines and ground plane apertures. These concepts are then applied to the Marchand balun. Section 4.2 details the electrical design process for a modified Marchand balun. Finally, Section 4.3 describes the manufacturing process for various implementations of the modified Marchand balun and measured results are compared to theoretical predictions.

4.1 Theoretical Background

4.1.1 Conventional Marchand Balun

A schematic representation of the conventional Marchand balun is shown in Fig. 4.1. It consists of two identical symmetric $\lambda/4$ coupled-lines that are joined together. The unbalanced input port connects directly to the first coupled-line section. The adjacent ports of the coupled-line sections are then joined together to form a $\lambda/2$ line section and a balanced port pair. The second coupled-line section is terminated by an open circuit as shown by "O.C" in the figure.

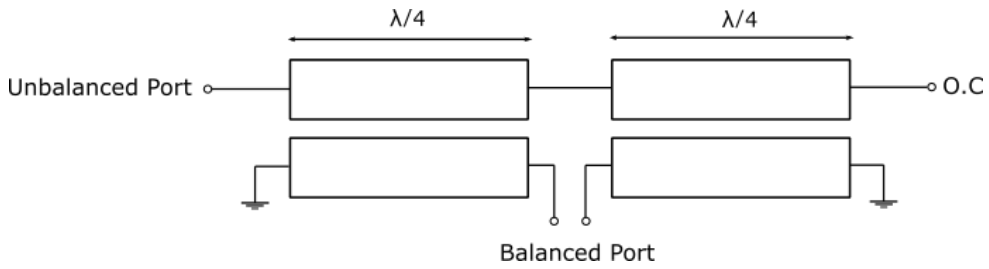

Figure 4.1: Planar coupled-line Marchand balun.

There are several ways to analyze and design the balun structure in Fig. 4.1. If a lumped network equivalent model of the balun is derived, then its impedance element values can be calculated to fit some filter response as described in [41]. This method is limited as it only explains the impedance frequency response of the balun with no indication of the balun's balance performance.

Another method involves analyzing the balun structure as a combination of two coupled-line sections. The scattering matrices of two identical symmetric couplers are used to derive the scattering matrix for the balun. The scattering matrix then explains the impedance frequency response, as well as the balance of the balun. The scattering matrix for the coupled-line balun with a source impedance, Z_0, and a differential load impedance, Z_1, was derived in [19] and is presented below,

$$[S] = \begin{bmatrix} \dfrac{1-k^2\left(\dfrac{2Z_1}{Z_0}+1\right)}{1+k^2\left(\dfrac{2Z_1}{Z_0}-1\right)} & j\dfrac{2k\sqrt{1-k^2}\sqrt{\dfrac{Z_1}{Z_0}}}{1+k^2\left(\dfrac{2Z_1}{Z_0}-1\right)} & -j\dfrac{2k\sqrt{1-k^2}\sqrt{\dfrac{Z_1}{Z_0}}}{1+k^2\left(\dfrac{2Z_1}{Z_0}-1\right)} \\ j\dfrac{2k\sqrt{1-k^2}\sqrt{\dfrac{Z_1}{Z_0}}}{1+k^2\left(\dfrac{2Z_1}{Z_0}-1\right)} & \dfrac{1-k^2}{1+k^2\left(\dfrac{2Z_1}{Z_0}-1\right)} & j\dfrac{2k^2\sqrt{\dfrac{Z_1}{Z_0}}}{1+k^2\left(\dfrac{2Z_1}{Z_0}-1\right)} \\ -j\dfrac{2k\sqrt{1-k^2}\sqrt{\dfrac{Z_1}{Z_0}}}{1+k^2\left(\dfrac{2Z_1}{Z_0}-1\right)} & j\dfrac{2k\left(\dfrac{Z_1}{Z_0}\right)}{1+k^2\left(\dfrac{2Z_1}{Z_0}-1\right)} & \dfrac{1-k^2}{1+k^2\left(\dfrac{2Z_1}{Z_0}-1\right)} \end{bmatrix}.$$

The relationship between the characteristic impedance and coupling coefficient, k, for a symmetric coupled-line is given by

$$Z_{0c} = \sqrt{Z_{0e}Z_{0o}}, \tag{4.1}$$

$$k = \frac{Z_{0e} - Z_{0o}}{Z_{0e} + Z_{0o}}. \tag{4.2}$$

The coupling coefficient of microstrip-coupled lines is specified by the even-mode impedance, Z_{0e}, and odd-mode impedance, Z_{0o}, which in turn are dependant on the dimensions of the coupled-line structure. The mode impedances are controlled by ϵ_r and height, h, of the substrate, as well as the trace width, W, and gap spacing, s, between the coupled sections. The relationship between Z_{0e}, Z_{0o} and the structure parameters is described in [20]. The ideal scattering matrix for a lossless balun can be obtained if k is specified as [19]

$$k = \frac{1}{\sqrt{\frac{2Z_1}{Z_0} + 1}}. \tag{4.3}$$

The scattering matrix then reduces to

$$[S] = \begin{bmatrix} 0 & \frac{j}{\sqrt{2}} & \frac{-j}{\sqrt{2}} \\ \frac{j}{\sqrt{2}} & \frac{1}{2} & \frac{1}{2} \\ \frac{-j}{\sqrt{2}} & \frac{1}{2} & \frac{1}{2} \end{bmatrix}.$$

The analysis shows that an impedance transforming Marchand balun can be designed with two symmetric coupled-lines and an appropriate coupling factor by making using of (4.1), (4.2) and (4.3).

Verification

A standard microstrip coupled-line Marchand balun, shown in Fig. 4.1, is designed according to the design procedure highlighted in Section 4.1.1. FR-4 substrate with a height h=1.6 mm and relative permittivity ϵ_r=4.55 is used during the design. The source impedance is chosen as Z_0=50 Ω and the differential load impedance is Z_1=300 Ω. The schematic of the coupled-line Marchand balun is shown in Fig. 4.2. The resulting coupling factor according to (4.3) is k=0.2774. The TXLine calculator in AWR Microwave Office (AWR MWO) [42] was utilized to determine W=4 mm and s=0.3 mm for the mode impedances that satisfy the required coupling factor.

The simulated performance of the balun is presented in Fig. 4.3. The reflection coefficient, S_{11}, and the insertion loss at each output port, S_{21}, and S_{31}, is depicted in Fig. 4.3a. The reflection coefficient is better than -10 dB across 2.6-3.2 GHz, which results in a proportional bandwidth of 1.23:1. The insertion loss response, S_{21}, coincides reasonably well with its S_{31} counterpart and is approximately -3.4 dB across the same band as S_{11}. The amplitude balance in Fig. 4.3b shows promising results as it is better than ±0.5 dB across the band. The same cannot be said for the phase balance shown in Fig. 4.3c which has a maximum phase variation of 10.4° at 3 GHz. The high phase imbalance occurs due to the unequal even and odd-mode phase velocities in the non-homogeneous microstrip medium [19].

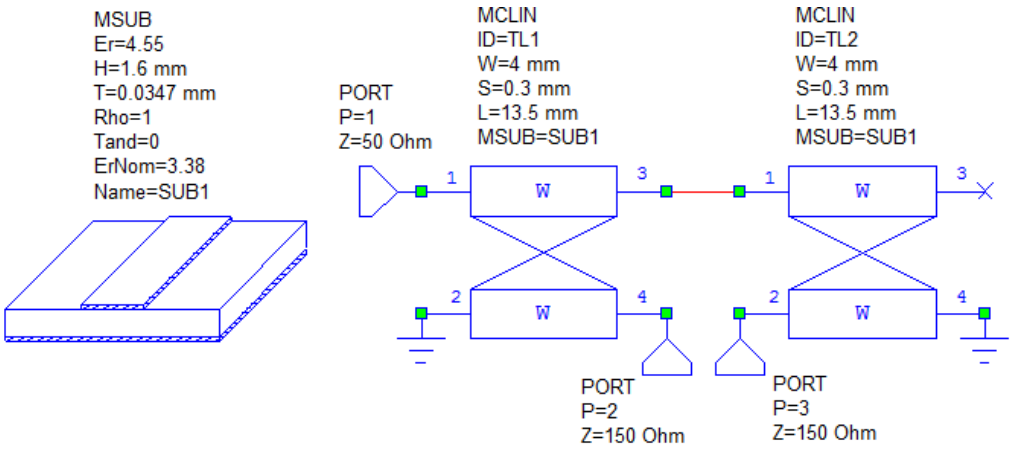

Figure 4.2: Planar coupled-line Marchand balun in MWO.

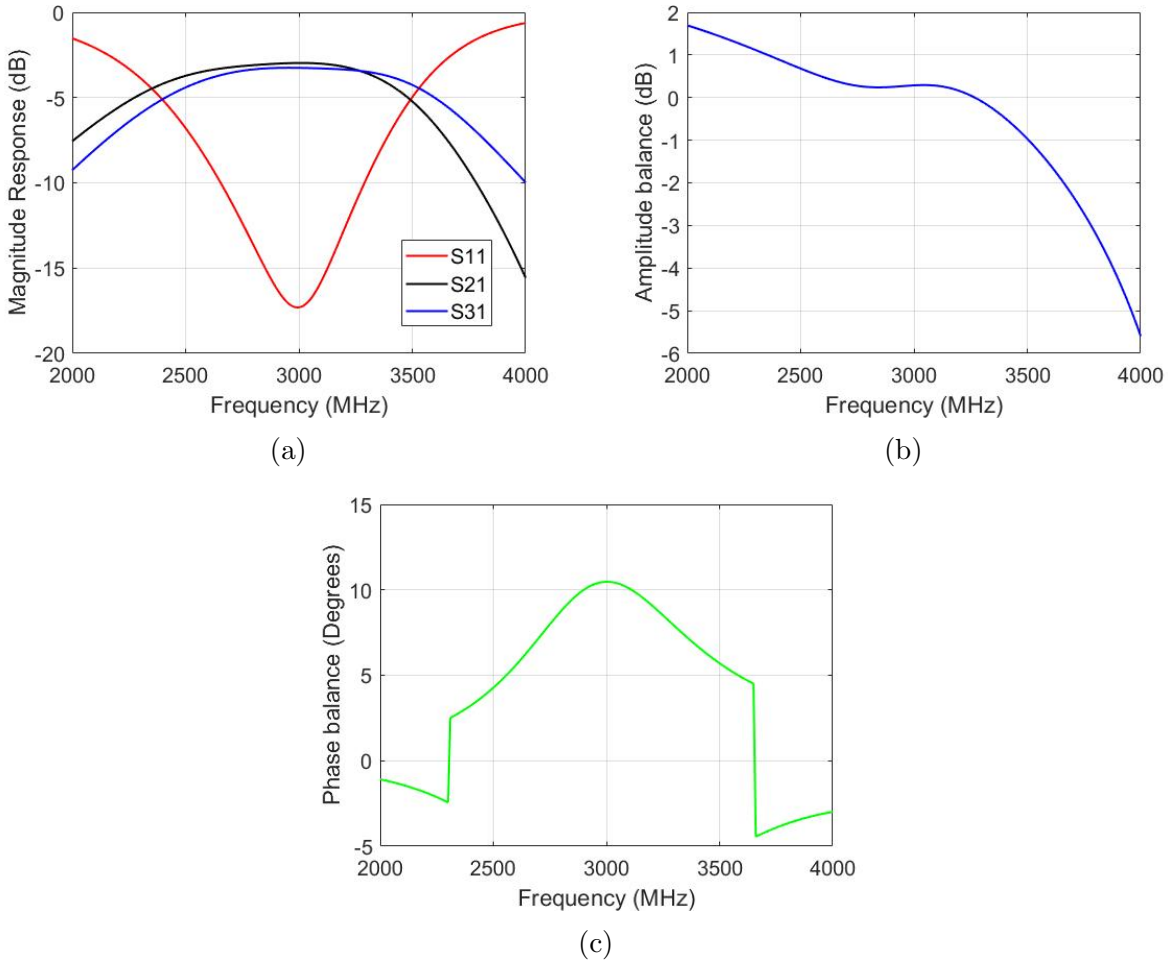

Figure 4.3: Simulated performance of coupled-line Marchand balun (a) Magnitude response of S-parameters (b) Simulated amplitude balance (c) Simulated phase balance.

The designed coupled-line Marchand balun performed as expected, confirming the theoretical analysis and design approach. However, the bandwidth is limited to approximately 1.23:1 which is not suitable for integration with the 3:1 bandwidth sinuous antenna.

4.1.2 Coupled-line Marchand Balun with Ground Plane Apertures

Marchand baluns that can be realized using microstrip coupled-lines and ground plane apertures (hereafter referred to as the modified Marchand balun) meet the necessary requirements for integration with the sinuous antenna. The configuration is identical to the standard implementation shown in Fig. 4.1, with the exception of the ground plane apertures. The baluns have wideband capabilities and the planar layout aids in maintaining a low profile. The balun can be fabricated using standard PCB printing techniques, making it quick and easy to produce.

Sufficient performance of the coupled-line Marchand balun, or modified Marchand balun, can be achieved for even-mode impedance, Z_{0e}, between 3 and 5 times that of the odd-mode impedance, Z_{0o} [20]. The design methodology described by Zhang [23] is based on this idea and the balun design equation is derived through even and odd-mode analysis of two symmetric coupled-line structures. The S-parameters that characterize the operation of a balun, $|S_{11}| = 0$ and $S_{21} = -S_{31}$, results in the following design equation [23],

$$\left[(Y_{0_e} - Y_{0_o})\csc(\theta)\right]^4 - 2Y_aY_b(Y_{0_e} - Y_{0_o})\csc^2(\theta) = 0, \tag{4.4}$$

where Y_{0e} and Y_{0o} denote the respective even- and odd-mode admittances, and Y_a and Y_b denote the respective source and load admittances. If the length of the coupled-line sections are made $\lambda/4$, then $\theta = 90°$. Therefore, (4.4) reduces to

$$(Y_{0_e} - Y_{0_o})^4 - 2Y_aY_b(Y_{0_e} - Y_{0_o})^2 = 0, \tag{4.5}$$

$$(Y_{0_e} - Y_{0_o})^2 = 2Y_aY_b, \tag{4.6}$$

which can be rewritten as

$$\frac{1}{Z_{0_e}} - \frac{1}{Z_{0_o}} = \sqrt{\frac{2}{Z_aZ_b}}. \tag{4.7}$$

Equation (4.7) describes the relationship between the even-and odd-mode impedances for arbitrary source and load terminations. This is graphically illustrated in Fig. 4.4.

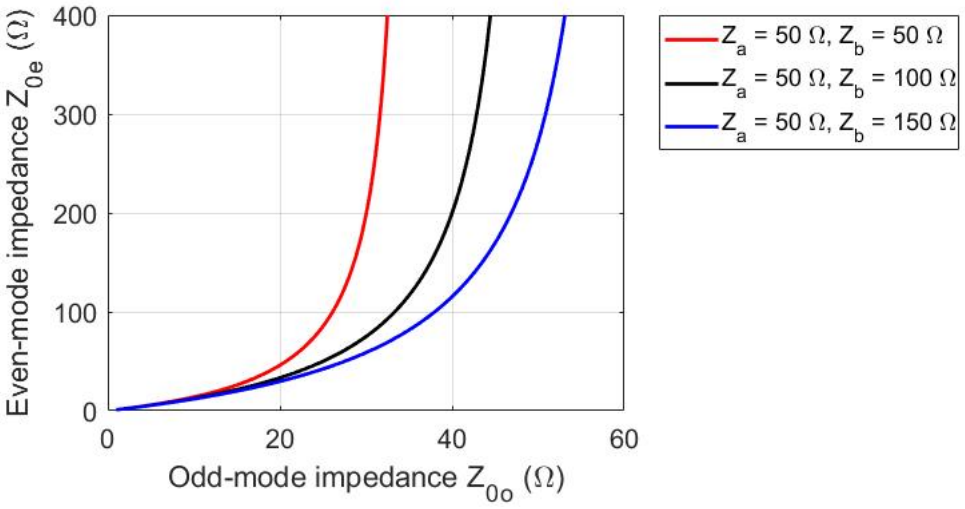

Figure 4.4: Relationship between even- and odd-mode impedances for different source and load terminations.

Three different cases are shown in Fig. 4.4. The first case is Z_a=Z_b=50 Ω, the second case is Z_a=50 Ω and Z_b=100 Ω and the third case is Z_a=50 Ω and Z_b=150 Ω . The third case is highlighted because it represents the 50 Ω coaxial input and the 150 Ω single-ended input impedance of the sinuous antenna. Indeed, there are many combinations of even- and odd-mode impedances that will satisfy (4.7). However, tight coupling, and subsequently large even-mode impedance, is required to achieve wideband performance. This is shown in Fig. 4.5 and 4.6 with two different implementations of the standard Marchand balun. Both implementations have 50 Ω source and load terminations as shown in Fig. 4.5a and 4.6a.

A low even-mode impedance of 50 Ω was chosen for the first implementation. The odd-mode impedance of 20 Ω coincides with the design curve in Fig. 4.4. The reflection coefficient and insertion loss at both output ports are plotted in Fig. 4.5b. The reflection coefficient is better than -10 dB from 3.2-5.1 GHz, so the bandwidth is 1.6:1. The insertion loss at both output ports is -3.01 dB, indicating equal power at the output ports across the same frequency band.

A larger even-mode impedance of 100 Ω was chosen for the second implementation. The odd-mode impedance of 25 Ω was chosen in the same manner as before. The reflection coefficient and insertion loss at both output ports are plotted in Fig. 4.6b. The reflection coefficient is better than -10 dB from 2.4-5.5 GHz, so the bandwidth exceeds an octave. The insertion loss at both output ports is again -3.01 dB across the same frequency band. The significant increase in bandwidth for the second implementation confirms that tight coupling between the coupled-line sections of the Marchand balun leads to improved bandwidth.

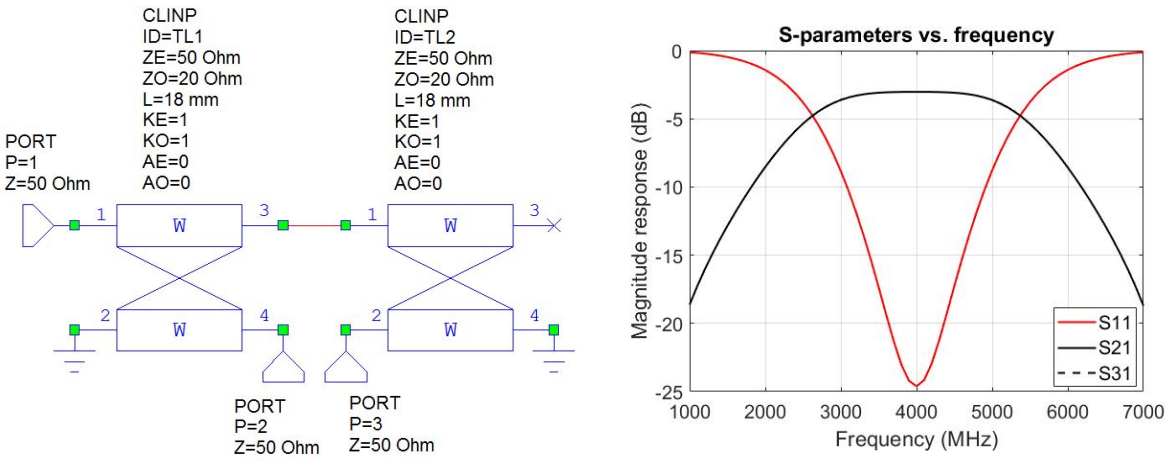

(a) (b)

Figure 4.5: Bandwidth enhancement of the standard Marchand balun (a) Schematic of first implementation (b) Reflection coefficient and insertion loss of first implementation.

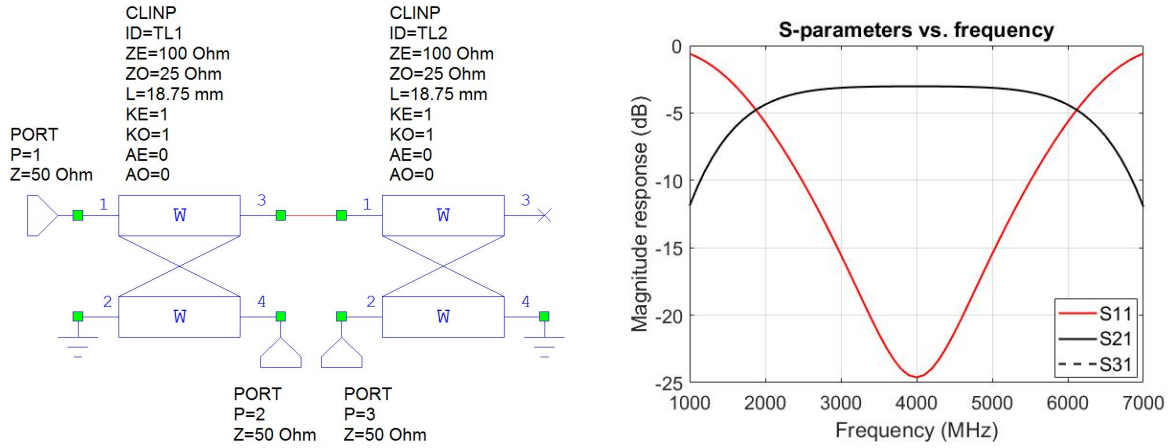

(a) (b)

Figure 4.6: Bandwidth enhancement of the standard Marchand balun (a) Schematic of second implementation (b) Reflection coefficient and insertion loss of second implementation.

Analysis of Ground Plane Slots

Coupled microstrip transmission lines with ground plane apertures are the main elements affecting the performance of the modified Marchand balun. It is important to be able to predict the influence that these apertures have on the performance of the coupled sections. Therefore, a short study relating to these concepts is conducted to conclude this section. Theory regarding even- and odd-mode analysis of symmetrical coupled-lines and general characteristics of transverse electromagnetic (TEM) modes can be found in [20].

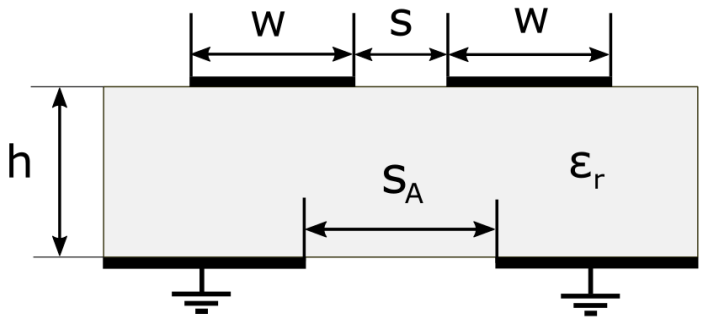

Figure 4.7: Cross section of coupled microstrip line with ground plane aperture.

Ground plane apertures refer to slots, or openings, that appear in the ground layer of a double-sided PCB. This structure is a basic building block of the modified Marchand balun and a thorough understanding of it is therefore required. A cross-section of a coupled microstrip line with a ground plane aperture is shown in Fig. 4.7.

The parameter, h, denotes the height of the substrate. w, denotes the trace width. s, denotes the gap spacing between the lines. s_A, denotes the width of the slot and ϵ_r denotes the relative permittivity of the substrate. This structure provides tight coupling in comparison to conventional microstrip lines, which relaxes the requirements on the physical dimensions (trace width and gap spacing) of the coupled-line structure [20]. These structures have also seen frequent use in the design of filters and couplers with enhanced performance [43, 44].

The even- and odd-mode parallel-plate and fringing fields for a standard microstrip coupled-line are shown in Fig. 4.8. Introduction of a slot beneath the coupled-lines significantly decreases the parallel-plate fields in the region beneath the transmission lines, and thus the capacitance in this region is also decreased. Intuitively, it also follows that the fringing fields in both the even- and odd-modes are less affected by the presence of the slot. The even- and odd-mode effective dielectric constants, indicated by ϵ_{ree} and ϵ_{reo} respectively, are then reduced according to

$$\epsilon_{ree} = \frac{C_e}{C_{0e}}, \tag{4.8}$$

$$\epsilon_{reo} = \frac{C_o}{C_{0o}}, \tag{4.9}$$

where C_e and C_o denote the respective even- and odd-mode capacitances in the presence of the inhomogeneous dielectric medium. C_{0e} and C_{0o} denote the respective even- and odd-mode capacitance of either line obtained by replacing the relative permittivity of the surrounding dielectric material by unity.

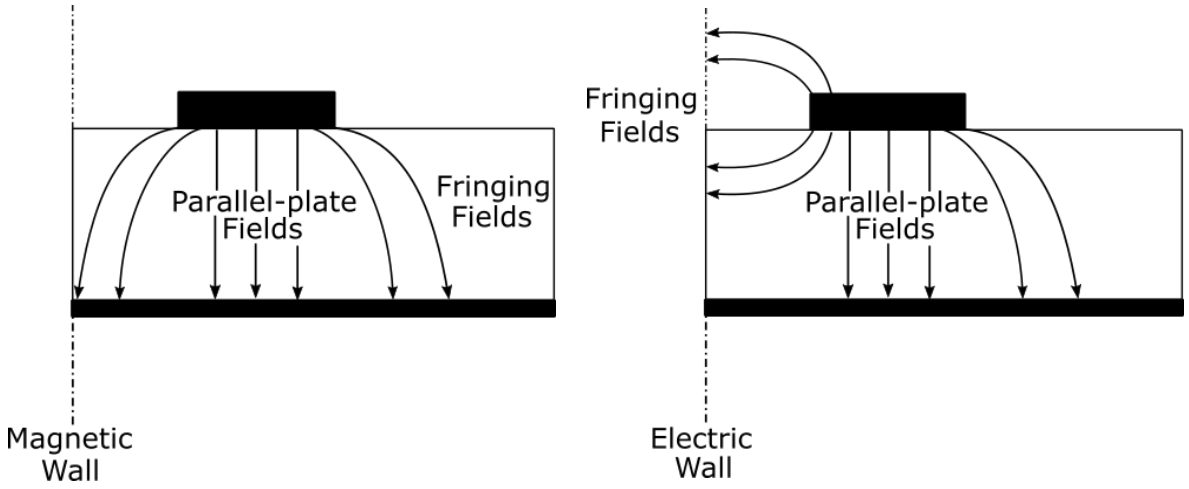

(a) Even mode (b) Odd mode

Figure 4.8: Even- and odd-mode electric fields of symmetric coupled lines.

The change in ϵ_{ree} and ϵ_{reo} has an influence on the even- and odd-mode phase velocities according to

$$v_{pe} = \frac{c}{\sqrt{\epsilon_{ree}}}, \tag{4.10}$$

$$v_{po} = \frac{c}{\sqrt{\epsilon_{reo}}}, \tag{4.11}$$

where, c, is the speed of light. The change in even- and odd-mode phase velocity results in a change in the respective even- and odd mode wavelengths, as wavelength is directly proportional to phase velocity. Therefore, the wavelength increases as the width of the slot increases. The structure becomes electrically smaller and shifts the frequency dependant results up in frequency. This is inconvenient, but a simple solution would be to design for a frequency slightly lower than the required frequency, or to slightly tune the length of the coupled-line sections. The even- and odd-mode impedances of the structure can then be calculated according to

$$Z_{0e} = \frac{1}{v_{pe}C_e}, \tag{4.12}$$

$$Z_{0o} = \frac{1}{v_{po}C_o}. \tag{4.13}$$

Taking (4.10) and (4.11), and combining them with (4.12) and (4.13) respectively, the even- and odd-mode impedances can be rewritten as follows,

$$Z_{0e} = \frac{1}{c\sqrt{C_e C_{0e}}}, \tag{4.14}$$

$$Z_{0o} = \frac{1}{c\sqrt{C_o C_{0o}}}. \tag{4.15}$$

Therefore, the addition of a slot directly beneath the coupled-lines has the result of decreasing the even- and odd-mode capacitance and consequently increasing the even and odd-mode impedance according to (4.14) and (4.15). The even-mode phase velocity is expected to increase at a faster rate than the odd-mode phase velocity for increases in slot size. This is because the even-mode capacitance is largely dependant on the parallel-plate fields directly below the trace and therefore fringing fields do not have a significant effect on the overall even-mode capacitance. However, both the fringing fields and the parallel-plate fields contribute significantly to the overall odd-mode capacitance, and thus the odd-mode phase velocity is expected to be less affected by changes in slot width.

Verification

The structure shown in Fig. 4.7 is modelled in CST MWS to confirm the theoretical analysis. Rogers RO4003C substrate with a thickness of 0.635 mm and $\epsilon_r = 3.38$ was used. The trace width of the coupled-lines was chosen to be w=0.5 mm and the gap spacing was chosen to be s=0.15 mm. The resulting structure is shown Fig. 4.9.

The size of the slot, s_A, is varied from 1-5 mm and the effect it has on some transmission line characteristics is depicted in Fig. 4.10. Fig. 4.10a and 4.10b represent the changes in even- and odd-mode impedance for increasing slot widths, while Fig. 4.10c depicts the change in the even- and odd-mode effective dielectric constants and 4.10d describes the phase velocity for increasing slot widths.

The results presented in Fig. 4.10 generally follow the expected trend: increasing slot widths lead to reduced C_e and C_o, resulting in increases in the even- and odd-mode impedance. The even-mode impedance increases greatly, while the odd-mode impedance increases only slightly. A discrepancy with the trend occurs in the odd-mode case. Fig. 4.10c shows that ϵ_{reo} actually increases between 1 mm and 2 mm, before following a decreasing tendency again. This increase follows from an increase in C_o, and thus the odd-mode impedance is expected to decrease slightly. This is shown to be false according Fig. 4.10b, where Z_{0o} still increases between 1 mm and 2 mm. The reason for the contradictory results is due to unpredictable odd-mode fields as the slot width approaches the region around $s_A = 2w + s$, and the unexpected significant influence of C_{0o}. A decrease in the odd-mode effective dielectric constant results in a decrease of C_o, but an increase of C_{0o}. Similarly, an increase in the odd-mode effective dielectric constant leads to an increase in C_o, but a decrease in C_{0o}. A positive trend in the odd-mode impedance therefore implies that C_{0o} is reduced while C_o is enlarged, and that the reduction in C_{0o} is greater than the increase in C_o causing Z_{0o} to increase.

Figure 4.9: Cross section of coupled microstrip line with ground plane aperture as seen in CST.

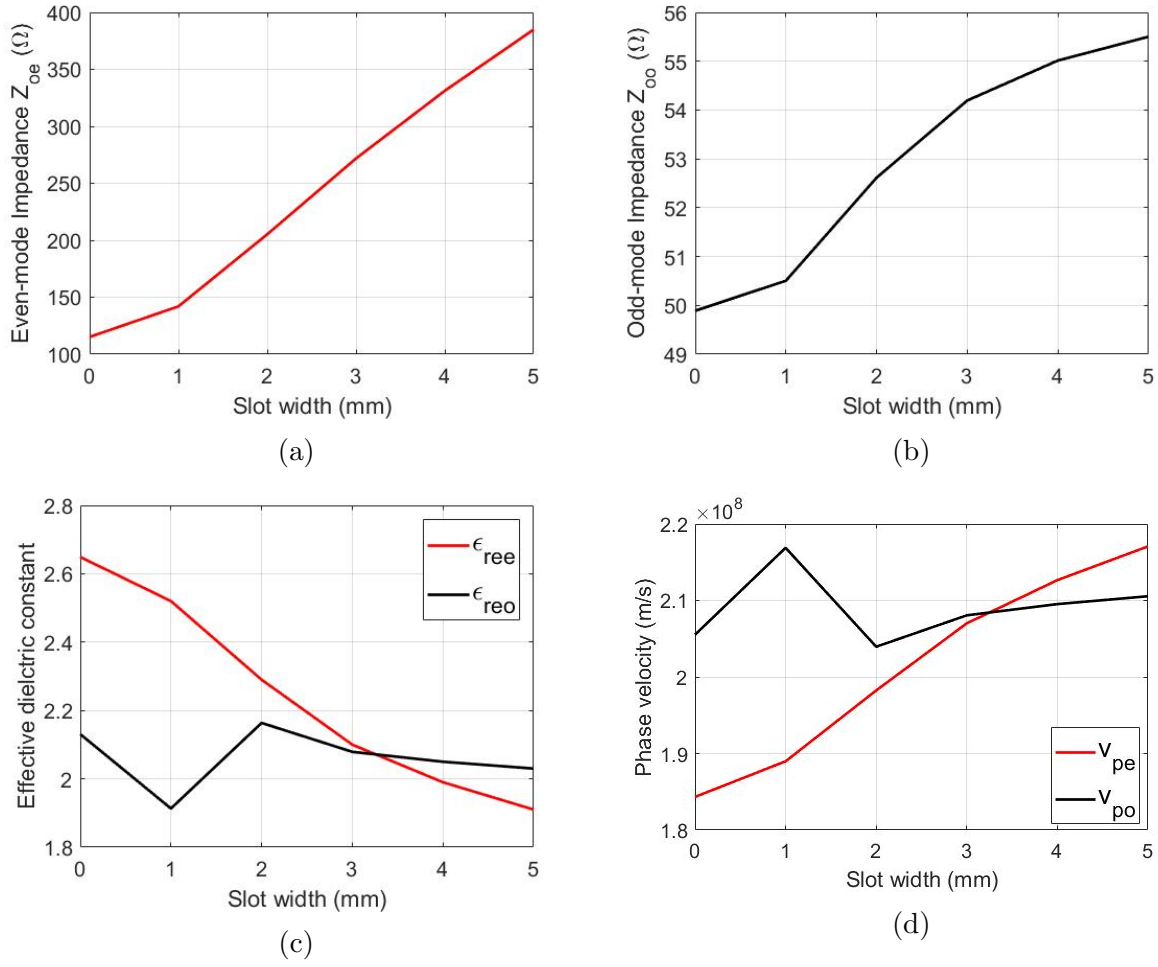

Figure 4.10: Microstrip coupled-line simulation results (a) Even-mode impedance (b) Odd-mode impedance (c) Even and odd-mode effective dielectric constant (d) Even and odd-mode phase velocity.

The verification process coincided well with the theoretical analysis and provided valuable insight relating to the presence of a slot beneath microstrip coupled-lines. The ability to increase the even-mode impedance is extremely valuable to the design of a wideband Marchand balun.

4.2 Electrical Design

4.2.1 Ideal Modified Marchand Balun

The coupled-line Marchand balun, shown in Fig. 4.11a, is designed in AWR MWO as a first step in the design process. The even- and odd-mode impedances are chosen according to the Z_a=50 Ω and Z_b=150 Ω design curve in Fig. 4.4. For wideband performance Z_{0e}=247 Ω, which results in Z_{0o}=50.2 Ω. The length of the quarter-wave coupled sections is l =18.75 mm to provide a centre frequency at 4 GHz.

The reflection coefficient and insertion loss are shown in Fig. 4.11b. The reflection coefficient is better than -10 dB across 1.54-6.45 GHz. The insertion loss at both output ports varies between approximately 3.011 dB and 3.337 dB across the same band. The resulting bandwidth is 4.25:1. It must be noted that the amplitude and phase balance are zero in the ideal case. The results presented here are the in the ideal scenario, but indicate that the microstrip coupled-line Marchand balun with tight coupling is suitable, and requires further investigation.

It is almost impossible to achieve the high even-mode impedance required for the Marchand balun in Fig. 4.11 using standard means. For instance, in a standard microstrip coupled-line configuration, with h=0.5 mm and ϵ_r=2.5, a gap spacing of 0.1 mm and a trace width of 55 μm is required to achieve an even-mode impedance of 250 Ω. The standard design, which requires high even-mode impedance, is clearly constrained by practical limitations. The study in Section 4.1.2 showed that ground plane slots beneath microstrip coupled-lines increases the even-mode impedance considerably, relaxing the requirements on the trace width and gap spacing. The high even-mode impedance required by the Marchand balun can therefore be achieved by utilizing slots in the ground plane.

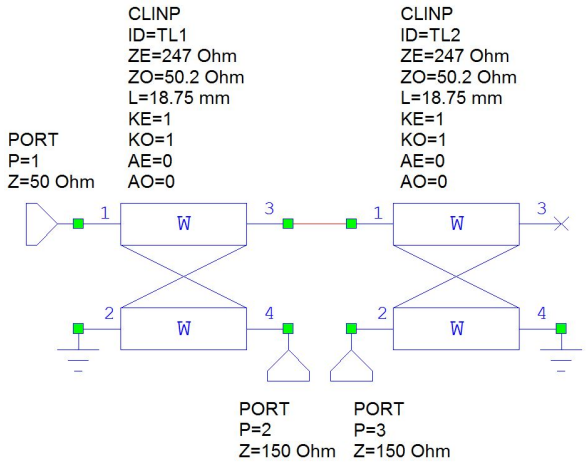

(a)

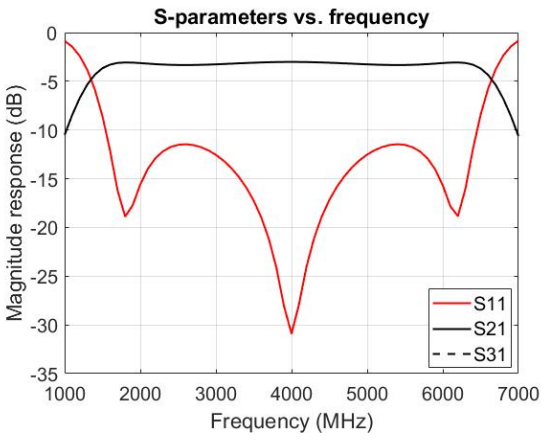

(b)

Figure 4.11: Initial design of modified Marchand balun. (a) Ideal schematic. (b) Magnitude response of S-parameters.

4.2.2 Feeding Considerations

Fig. 4.12 shows two different implementations of the modified Marchand balun. The first implementation presented in [23] is shown in Fig. 4.12a, and the proposed balun for integration with the antenna is shown in Fig. 4.12b. The slots are placed directly underneath the coupled-line sections and are indicated by dashed lines. The geometric aspects of these implementations, as well the advantages and disadvantages of each implementation is studied next.

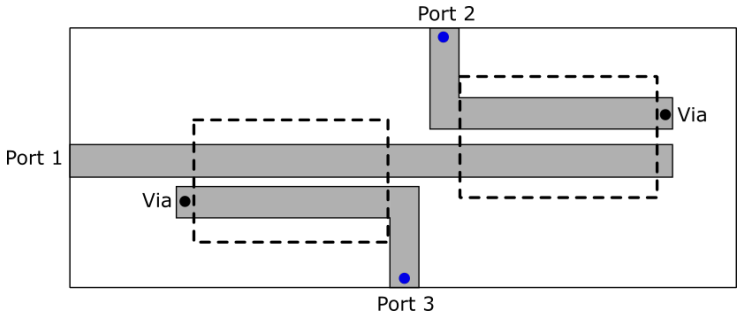

(a)

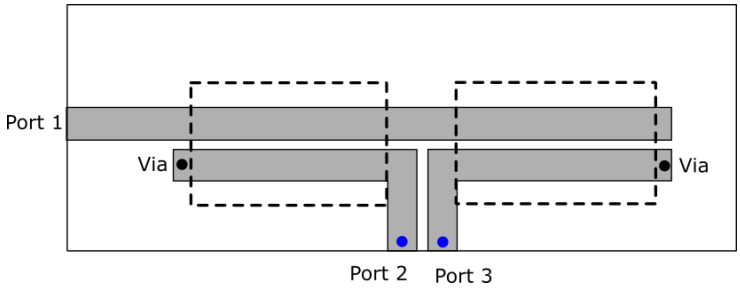

(b)

Figure 4.12: Modified Marchand balun implementations (a) Proposed layout from the study in [23]. (b) Proposed layout in this work.

The modified Marchand balun from Fig. 4.12a is studied first. The input port is labelled Port 1, and the output ports are labelled Port 2 and Port 3. The points where the balun connects to the antenna or "feed points" are marked in blue. The location of the output lines on opposite sides of the substrate complicates integration of the balun with other balanced microwave components, like the sinuous antenna. Also, the misalignment of the output ports results in a misalignment of the associated feed points, but this is only a slight inconvenience as the balun can be rotated until the feed points are aligned vertically. This balun configuration prevents coupling between the output ports and provides a consistent layout for practical measurements. It is also versatile for different sizes of the feeding region and is therefore suitable for feeding a two-arm sinuous antenna. The problem is that a four-arm sinuous antenna would require two baluns of this type to overlap in an awkward manner in order to feed the antenna. This problem was addressed in [14] for a different implementation of the Marchand balun, but an alternative solution was not provided.

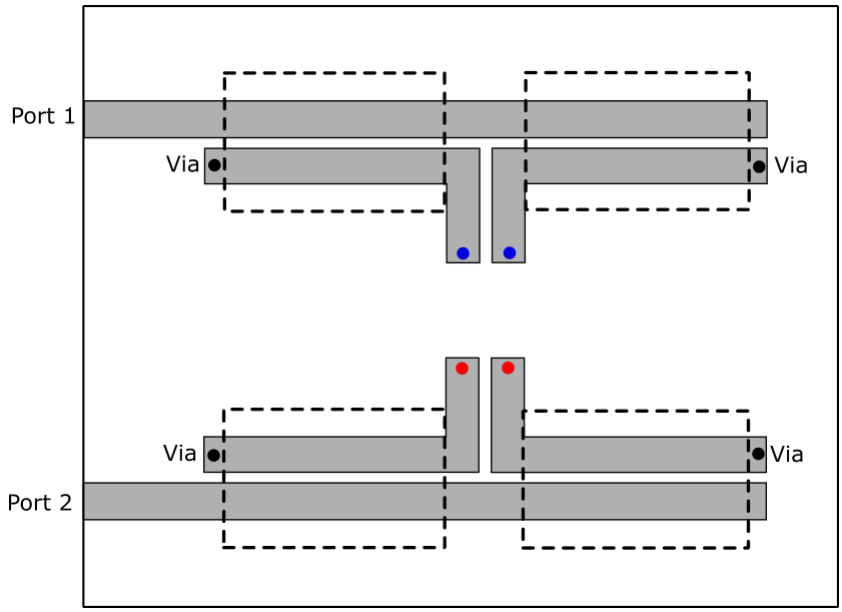

Figure 4.13: Modified Marchand balun feeding scheme for feeding a dual-polarized pyramidal sinuous antenna.

The configuration in Fig. 4.12a is modified so that the output lines now appear on the same side of the substrate. However, the result is that the balanced output lines join together, and the balun loses proper functionality. Separation of the output lines can be re-established by slightly reducing the length of the coupled-line sections, as shown in Fig. 4.12b. Balun functionality is then restored, but this introduces unwanted coupling between the output lines. The Marchand balun is characterized by $\lambda/4$ coupled-line sections and so significant reduction of coupled-line section lengths will reduce coupling between the output lines, but negatively affect balun performance, especially at high frequencies. Therefore, a trade-off exists between separation of the output lines and length of the coupled-line sections. Nevertheless, the proposed changes provide a convenient solution for feeding a two-arm sinuous antenna or the four-arm sinuous without overlap as shown in Fig. 4.13.

Fig. 4.13 depicts two modified Marchand baluns on a single substrate along with the four feed points of the antenna situated on a horizontal plane above the baluns. The feed points marked in blue are responsible for one pair of sinuous arms, and the feed points marked in red are responsible for the other pair. Parallel circular conductors form the connection between the balun outputs and the feed points of the antenna. These proposed layout changes provide a coherent and simple means of integration for the baluns and antenna while also being easy to manufacture using standard PCB techniques.

4.2.3 Design Process

The design procedure of the modified Marchand balun is described next with reference to Fig. 4.14 and the flow diagram shown in Fig. 4.15. The configuration shown in Fig. 4.12b serves as a starting point for the full-wave simulation design. The Rogers RO4003C substrate with a thickness of 0.762 mm was selected for its low-loss characteristics $\tan(\delta) = 0.0012$ and low relative permittivity $\epsilon_r = 3.38$. A low value of ϵ_r enables wider microstrip traces for high impedances. The thickness of the substrate can also be increased to achieve the same result if necessary.

The parameters of the coupled-line sections, w_1 and s_1, are set first. It is better to choose parameters that ensure a high coupling factor and therefore small values of w_1 and s_1 are preferred. The balanced output line trace width, w_2, was chosen inline with etching equipment capabilities and a minimum trace width of 0.5 mm was suggested. This produces an impedance of 97 Ω given the substrate definitions. Of course, this limits the impedance transformation of the balun to roughly 2:1. However, the impedance of the output lines can be increased by making use of the existing underlying slot and following the same principles described in Section 4.1.2.

The next step is to determine the ideal slot width for the balun. The procedure involves initially guessing w_3 and then estimating the resulting Z_{0e} and Z_{0o} of the coupled-line sections. The design curves then give an idea of what the impedance transformation of the balun is. This process is repeated until the desired impedance transformation is achieved. The width of the slot also needs to be set carefully to account for the balanced output lines. A wide slot may require long output lines placed directly above it, and a narrow slot may be unable to provide the required Z_{0e} and Z_{0o}. The length, l_1, of the slot is slightly shorter than a quarter wavelength to accommodate the via to ground.

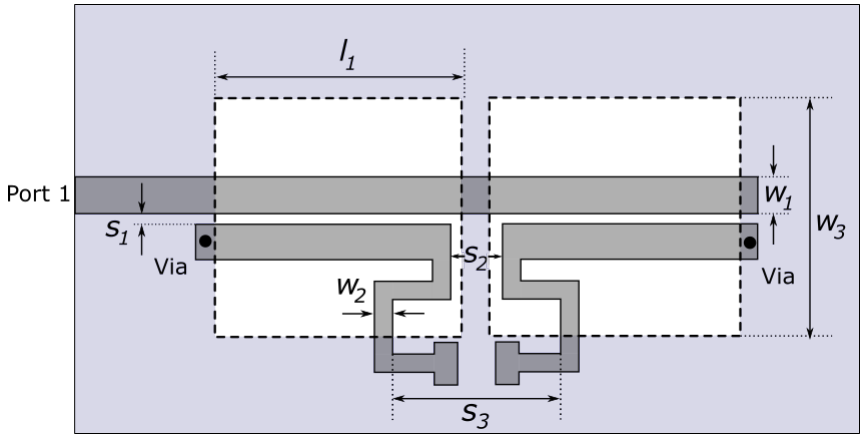

Figure 4.14: Design schematic of the modified Marchand balun prototype.

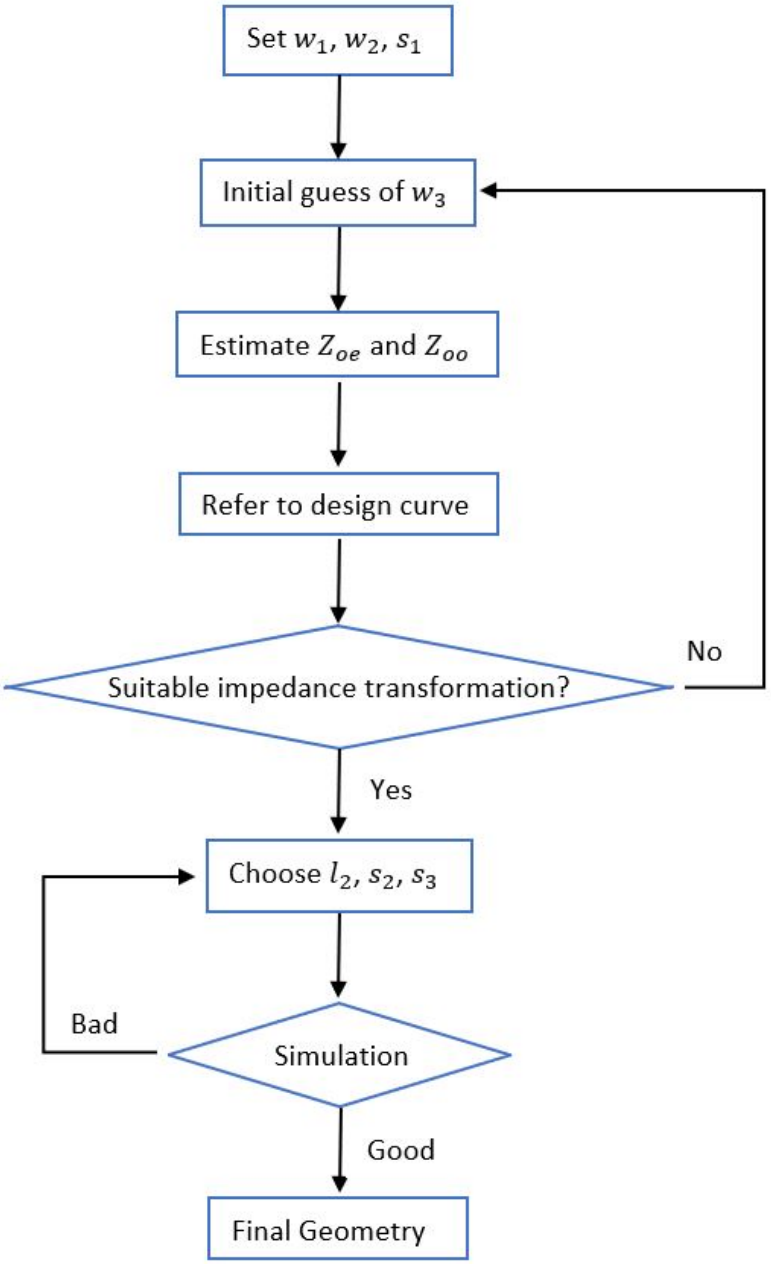

Figure 4.15: Flow diagram of design procedure for modified Marchand balun.

Finally, the configuration of the balanced output lines is set. The output lines are placed above the ground plane slots, thereby increasing the respective impedances. The length of the output lines is kept short to coincide with the region of the slot. The balanced lines extend out from the coupled-line sections and are initially placed close together, but this results in unwanted coupling. The balanced lines therefore need to be separated in some manner.

The parameter, s_2, represents the separation, and thus effectively the shortening of the $\lambda/4$ coupled-line sections. The value of s_2 must remain small to preserve balun performance, but this implies that the coupling on the output lines will be high. Strong coupling can be avoided by further separating the output lines by means of s_3. The value of s_3 must also remain small to prevent back coupling between the output lines and the coupled-line sections, but it must be large enough to minimize coupling between the balanced lines. Separation of at least 5 mm, given the balanced line trace width of 0.5 mm, ensures that coupling between the balanced lines is reduced and has a minimal effect on performance of the balun. The parameters l_2, s_2 and s_3 are then varied systematically until the simulated performance of the balun is acceptable. The output lines are made to converge toward the centre of the structure, so that a surface mount resistor can be connected at the balanced end. The pads and spacing are designed to accommodate a 300 Ω 1206 surface mount device (SMD) resistor.

Equivalent Transmission Line Model

The analysis of the Marchand balun highlights the importance of the even- and odd-mode impedances of the coupled-line structures. The ability to determine these values is crucial to the design. However, it is not immediately clear what the values of the even- and odd-mode impedances are for different aperture sizes. A method of analyzing the balun and its respective even- and odd-mode impedances for different aperture sizes is needed.

The balun shown in Fig. 4.14 is a difficult structure to analyze from first principles. This is due to its unconventional structure and various inter-dependencies on account of the ground plane slots that influence the characteristics of the coupled-line sections, as well as the balanced output lines. Another option is to use full-wave simulations to classify the balun, but CST MWS is unable to provide the even- and odd-mode impedances of the coupled-line sections in the context of the entire balun structure. Therefore, an equivalent transmission line model of the full-wave balun is designed in AWR MWO, so that the characteristics of the balun can be analyzed.

The equivalent ideal transmission line model of the modified Marchand balun is implemented in AWR MWO. It consists of a 50 Ω input port, two coupled-line sections with tunable parameters, a balanced output transmission line pair and a variable differential load. The equivalent model is generated by first importing the reflection coefficient of the full-wave balun into AWR MWO. The reflection coefficient of the equivalent model is then matched to the imported reflection coefficient. Multiple instances of the reflection coefficient, with different load terminations, are imported to improve the accuracy of the estimation. During this process, everything besides the load terminations must remain fixed so that the comparison is not corrupted. The Smith chart representation of the input impedance is also used to support the modelling process.

Fig. 4.16 shows the result of the modelling process in AWR MWO. The reflection coefficients and Smith chart results for three different load terminations are presented. The reflection coefficients of the equivalent model compare reasonably well to the full-wave simulations, with the exception of some minor discrepancies.

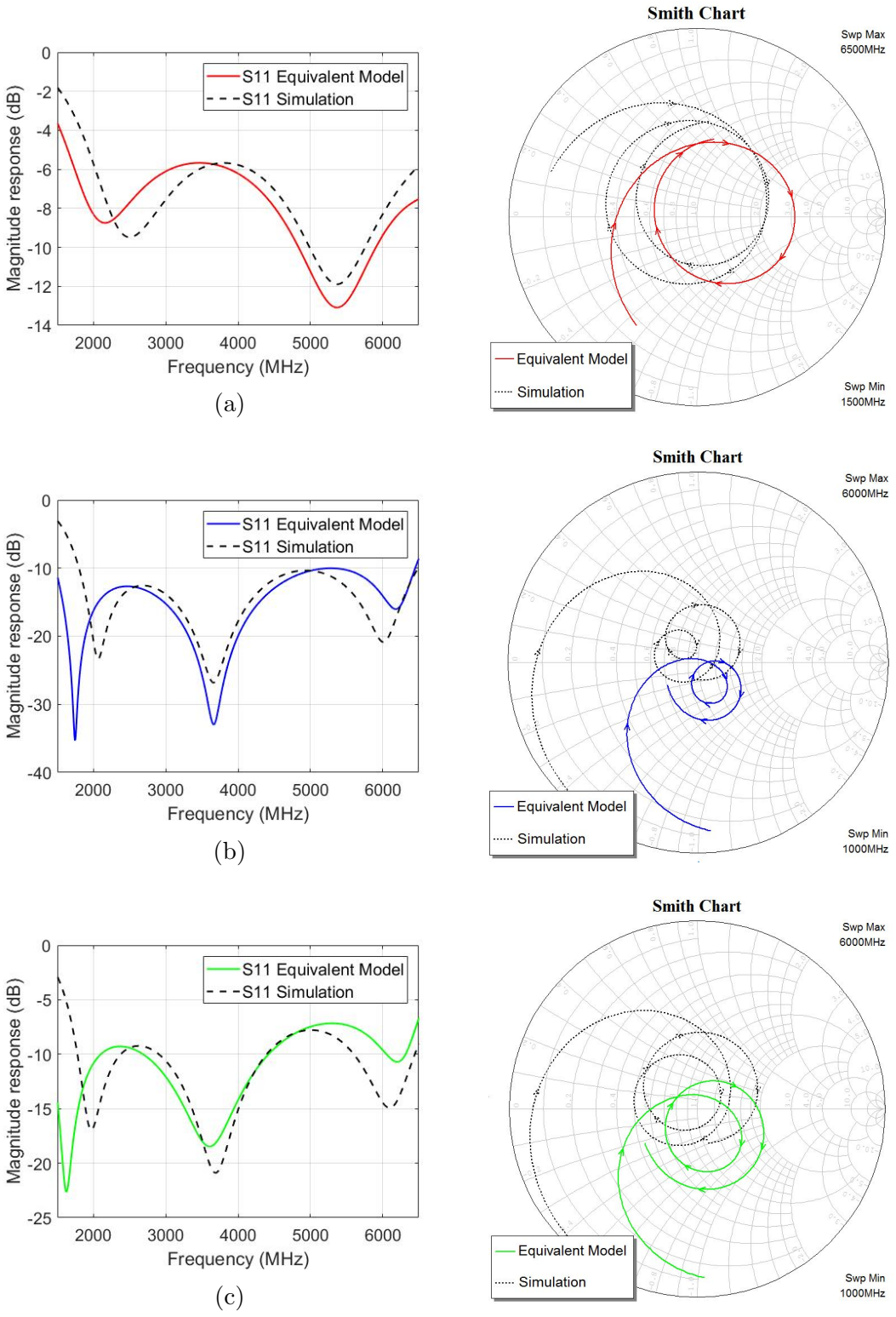

Figure 4.16: Equivalent transmission line model vs full-wave model for different termination impedances. (a) 100 Ω termination (b) 300 Ω termination (c) 400 Ω termination.

The discrepancies relate to slight differences in magnitude, and frequency shifted results of the reflection coefficients. This is expected, since the full-wave case has been implemented microstrip format, while the ideal case has not. The Smith chart results of the full-wave simulations coincide with this idea. The Smith chart input impedance results, Z_{11}, are shown to be very similar to the modelled case except for a slight upwards shift indicating higher inductive reactance for the simulated case. The even- and odd-mode impedances of the coupled-line sections can be estimated with relative certainty.

4.3 Practical Results and Discussion

4.3.1 Initial Design

The manufactured prototype device in Fig. 4.17 has been designed using the method described in Section 4.2.3. The connector is attached a $\lambda/4$ away from the coupled-line sections to minimize its effect on the balun performance. The simulated and measured reflection coefficient results, S_{11}, are shown in Fig. 4.18. There is a significant difference between the measured and simulated responses. The measured reflection coefficient is poor between 3.4-5.3 GHz, reaching -7 dB at 4.38 GHz.

The significant differences suggest a difference between Z_{0e} and Z_{0o} of the simulated and manufactured boards. Initially, it was thought to be some unexpected influence of the slot that was not modelled or simulated correctly, or a problem with the estimation of Z_{0e} and Z_{0o} parameters. However, it was later found that some of the dimensions of the constructed balun were incorrect. This disparity was due to the inaccuracy of the etching equipment used, and resulted in differences in Z_{0e} and Z_{0o}, as initially predicted. Consequently, the expected results were not obtained.

Table 4.1 shows the difference between the actual and simulated dimensions of the balun, and gives some insight into the poor performance of the balun. The considerable difference between the simulated and actual dimensions of s_1 contributes significantly to the degraded results, as s_1 is largely responsible for the coupling factor. The differences in the shortening of the coupled-line sections, s_2, are also responsible for the degraded results.

Table 4.1: Actual and simulated balun dimensions.

Design Parameter	**Simulated (mm)**	**Actual (mm)**
w_1	1.86	1.74
w_2	0.5	0.5
w_3	7.86	8
s_1	0.15	0.32
s_2	0.5	0.65
s_3	5.8	5.95

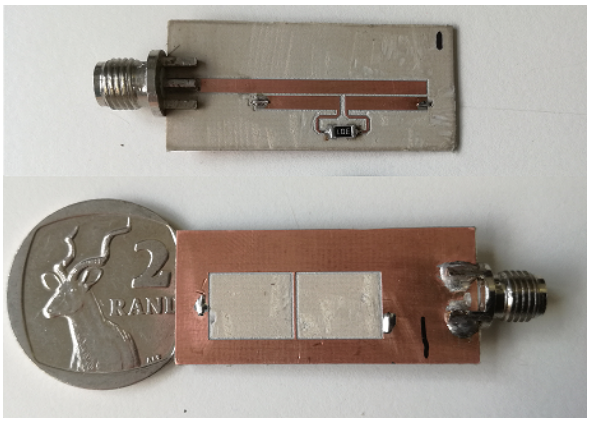

Figure 4.17: Top and bottom view of manufactured balun prototype.

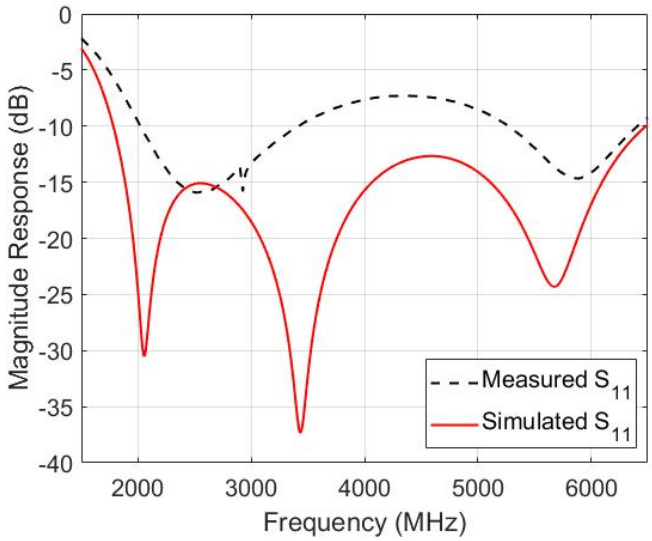

Figure 4.18: Simulated and measured reflection coefficient.

The actual dimensions of the fabricated test board listed in Table 4.1 are used to recreate the manufactured balun in CST MWS. A comparison of the simulated structure with adjusted dimensions and the measured reflection coefficient results is shown in Fig. 4.19. These results show a good correlation between the simulated and measured case, and prove that the original results are mostly incorrect due to a difference in the dimensions of the simulated and manufactured boards.

Due to the manufacturing problems, fabrication of the balun was outsourced to an external manufacturer that could meet the etching requirements for the balun. This opportunity was used to improve some aspects of the prototype test device, such as the location of the connector and the spacing between the pads for the surface mount device (SMD) resistor.

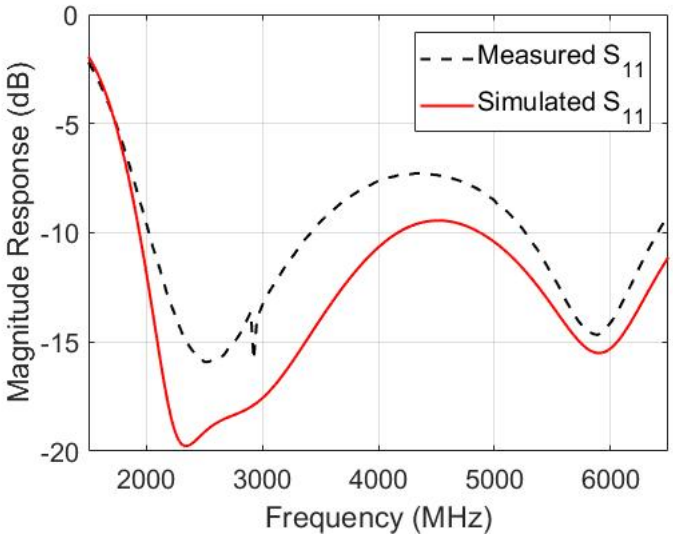

Figure 4.19: Comparison between simulated and measured reflection coefficient results with adjusted dimensions to coincide with the manufactured balun.

4.3.2 Improved Marchand Balun Design

The second iteration of the designed baluns are presented in Fig. 4.20. These test devices allow partial characterization of the balun without the need for connectors at the output lines. The terminated load test device on the right side of Fig. 4.20 is used to characterize the return loss. The differential load impedance is Z_L=300 Ω to match the differential input impedance of the antenna. Fig. 4.20 on the left, also shows the back-to-back test device used to characterize the insertion loss. The insertion loss of a single balun is then half of the through insertion loss S_{12}. The characterization of the amplitude and phase balance is complicated given the structure of the test devices, and will be verified in simulation only. The updated design parameters of the balun test devices are summarized in Table 4.2.

Table 4.2: Design parameters of printed Marchand balun.

Design Parameter	Value	Description
w_1	1.86 mm	Coupled-line section trace width.
w_2	0.5 mm	Output-line trace width.
w_3	7.86 mm	Width of the slot.
l_1	10 mm	Length of the slot.
l_2	5.6 mm	Length of output lines.
s_1	0.15 mm	Separation between coupled lines.
s_2	1 mm	Separation between coupled sections.
s_3	4.8 mm	Separation between output lines.

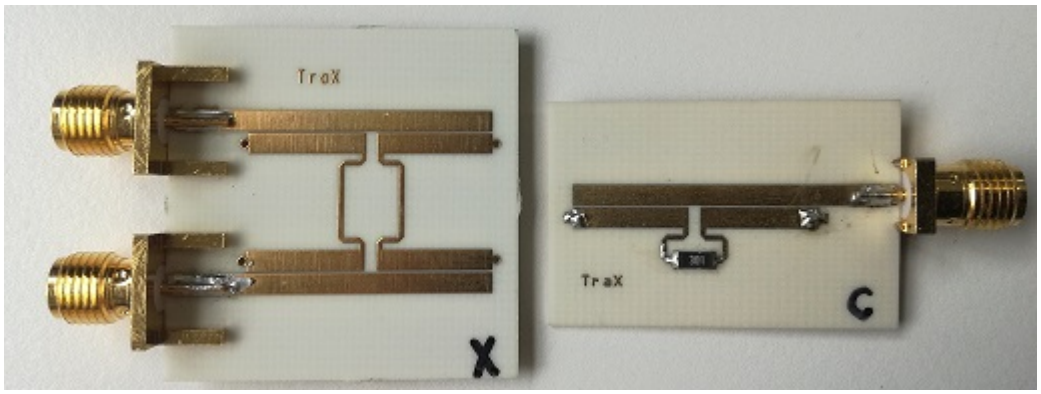

Figure 4.20: Second iteration of manufactured balun prototypes. Back-to-back prototype (Left) Terminated prototype with 300 Ω SMD resistor (Right).

A slot width of 7.86 mm results in an even-mode impedance of 268 Ω, and an odd-mode impedance of 50.3 Ω. This provides the desired impedance transformation of approximately 50-150 Ω according to the design curves. The slot is also compact enough to ensure that the lengths of the balanced output lines are short. The estimated impedance of the 0.5 mm line in the presence of the slot was determined to be approximately 115 Ω, providing a a slightly better, but not ideal, match to the load.

Results

The performance of the prototype test devices is presented in Fig. 4.21. The return and insertion loss results are shown in Fig. 4.21a and Fig. 4.21b respectively. The simulated S_{11} is better than 10 dB across a wide operating frequency range of 1.8 GHz to 6.5 GHz and easily meets the desired 3:1 bandwidth ratio. The measured S_{11} coincides well with the simulated response. The differences between the simulated and measured cases are as a result of manufacturing and can be improved through optimization of the balun. The simulated S_{21} of the back-to-back balun, shown in Fig. 4.21b, is halved to obtain the equivalent insertion loss of a single balun. The equivalent insertion loss is better than 0.25 dB across more than half the desired operating band and reaches a maximum value of 0.84 dB at 5.65 GHz. The measured S_{21} closely follows the simulated trend with a slight shift up in frequency, most likely due to the manufacturing process.

The simulated amplitude and phase balance are depicted in Fig. 4.21c and Fig. 4.21d respectively. The actual amplitude and phase balance are assumed to be similar to the simulated case, as other simulated and measured results were in agreement. The amplitude balance is better than 0.3 dB for most of the band with a maximum value of 0.76 dB at 6 GHz. The phase balance is better than 2° across the band up to 4 GHz, after which it deteriorates rapidly with a maximum value of 12°. This is attributed to the design parameter s_3, as smaller values of this parameter lead to better phase balance at higher frequencies, but also to increased coupling on the output lines.

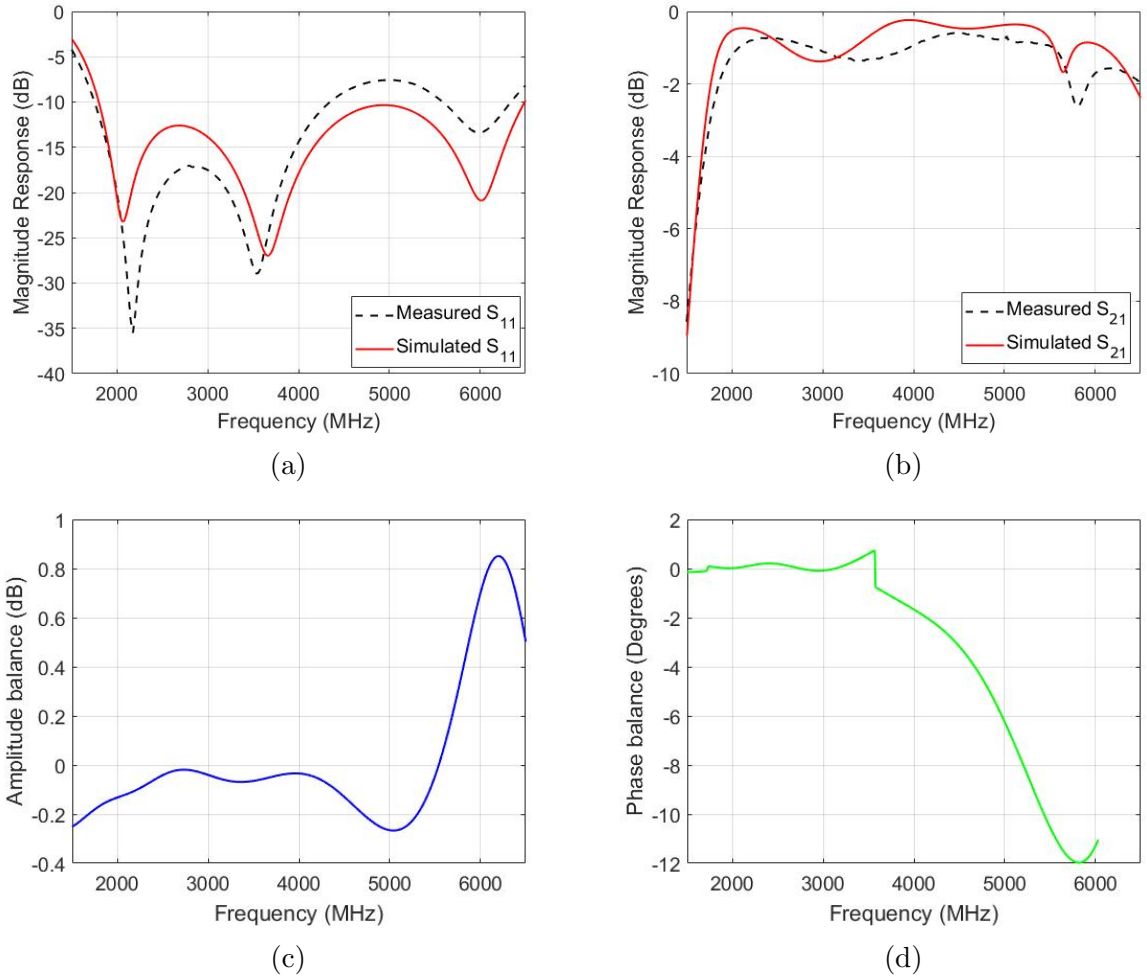

Figure 4.21: Simualted performance results (a) Simulated and measured reflection coefficient (b) Simulated and measured insertion loss (c) Simulated amplitude balance (d) Simulated phase balance.

4.4 Summary

The structure of the balun was carefully considered during the planning phase, so that it could accommodate the dual-polarized implementation of the sinuous antenna. The effect of ground plane apertures beneath coupled-line sections was investigated and then extended in order to design a wideband planar Marchand balun. A procedure for the design of the full-wave balun was provided, along with a technique for estimating the even and odd-mode impedance of coupled-line sections.

The design of a microstrip coupled-line balun with a modified ground plane was presented. The purpose was to develop a wideband planar Marchand balun with good balance, insertion and return loss characteristics as per specification.

The actual performance of the fabricated prototype test devices correspond well with simulated predictions. The return loss is better than 10 dB, and the insertion loss is better than 0.84 dB across the band from 2-6 GHz. The simulated amplitude balance is better than ± 0.6 dB, however, the phase balance deteriorates to 12° between 4-6 GHz. There is room for improvement with regard to the return loss and phase balance. Further optimization of the balun should solve these problems. Overall though, the balun prototype delivers good performance, as well as meeting the original specifications.

Chapter 5

Coaxial Marchand Balun

The modified Marchand balun in Chapter 4 achieved acceptable reflection coefficient, insertion loss and amplitude balance results. However, the bandwidth ratio of the printed case is limited to approximately 3:1. The coaxial version of the Marchand balun can achieve bandwidths in excess of 10:1 and is therefore proposed for integration with the sinuous antenna.

This chapter starts by introducing the coaxial Marchand balun. The theory and operation of the balun is described with reference to a transmission line equivalent model. Next, the closed-form impedance expressions that provide a Chebyshev passband response are presented for the fourth order balun. The full-wave simulation design of the coaxial Marchand balun describes the procedure and considerations behind implementing a 3D model. The coaxial Marchand balun is then manufactured and tested against simulated predictions. The various challenges that emerged during the design process to the manufacturing of the balun are described, and managed.

5.1 Theoretical Background

The transmission line equivalent circuit of a compensated, or fourth order, Marchand balun is presented in Fig. 5.1. A compensated Marchand balun simply refers to the addition of a series open-circuited stub, Z_b, which provides impedance compensation for the shunted resonant cavity [25]. The balun effectively acts as a multi-element band-pass network [18], and can provide impedance transformation over a wide bandwidth.

The single-ended source impedance is given by Z_0 and the balanced load is given by R. The shunted short-circuited stub sections with impedances $Z_{ab}/2$ represent the resonant $\lambda/2$ cavity shunting the balun junction. The series open circuit stub, Z_b, is added to maintain the symmetry of the structure and to compensate for the shunting effects of the resonant line. The line sections Z_1 and Z_4 are included for impedance transforming purposes. Each of the aforementioned sections is made $\theta = \pi/2$, relative to wavelength, to provide flexibility for matching purposes.

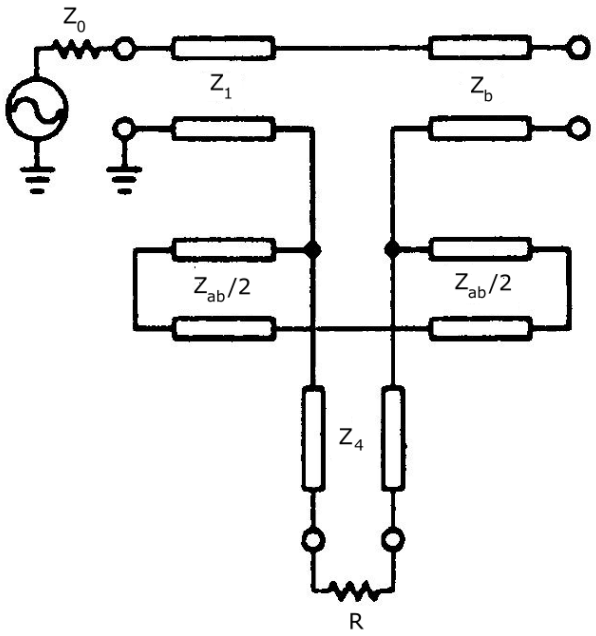

Figure 5.1: Compensated Marchand balun [18].

The outer conductors of the inner coaxial lines and the shield also form a complementary coaxial line with impedance $Z_{ab}/2 + Z_{ab}/2$.

5.1.1 Chebyshev Passband Synthesis

The circuit element values of the Marchand balun are often designed according to some desired passband response. The compensated Marchand balun designed in [45] is based on this technique. Exact, non-redundant synthesis methods for general transverse electromagnetic (TEM) filters presented in [41] are used to calculate element values for a Chebyshev passband response. The Chebyshev passband response is ideal for this application due its equal-ripple properties and increased bandwidth compared to a binomial response.

More recently in [46], closed-form expressions for a Chebyshev passband response are also derived from the general expressions presented in [41]. Closed-form expressions are convenient as they allow for straightforward calculation of the element values using software. The magnitude of the reflection coefficient for the design of Marchand baluns with a Chebyshev passband response is given by [46],

$$|\rho|^2 = \frac{\epsilon^2 M_n^2(\theta, \theta_c)}{1 + \epsilon^2 M_n^2(\theta, \theta_c)}, \tag{5.1}$$

$$M_n(\theta,\theta_c) = T_2\left(\frac{\tan\theta_c}{\tan\theta}\right)T_{n-2}\left(\frac{\cos\theta}{\cos\theta_c}\right) - U_2\left(\frac{\tan\theta_c}{\tan\theta}\right)U_{n-2}\left(\frac{\cos\theta}{\cos\theta_c}\right). \tag{5.2}$$

A description of the parameters is given below:

- ϵ is a constant relating to the calculation of $|\rho|_{max}$.
- n indicates a Marchand balun of the nth order.
- θ is the electrical length of the transmission line.
- θ_c is the electrical length of the transmission line at the lower cutoff.
- $T_2(x)$ and $U_2(x)$ are the Chebyshev polynomials of the first and second kind respectively.

The Chebyshev polynomials of degree $(n-2)$ can be calculated by

$$T_{n-2}(x) = \cos[(n-2)\cos^{-1}(x)], \tag{5.3}$$

$$U_{n-2}(x) = \sin[(n-2)\cos^{-1}(x)]. \tag{5.4}$$

The number of nulls in the Chebyshev passband response matches the order of the balun i.e. a second order Marchand balun will have two distinct nulls. The ith null of the passband response for an nth order Marchand balun can be determined by setting $M_n(\theta^i_{n0},\theta_c) = 0$ in (5.2) and solving for θ^i_{n0} using numerical analysis, like the bisection method described in [47]. Note that the location of the nulls are symmetrical around $\theta = \pi/2$.

θ_c is related to the proportional bandwidth in the following manner:

$$\theta_c = \frac{\pi}{B+1}, \tag{5.5}$$

with $B = f_{upper}/f_{lower}$. Note that (5.5) is only valid for non-dispersive $\lambda_g/4$ transmission lines that make up the balun.

5.1.2 Closed-form Impedance Expressions

The generalized equivalent circuit of the compensated Marchand balun is shown in Fig. 5.2. The complex source $R_{i1} + X_{i1}$ and load impedance $R_{i4} + X_{i4}$ replaces Z_0 and R while incorporating the potential transforming sections Z_1 and Z_4. This equivalent circuit is necessary to derive the generalized closed-form expressions for the element values of the nth order Marchand balun, as was done in [46].

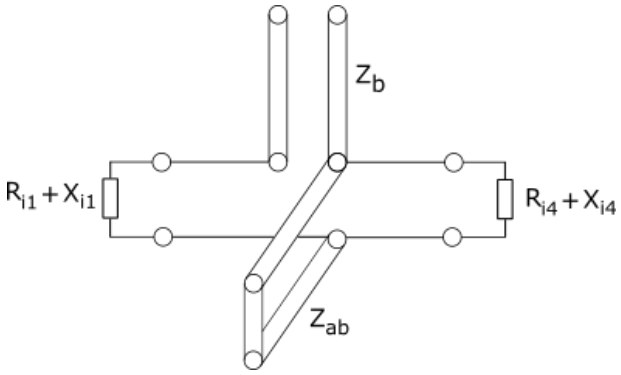

Figure 5.2: Generalized equivalent circuit of the Marchand balun [46].

The general closed-form expressions derived in [46] for the fourth order Marchand balun are described next. The closed-form impedance expressions for the second and third order Marchand baluns are summarized in Appendix B. The expressions for the impedances that follow are normalized with respect to Z_0.

Fourth order Marchand balun

The transmission line equivalent circuit for the fourth order Marchand balun is shown in Fig. 5.3. It is identical to the equivalent circuit in Fig. 5.1 and consists of a $\lambda/4$ transforming section Z_1, the $\lambda/4$ open-circuit stub Z_b, the shunted resonant line impedance Z_{ab} and the $\lambda/4$ transforming section Z_4.

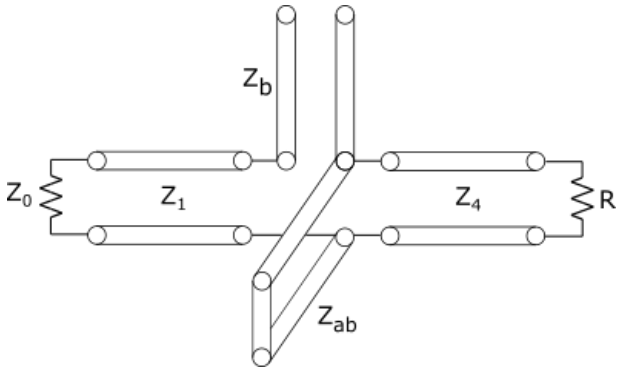

Figure 5.3: Transmission line equivalent for the fourth order Marchand balun.

The procedure for determining the location of the nulls was discussed in Section 5.1.1. Setting $M_n(\theta, \theta_c) = 0$ and numerically solving for θ_{40}^1 provides the dependence of θ_{40}^1 versus B, as depicted in Fig. 5.4. It is important to mention that the values of θ_{40}^1 obtained in Fig. 5.4 are slightly different to those obtained by [46]. The differences are summarized in Table 5.1.

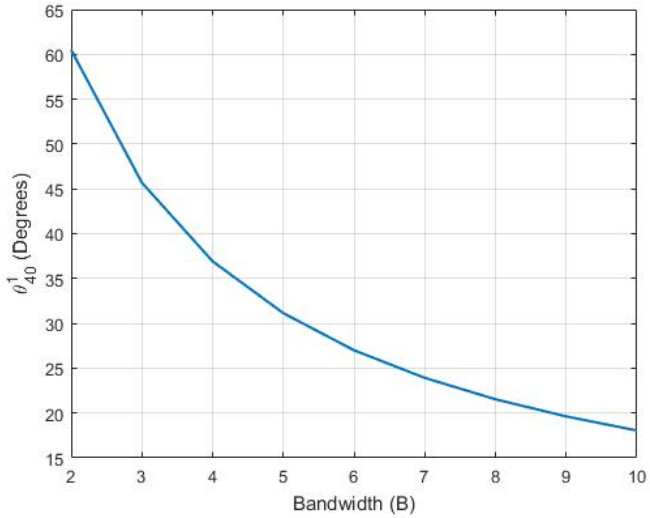

Figure 5.4: Dependence of θ_{40}^1 vs. bandwidth.

Table 5.1: Comparison between θ_{40}^1 values.

B	θ_{40}^1(Degrees)	θ_{40}^1 (Degrees) [46]
2	60.49	62.18
4	36.92	39.40
6	26.99	29.23
8	21.53	23.38
10	18.05	19.54

The difference in the θ_{40}^1 values can be attributed to the stricter tolerance that was applied during numerical analysis. Substituting opposing θ_{40}^1 values presented in Table 5.1 back into (5.2), it is seen that the calculated θ_{40}^1 provides a better estimation of the roots of the equation than that of [46]. These differences are not expected to influence the element values significantly, so either can be used.

Unlike the second and third order Marchand baluns, the derivation of closed-form impedance expressions for the element values Z_1, Z_b, Z_{ab} and Z_4 for the fourth order Marchand balun requires the introduction of an approximation. The reader may refer to [46] for further detail regarding the approximation. In short, the approximation stems from the similarity between a fourth order Marchand balun with a Chebyshev response and a homogeneous fourth order quarter-wave transformer with Chebyshev response. It states that the fourth order balun and the corresponding quarter wave transformer (with identical source and load terminations) have equal reflection coefficient maxima. This results in the following expression:

$$z_1 = a\sqrt{r}. \tag{5.6}$$

The closed-form expressions for a quarter-wave transformer which can be used to solve for (5.6) are [46],

$$a^2 = \left(\frac{1-1/r}{2t_1t_2}\right) + \sqrt{\left(\frac{1-1/r}{2t_1t_2}\right)^2 + 1/r}, \tag{5.7a}$$

$$t_1 = \frac{2\sqrt{2}}{(\sqrt{2}+1)\mu_0^2} - 1, \tag{5.7b}$$

$$t_2 = \frac{2\sqrt{2}}{(\sqrt{2}-1)\mu_0^2} - 1, \tag{5.7c}$$

$$\mu_0 = \sin\left(\pi/2\frac{B-1}{B+1}\right). \tag{5.7d}$$

The closed-form expressions for the remaining element values are as follows [46]:

$$z_b z_{ab} = z_1 z_4 = r, \tag{5.8}$$

$$z_{ab} = -b + \sqrt{b^2 - c}, \tag{5.9}$$

where b and c are given by

$$b = \frac{r_{i1}x_{i4}}{(r_{i1}-r_{i4})\tan\theta_{40}^1}, \tag{5.10a}$$

$$c = \frac{r_{i1}(r_{i4}^2+x_{i4}^2)}{(r_{i1}-r_{i4})\tan^2\theta_{40}^1}, \tag{5.10b}$$

$$r_{i1} = z_1^2\frac{1+\tan^2\theta_{40}^1}{z_1^2+\tan^2\theta_{30}^1}, \tag{5.10c}$$

$$r_{i4} = r\frac{1+\tan^2\theta_{40}^1}{1+z_1^2\tan^2\theta_{30}^1}, \tag{5.10d}$$

$$x_{i4} = r/z_1\tan\theta_{40}^1\frac{1-z_1^2}{1+z_1^2\tan^2\theta_{30}^1}. \tag{5.10e}$$

In conclusion, the element values of Marchand baluns that showcase Chebyshev passband response for different orders ($n = 2, 3, 4$) can be designed for various bandwidths according to closed-form equations presented by [46].

5.1.3 Graphs of Circuit Elements

The study conducted by Cloete in [45] compared the magnitude of the reflection coefficients for second, third and fourth order baluns with load impedances of R=100 Ω and bandwidths of B=10. It was stated that the second order balun was not suitable for load impedances greater than approximately 75 Ω, as this resulted in an insufficient match. The third order balun, with a $\lambda/4$ transformer placed before the load, exhibited significant improvement over the second order balun for bandwidths up to about B=4, but lost its effectiveness for larger bandwidths. The fourth order balun, with $\lambda/4$ transformers placed at the balanced and unbalanced ends, was created to enhance the effectiveness for larger bandwidths and resulted in a reflection coefficient better than -14.9 dB. A summary of the results is presented in Table 5.2.

The coaxial Marchand balun being designed for the sinuous antenna needs to provide a 50-300 Ω impedance transformation over a large bandwidth. Thus, the fourth order version of the Marchand balun is the clear choice for implementation as it can provide a better impedance match than the second and third order versions. However, the impedance transformation over a bandwidth of $B = 10$ seems unlikely given the results in [45]. This is confirmed by Fig. 5.5 which displays the element values Z_1, Z_b, $Z_{ab}/2$, Z_4 and R for the fourth order Marchand balun as a function of the reflection coefficient. The graphs of the elements values are created by first varying the load impedance R between 60-300 Ω, producing a unique Z_1, Z_b, $Z_{ab}/2$, Z_4 for each R value. These element values for various R are then included in a schematic version of the fourth order balun which generates the reflection coefficient results.

Fig. 5.5 shows that for impedances greater than $R = 150$ Ω, the reflection coefficient is worse than -10 dB. Specifically, the reflection coefficient for R=300 Ω is -5.45 dB which is not a suitable match. Even so, the other element values dependant on R=300 Ω are reasonable and practically feasible. In order for the fourth order balun to provide a 6:1 impedance transformation with a suitable match, the bandwidth has to be reduced.

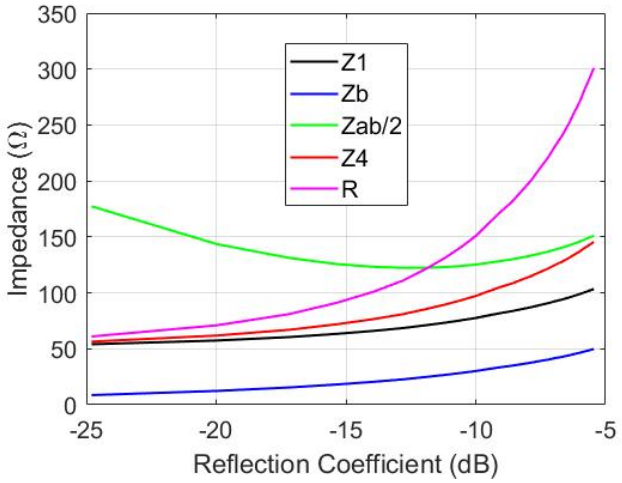

Figure 5.5: Graph of circuit elements for $n = 4$ Marchand balun.

Table 5.2: Comparison of nth order Marchand baluns for B=10, Z_0=50 Ω and R=100 Ω [45].

Order	Z_1 (Ω)	Z_b (Ω)	Z_{ab} (Ω)	Z_4 (Ω)	$\|\rho\|_{max}$ (dB)
2	–	21	241	–	-9.5
3	–	17.5	215	70.7	-12.4
4	65	20	250	76	-14.9

5.2 Electrical Design

The impedances of the ideal Marchand balun, namely Z_1, Z_b, Z_{ab}, have to be related to applicable coaxial dimensions. The formula for calculating the the impedance of a coaxial line is given by [17],

$$Z = \sqrt{\frac{\mu}{\epsilon}} \frac{\ln(b/a)}{2\pi}, \tag{5.11}$$

where b/a is the ratio of the outer radius to the inner radius of the coaxial structure.

The impedance, Z_4, has to be related to parallel circular conductor dimensions. The formula for calculating the impedance of parallel circular conductors is given by [17],

$$Z = \frac{120}{\sqrt{\epsilon_r}} \cosh^{-1}(D/d), \tag{5.12}$$

where D is the distance between the centres of the conductors and d is the diameter of the circular conductors.

5.2.1 Ideal Fourth Order Marchand Balun

The ideal model of the fourth order Marchand balun, shown in Fig. 5.6, is created as a first step in the design process. It consists of the impedance transforming sections Z_1 and Z_4, as well as the shunted short circuit stub Z_{ab} and the series open circuit stub Z_b. The $\lambda/4$ sections are set to 25 mm, so that f_{centre}=3 GHz.

The balun shown in Fig. 5.6 is specified for a bandwidth B=5 and load R=300 Ω. The relevant impedances Z_1, Z_b, $Z_{ab}/2$ and Z_4 can be determined using the closed-form expressions for the element values given for the fourth order balun with θ^1_{30}=33.15° and θ^1_{40}=31.14°.

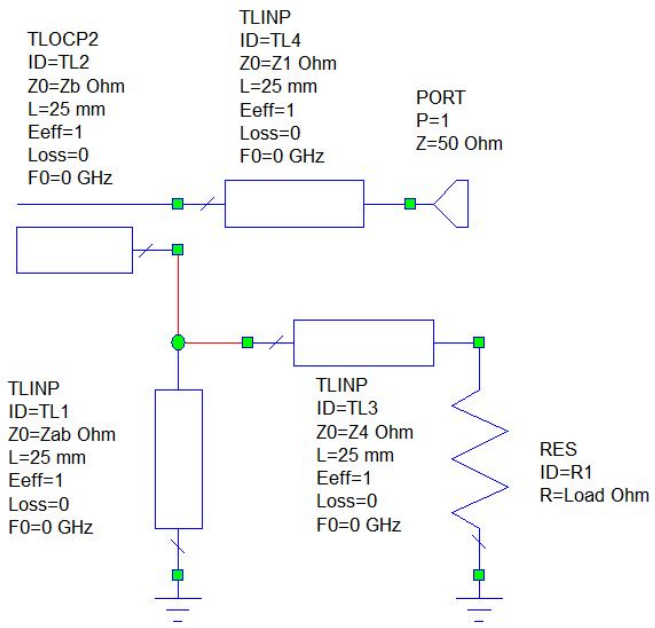

Figure 5.6: Ideal fourth order Marchand balun.

The resulting default reflection coefficient is shown in red in Fig. 5.7. The default S_{11} is not equi-ripple; the first and last maxima have a magnitude of -8.54 dB, while the maxima in the centre has a magnitude of -13.2 dB. The reason is attributed to the approximation made during the derivation of the closed-form expressions, and the reduced effectiveness of the quarter-wave transforming sections due to the 6:1 impedance transformation requirement over a wide bandwidth.

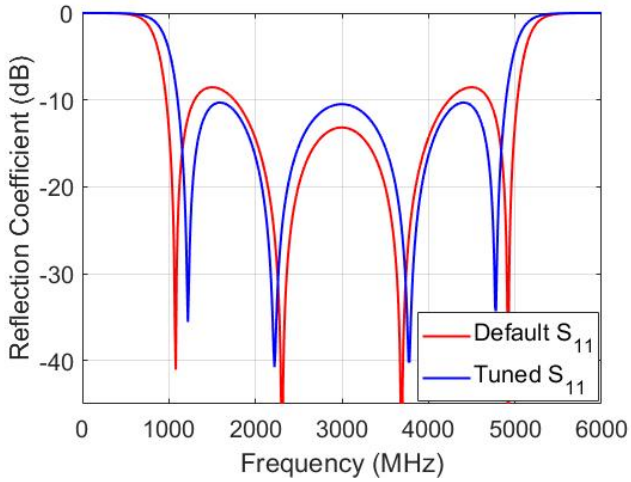

Figure 5.7: Default and tuned reflection coefficient of ideal fourth order Marchand balun.

The element values of the balun can be tuned in order to provide an equi-ripple response, as shown in blue in Fig. 5.7. The change in element values is given below,

$$\begin{aligned} Z_1 &: 87.6\,\Omega \rightarrow 90\,\Omega \\ Z_b &: 87.7\,\Omega \rightarrow 104\,\Omega \\ Z_{ab} &: 171.1\,\Omega \rightarrow 137\,\Omega \\ Z_4 &: 171.5\,\Omega \rightarrow 165\,\Omega \end{aligned}$$

The tuned S_{11} is better than -10.32 dB between 1.1-4.9 GHz which is a proportional bandwidth of 4.5:1. This is close to the optimal achievable bandwidth for an equi-ripple response with a balanced load of 300 Ω.

5.2.2 High Order Modes in Resonant Coaxial Cavity

The resonant cavity of the coaxial Marchand balun is an important aspect to consider during the design phase for several reasons. The cavity serves to shield the device from outside interference and its dimensions determine the shorted stub impedance Z_{ab} which is necessary for proper balun operation. The design of the inner and outer diameters of the cavity is quite flexible because the desired impedance can be achieved for a multitude of different inner and outer diameter dimensions. However, there is an issue that arises with this approach. Increasing inner diameter dimensions, d, leads to increasing outer diameter dimensions, D. This has no effect on the impedance of the device as D/d remains constant, but it does result in severe degradation of balun performance which is investigated in this section.

Fig. 5.8 presents the cross-sections of two realizations of the circular coaxial Marchand balun with identical impedances as implemented in CST MWS. Fig. 5.8a depicts a balun with a smaller cavity and Fig. 5.8b depicts a balun with a larger cavity. The insulating material is air, so that $\epsilon_r = 1$. The physical dimensions of the two realizations are different, but the structures remain proportionally the same, and therefore the impedances are preserved. The impedances Z_1, Z_b, Z_{ab}, Z_4 from the ideal model are carried over to the full-wave simulation.

The diameter of the outer conductor and shield of Z_0 forms the inner conductor of the coaxial cavity Z_{ab}, denoted by d. The outer conductors and shields of Z_1 and Z_b are also made equal to d. This is not a necessity, but it greatly simplifies the implementation of the balun. For instance, if the diameters of Z_1 and Z_b are made unique, the length of the parallel conductors would be dissimilar, causing phase variation at the input of the antenna. The diameter of the outer conductor of the coaxial cavity Z_{ab} is denoted by D.

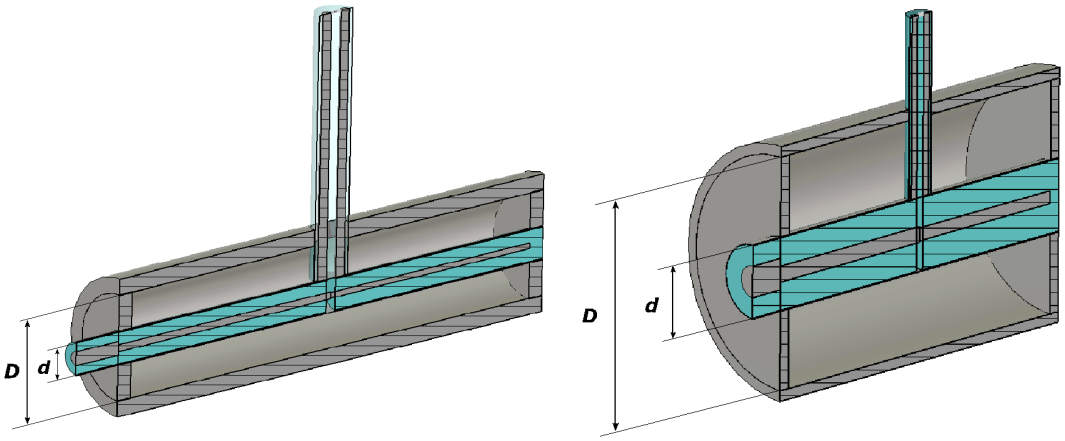

(a) (b)

Figure 5.8: Cross section of coaxial Marchand balun in CST MWS. (a) d=3.2 mm, D=10.038 mm (b) d=10.2 mm, D=32 mm

The inner diameter, d, is varied between 3.2-20.2 mm and the balun performance is studied. The reflection coefficient for different d, and consequently different D, is shown in Fig. 5.9. The d=3 mm implementation, in red, actually performs almost identically to the dashed ideal model simulated in the previous section. However, S_{11} deteriorates rapidly for increasing d. The most likely explanation for the degradation of S_{11} is that higher order modes are being excited due to the resulting large cavity.

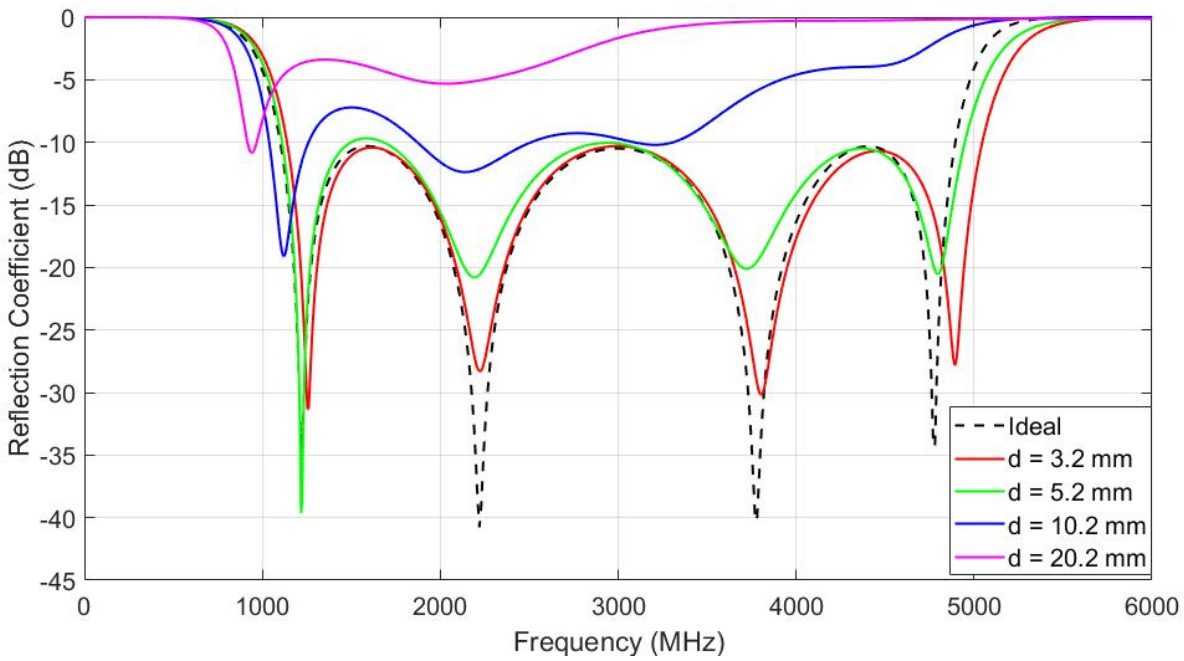

Figure 5.9: Simulated reflection coefficient results for varying d values.

A brief study of higher order mode cutoff frequencies in coaxial transmission lines is now presented. The fundamental mode in a coaxial transmission line is the transverse electro-magnetic (TEM) mode, but higher order transverse electric (TE) and transverse magnetic (TM) modes are also supported. Propagation of two or more modes with different propagation constants can lead to unpredictable results and is generally avoided.

The first higher order mode that propagates in a coaxial transmission line is the TE_{11} mode. An upper limit on the frequency of operation is set to avoid propagation of this higher order mode. The upper limit is determined by the cutoff frequency of the TE_{11} mode given by [17],

$$f_c = \frac{ck_c}{2\pi\sqrt{\epsilon_r}}, \tag{5.13}$$

$$k_c d = \frac{4}{1 + D/d}, \tag{5.14}$$

where, k_c, is the cutoff wavenumber. The calculated cutoff frequencies for the different cross-sections are presented in Table 5.3. The operating frequency of the desired balun is approximately 1-5 GHz and therefore the cutoff frequency for the TE_{11} mode should be well above 5 GHz. The table shows how the cutoff frequency is reduced as d, and consequently the cavity size, D, increases. This correlates well with the degraded reflection coefficient results in Fig. 5.9. Higher order modes will start interfering in the operating frequency band for values larger than d=9 mm.

Table 5.3: Frequency cutoffs for the TE_{11} mode.

Diameter (d)	Frequency cutoff (f_c)
3.2 mm	14.43 GHz
5.2 mm	8.88 GHz
10.2 mm	4.52 GHz
20.2 mm	2.28 GHz

The impact of cavity size and the excitation of higher order resonant modes in standard coaxial resonators is also investigated, in order to complement the study of coaxial transmission line cutoff frequencies. The length of the coaxial resonators are fixed and the other dimensions are chosen to mimic the dimensions of the fourth order balun. The Eigenmode solver in CST is used to analyze the cavity behaviour.

A $\lambda/2$ resonator of length L=50 mm with a large air coaxial cavity is described first and shown in Fig. 5.10a. The required impedance of the cavity is $Z_{ab}/2$=68.5 Ω. If the diameter of the centre conductor is specified arbitrarily as d=20.2 mm then the diameter of the outer conductor is d_b=64 mm according to (5.11). The fundamental mode of a circular coaxial resonator is $TM_{0,0,n}$. The resonant frequency of this mode is given by [48],

$$f_{0,0,n} = \frac{cn}{2L}, \tag{5.15}$$

where n is a natural number. The resonant frequency of the fundamental mode is obtained by substituting n=1 and L=50 mm of the coaxial resonator into (5.15), resulting in $f_{0,0,1}$=2.9970 GHz.

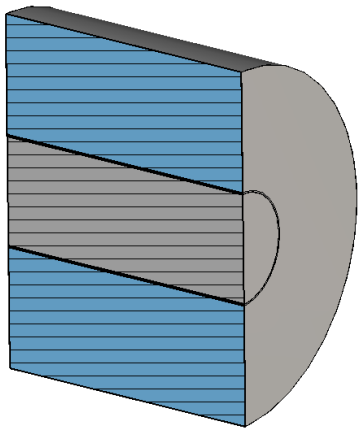

(a)

Eigenmode solver results:

Mode	Frequency	Accuracy
1	2.999005 GHz	6.476e-008
2	3.792221 GHz	3.918e-011
3	3.792238 GHz	2.539e-011
4	5.319936 GHz	1.891e-007
5	5.320027 GHz	1.334e-007

(b)

Figure 5.10: A large coaxial cavity resonator. (a) Sectioned view of a large coaxial cavity. (b) Resonant frequencies for the first five modes.

The desired operating frequency range of the balun is from 1–5 GHz and the table in Fig. 5.10b represents the resonant frequencies of the first five modes in this range. It is noted that the calculated $f_{0,0,1}$ coincides well with Mode 1 as determined by the Eigenmode solver in Fig. 5.10b. The corresponding field configurations of each mode in the table are presented in Fig. 5.11 from left to right. Quick inspection of the results finds that there are several higher order modes propagating in, or close to, the desired operating frequency range. This would explain the poor performance of the balun with a large cavity. Note that Modes 2 and 3, as well as Modes 4 and 5 occur at the same frequencies and can be considered degenerate.

Another $\lambda/2$ resonator of length L=50 mm with a small air coaxial cavity is described next and shown in Fig. 5.12a. If the impedance $Z_{ab}/2$ remains the same as the previous case and the diameter of the centre conductor is chosen as d_a=3.2 mm, the resulting outer diameter is d_b=10.03 mm according to (5.11). The first three modes that propagate within the cavity are shown in the table in Fig. 5.12b. The resonant frequencies of the various modes are not clustered around certain frequencies anymore. Mode 2 and 3 can be ignored, as only Mode 1, with a resonant frequency of 2.9965 GHz, appears across the desired 1-5 GHz frequency range. The resonant frequency of Mode 1 still matches the calculated $f_{0,0,1}$ of (5.15) as expected. This result supports the notion that a small cavity supresses higher order resonant modes.

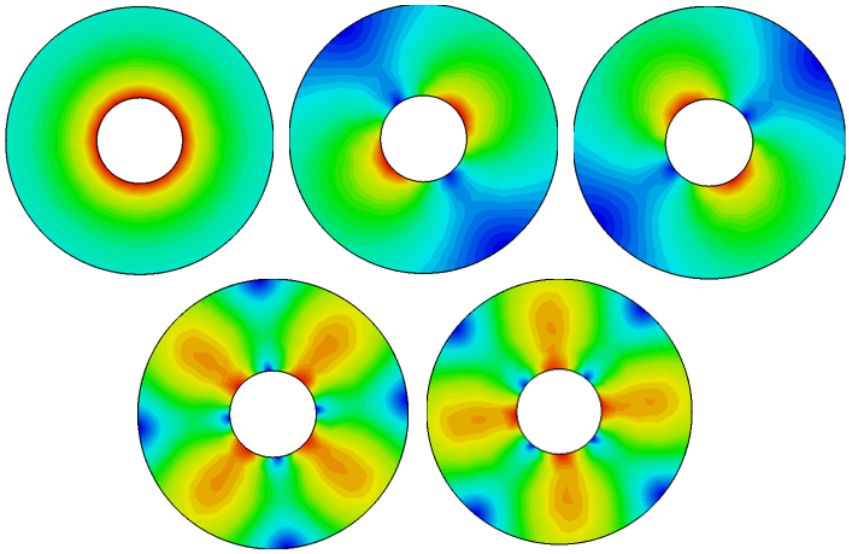

Figure 5.11: E-field configuration for the first 5 modes.

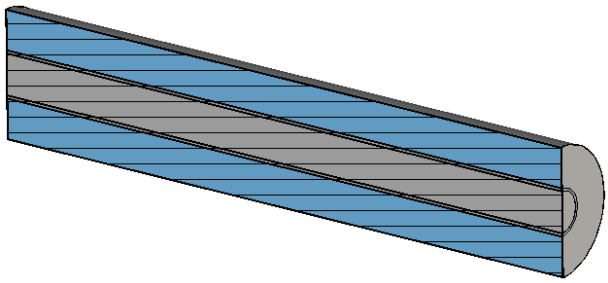

(a)

Eigenmode solver results:

Mode	Frequency	Accuracy
1	2.996475 GHz	3.053e-007
2	5.993939 GHz	1.712e-010
3	8.992474 GHz	3.978e-007

(b)

Figure 5.12: A small coaxial cavity resonator. (a) Sectioned view of a small coaxial cavity. (b) Resonant frequencies for the first three modes.

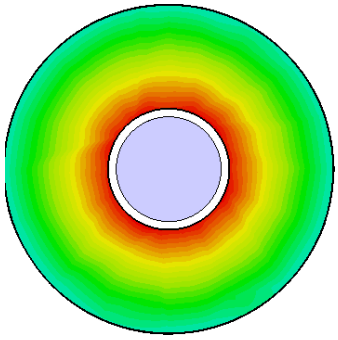

Figure 5.13: E-field configuration for the fundamental TEM mode.

In conclusion, the studies of both the higher order transmission line cutoff frequencies and resonant modes found that the implementation of a small cavity is preferred for the design of the coaxial Marchand balun.

5.2.3 Full-wave Simulations

Standard Rectangular Coaxial Implementation

There are many different ways to implement a coaxial line structure. Fig. 5.14 shows various possible coaxial line implementations from [49]. The circular coaxial Marchand balun shown in Fig. 5.8 is of the type "Shape I" and it has been shown to perform as expected. However, other coaxial realizations should be considered, as the cylindrical structure introduces some difficulties where manufacturing is considered. Small cylindrical structures required for the cavity are difficult to custom-make and the final product cannot be opened or closed in a straightforward manner.

The proposed coaxial structure change is shown as "Shape III" in Fig. 5.14. The rectangular shield of the coaxial line with with the circular inner conductor is appealing because it resolves the issues experienced with the "Shape I" coaxial structure. The impedance of the "Shape III" coaxial structure is given by [49],

$$Z = 138 \log \frac{1.079A}{a}, \tag{5.16}$$

where A is half the side length of the rectangular shield and a is the radius of the circular inner conductor. The relevant dimensions, A, and ,a, for the rectangular coaxial structure can be calculated using (5.16) given a desired impedance.

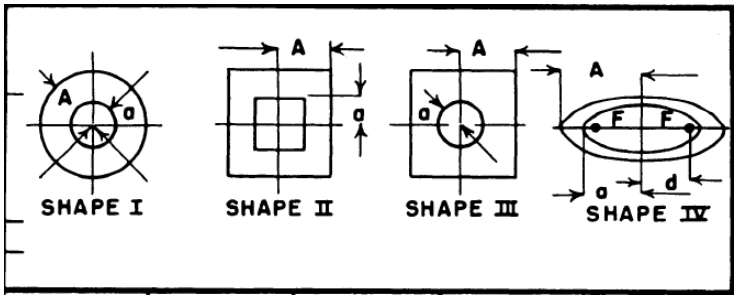

Figure 5.14: Possible coaxial implementations [49].

A cross-section view of the designed rectangular coaxial Marchand balun is shown in Fig. 5.15. The balun is essentially the same as the circular coaxial implementation in Fig. 5.8, except for the rectangular cavity structure. The simulated performance of the balun is presented in Fig. 5.16 and Fig. 5.17.

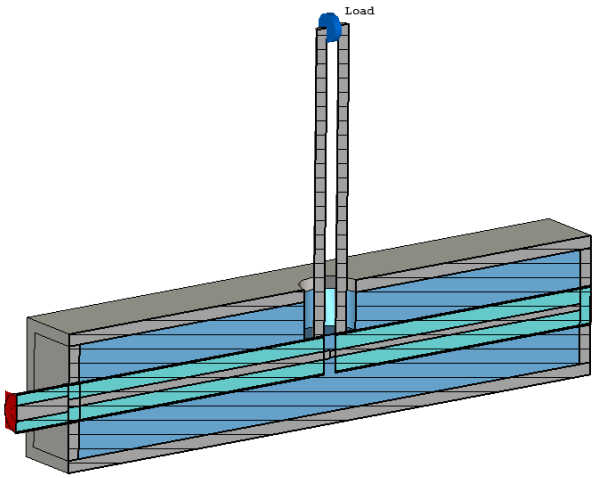

Figure 5.15: Cross-section view of rectangular coaxial Marchand balun.

The reflection coefficient of the simulated balun with a R=300 Ω load is shown in Fig. 5.16a. It depicts an equi-ripple response better than -10 dB across the band from 1.1-5 GHz which is a proportional bandwidth of $B = 4.55$. The back-to-back insertion loss of the simulated balun is shown in Fig. 5.16b and it is better than -0.56 dB across the required band.

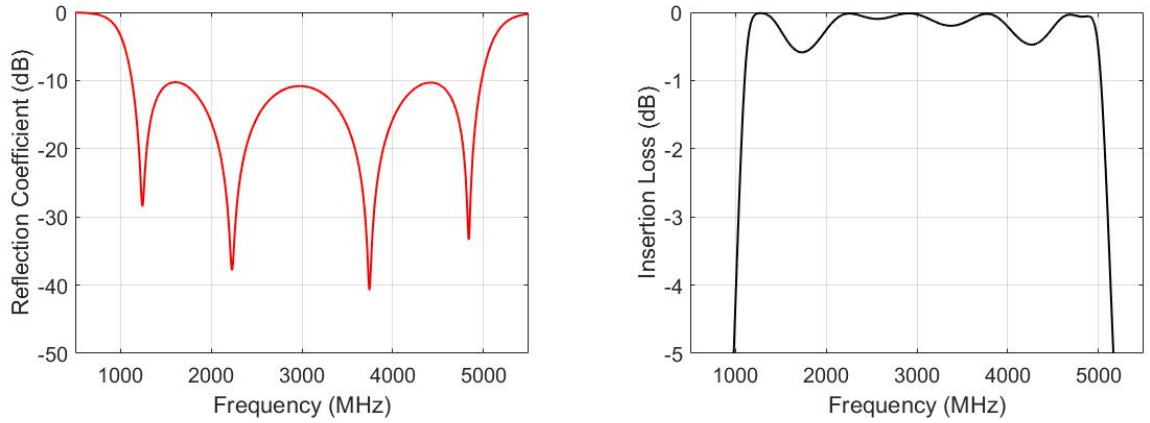

(a) (b)

Figure 5.16: Simulated performance of rectangular Marchand balun (a) Reflection coefficient (b) Back-to-back insertion loss.

The amplitude and phase balance are found by setting up a multi-pin single-ended port across the balanced lines and extracting S_{21} and S_{31}. The amplitude balance shown in Fig. 5.17a is better than 0.2 dB across the required band. Similarly, the phase balance shown in Fig. 5.17b is better than 0.5° across the required band. The balun balance results are excellent and display a marked improvement over the printed balun version.

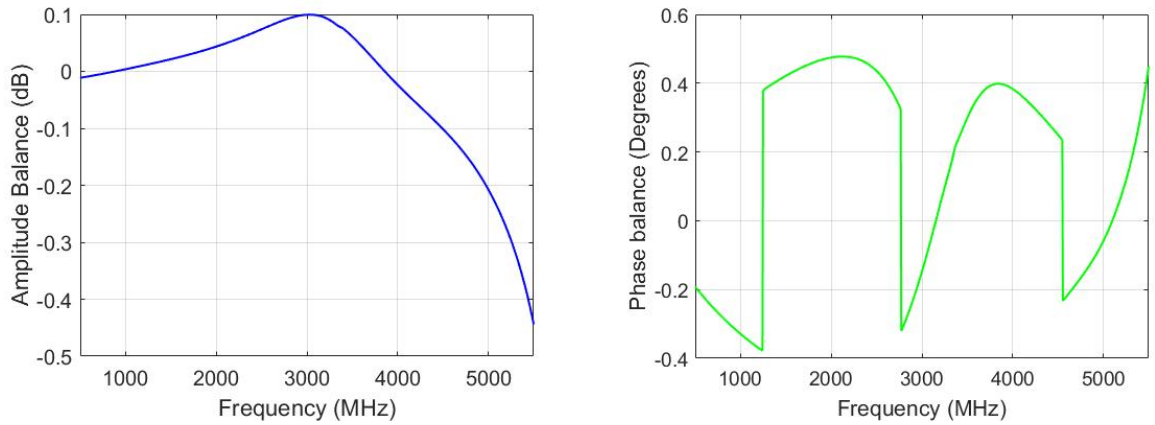

(a) (b)

Figure 5.17: Simulated performance of rectangular Marchand balun (a) Amplitude balance (b) Phase balance

5.3 Practical Results and Discussion

There are several challenges with regard to making the balun in Fig. 5.15 practically realizable. These challenges relate to physical limitations, structural discontinuities and mechanical stability requirements of the coaxial structure. Various parts of the structure in Fig. 5.15 are therefore altered for the purpose of production.

5.3.1 Design I

The sectioned side-view of the modified structure of the rectangular Marchand balun is presented in Fig. 5.18. This structure incorporates the necessary mechanical changes while tuning other dimensions of the balun to preserve the "best" possible reflection coefficient performance. Its design parameters can be found in Appendix C.1. The various challenges are described and the necessary changes shown in the image are described.

The front and back panels of the structure shown in Fig. 5.15 are too thin to include screw holes that are required for securing the separate faces of the rectangular cavity. Therefore, the thickness of the front and back panels was changed from 1.5-3.5 mm. The screw locations securing one of the side panels to the front and back panels are shown in Fig. 5.18.

Noticeable discontinuities are observed between the centre conductors of the connector and Z_1, and at the balun junction between the centre conductors of Z_1 and Z_b in Fig. 5.18. Mechanical sleeve supports are required to form the connection between these centre conductors and to provide extra mechanical support. The size and length of the sleeves should be kept as small as possible in order to preserve balun performance. Therefore, sleeves with a length of 5 mm and a diameter d=2 mm are integrated into the design.

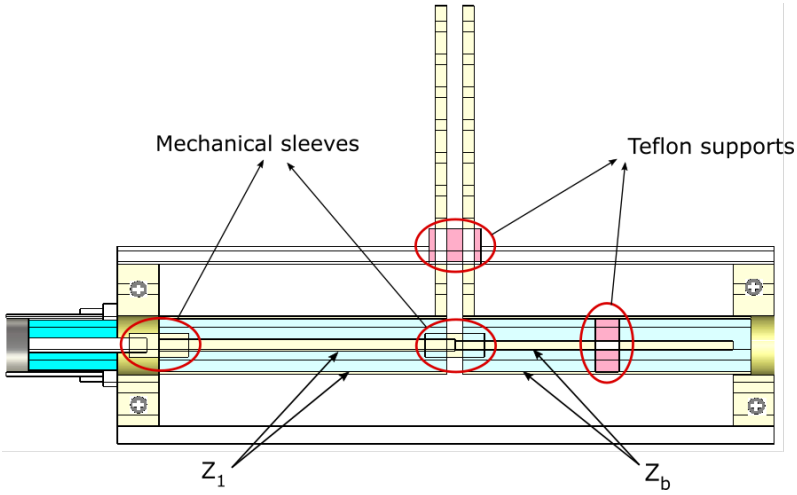

Figure 5.18: Sectioned side-view structure of Design I.

Mechanical stability and accurate compliance with the simulated model for the practical coaxial structure is an important aspect to consider. Air coaxial structures are preferred so that the dimensions b and a in (5.11) are maximised for a given impedance. However, this is cumbersome from a manufacturing point of view, as there is no dielectric material to provide structural reinforcement or to help centre the various sections of the coaxial structure. This is remedied by adding Teflon supports at two critical points in the structure. The first Teflon support with a length of 2 mm and a diameter d=4.55 mm is added at the centre of the Z_b line section. The other Teflon support is approximately 3 mm in length with a diameter d=4.52 mm which surrounds the balanced lines as they exit the cavity structure. These Teflon supports, together with the mechanical sleeves, provide a centred and mechanically stable coaxial structure.

Additional modifications were made to certain dimensions of the coaxial structure to compensate for the mechanical sleeves and Teflon supports. These modifications included minor changes to the impedances and lengths of various line sections. The impedance Z_{ab} changed from 137 Ω to 130 Ω. The length of the balanced lines Z_4 changed from 25 mm to 26.36 mm. The length of the Z_b line section changed from 24.25 mm to 23.25 mm which consequently reduced the length L of the cavity from 50 mm to 48.5 mm. The simulated performance of the modified balun structure is shown in Fig. 5.19 and 5.20.

Simulated Results

The S_{11} shown in Fig. 5.19a is better than -10 dB across the band from 1.1-4.8 GHz. This implies a proportional bandwidth of B=4.25 which is slightly lower than the B=4.55 of the standard rectangular coaxial implementation. The bandwidth reduction is as a result of lowering the impedance Z_{ab} to compensate for the mechanical considerations. The back-to-back insertion loss is shown in Fig. 5.19b. It is better than -0.85 dB across the same band as the reflection coefficient, showcasing similar performance to that of the standard rectangular coaxial implementation.

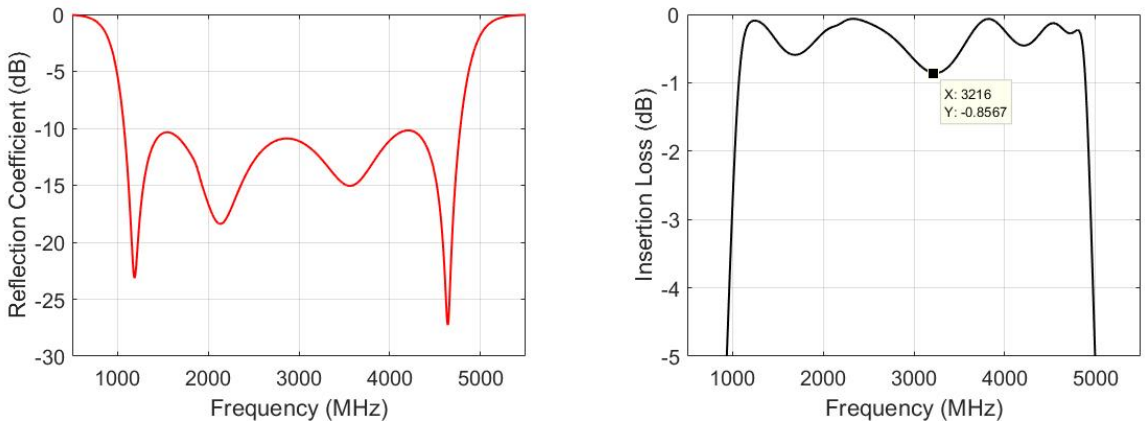

(a) (b)

Figure 5.19: Simulated performance of Design I (a) Reflection coefficient (b) Back-to-back insertion loss.

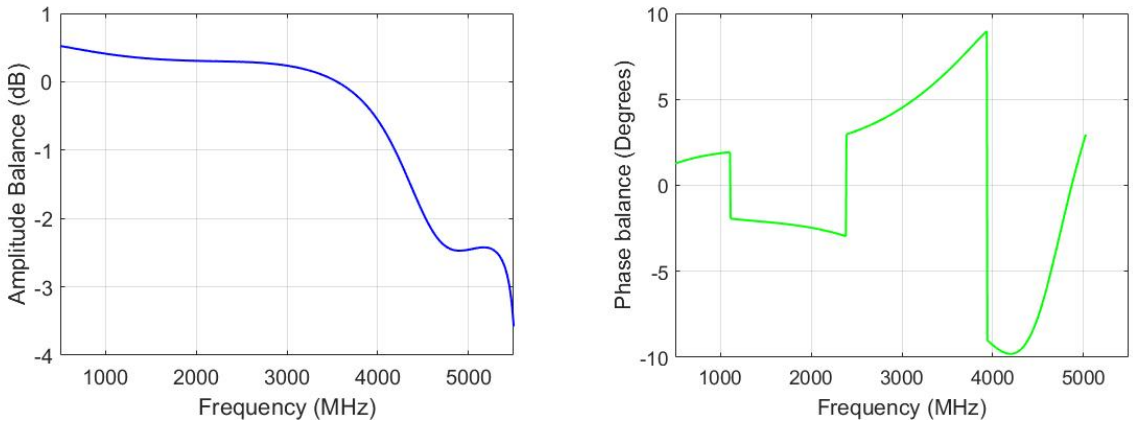

(a) (b)

Figure 5.20: Simulated performance of Design I (a) Amplitude balance (b) Phase balance.

The balance performance of the rectangular Marchand balun is shown in Fig. 5.20. The amplitude balance shown in Fig. 5.20a is better than ±0.5 dB up to 4 GHz, after which it deteriorates rapidly to -2.45 dB at 5 GHz. The phase balance shown in Fig. 5.20b is also shown to perform poorly with the phase difference being 3° at best and 9.8° at its worst occurring at 4.23 GHz. The poor balance performance is partially expected due to the lengths of Z_b and Z_{ab} sections that are tuned to provide suitable S_{11} results. The resulting asymmetry of the device around the balun junction is therefore to blame. The rectangular coaxial Marchand balun of Fig. 5.18 showcased suitable return and insertion loss results even though the balance performance was poor. A prototype rectangular coaxial test device was readied for production in order to confirm the S_{11} and S_{21} results. Future iterations of the balun may focus on improving the balance performance.

Construction and Measurement

The constructed rectangular coaxial Marchand balun is shown in Fig. 5.21a. The inside of the balun can be seen in Fig. 5.21b which shows the side-view of the balun with one of its side panels removed. The inner coaxial line sections Z_1 and Z_b are constructed using commercially available circular brass rods and tubes with small diameters. The selected brass tube has a radius $r_b^{Z_1}$=2.275 mm excluding the wall thickness of 0.225 mm. This results in an inner rod radius of $r_a^{Z_1}$=0.5 mm for Z_1=90 Ω, and $r_a^{Z_1}$=0.4 mm for Z_b=104 Ω which are readily available. The side length A of the rectangular cavity is then A=6.72 mm, so it is small enough to suppress higher order modes.

The fabrication of the balun described in Fig. 5.21 requires careful planning and implementation. The performance of the balun is highly dependant on the achievable accuracy of the structure and its specified dimensions. It is important to confirm whether or not the balun performance is reproducible and consistent. Three duplicates of the balun described in Fig. 5.21 were therefore fabricated and tested and the results are presented in Fig. 5.22.

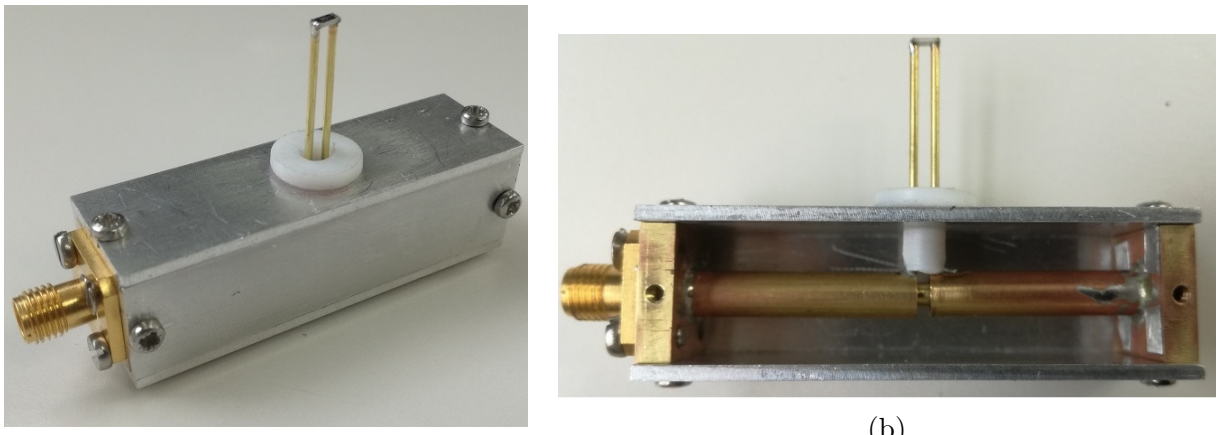

(a) (b)

Figure 5.21: Constructed rectangular Marchand balun.

The results for the three fabricated duplicate baluns labelled Case(s) A to C are compared against one another, along with the simulated results in Fig. 5.22. The S_{11} results for all three cases coincide well with one another, confirming the consistency of the fabrication process. However, the performance of the manufactured baluns doesn't correspond well with the simulated predictions. This is evident when comparing the nulls, maxima and bandwidth of the measured and simulated responses. The simulated response is better than -10 dB across the band from 1.1 GHz-4.8 GHz, while the measured response is only better than -10 dB across the band from 1.1-3.6 GHz.

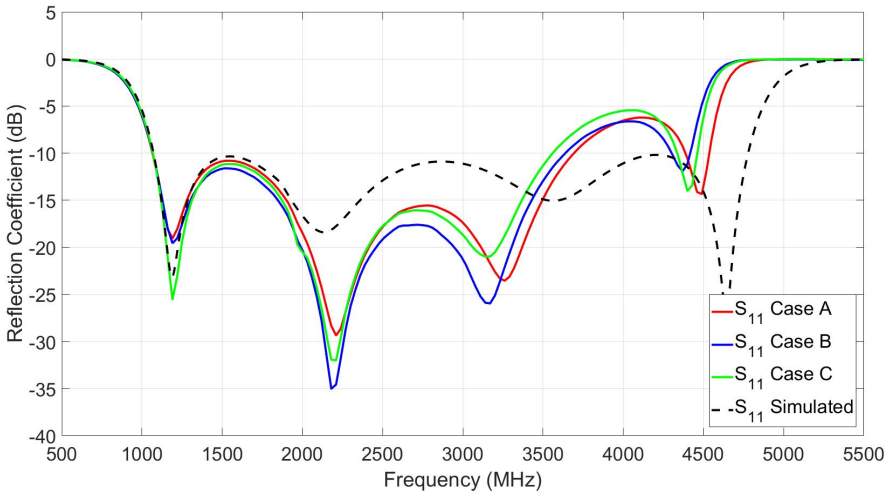

Figure 5.22: Comparison of measured and simulated reflection coefficient results for the rectangular coaxial Marchand balun.

The structure of the actual baluns are analyzed and compared to the simulated balun to determine the cause behind the conflicting results. The full-wave reconstructed model of the manufactured balun is shown in Fig. 5.23, highlighting the differences from the simulated model in Fig. 5.18.

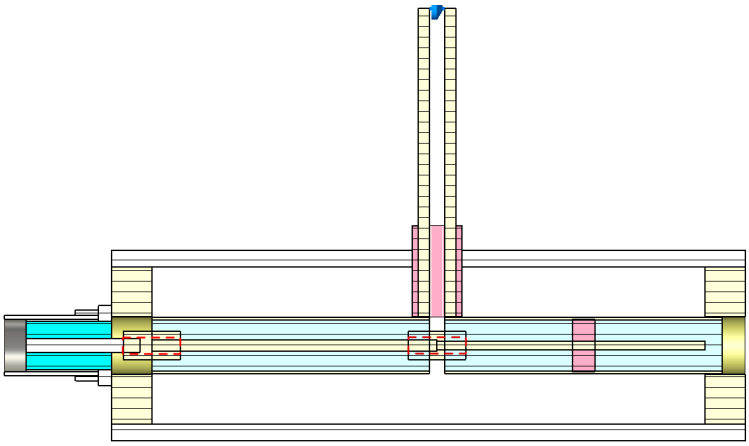

Figure 5.23: Simulated model of manufactured balun.

A miscommunication during the manufacturing process resulted in the actual diameter of the mechanical sleeves being d=2.5 mm instead of the expected 2 mm. The increased sleeve diameter results in a change in the input impedance of the coaxial line sections Z_1 and Z_b. The problem is further exacerbated at higher frequencies due to the l=5 mm sleeve length which is electrically long at high frequencies. This can be seen quite clearly in the measured S_{11} results in Fig. 5.22.

The other issue relates to the Teflon supporting the balanced lines Z_4. The opening was supposed to be filled with Teflon material with the balanced lines passing through. Instead, the Teflon support simply surrounded the twin lead lines extending from the balun junction. A comparison of the actual measured results and the full-wave reconstructed model results are shown in Fig. 5.24. The simulated results now provide a much better indication of the measured balun performance and explains the reason behind the poor measurement results.

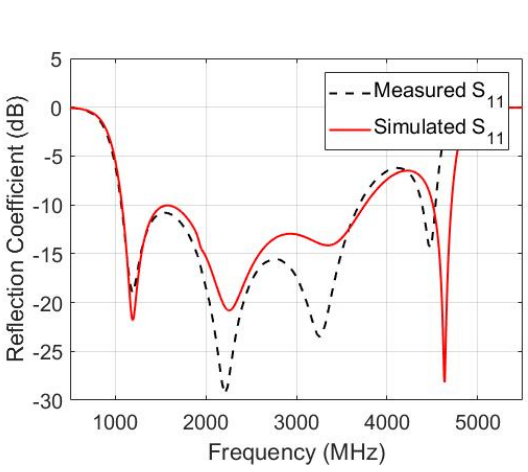

(a)

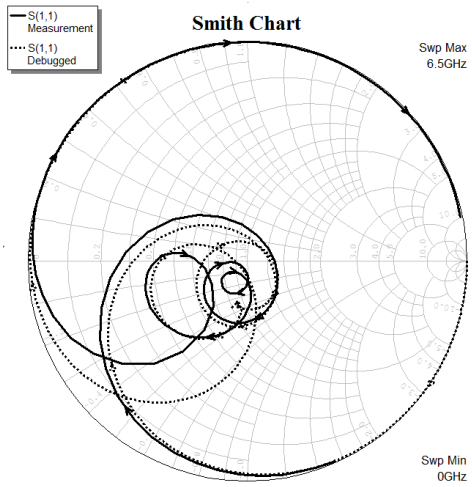

(b)

Figure 5.24: Comparison of simulated and measured reflection coefficient results for adjusted model dimensions.

The rectangular coaxial Marchand baluns shown in Fig. 5.21 are then disassembled and reconstructed in back-to-back configuration, so that the through insertion loss (S_{21}) can be measured. A comparison between the simulated and measured insertion loss results is shown in Fig. 5.25. The simulated and measured through insertion loss results correspond well with one another, with slight differences being attributed to manufacturing error.

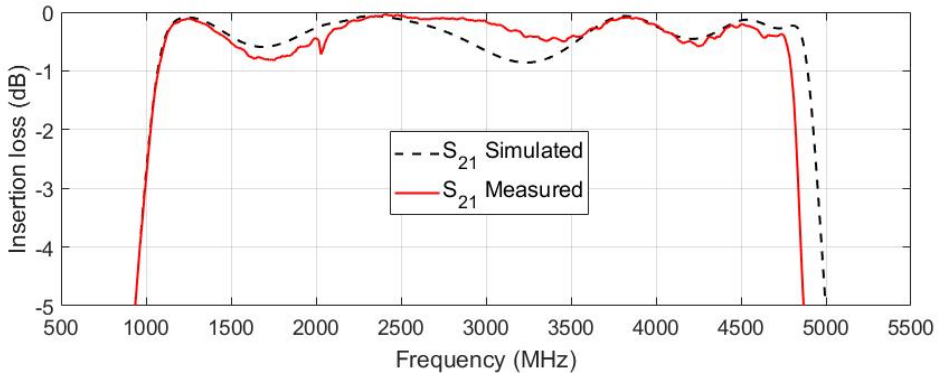

Figure 5.25: Comparison of measured and simulated insertion loss results for the rectangular coaxial Marchand balun.

The next step is to redesign some aspects of the balun structure of Fig. 5.23 to improve the the poor reflection coefficient and balance performance.

5.3.2 Design II

Design I of the rectangular coaxial Marchand balun displayed decent return and insertion loss performance, but did not meet the necessary requirements for integration with the sinuous antenna due to its poor amplitude and phase balance performance. This was because return loss performance was prioritised at the expense of balance performance. Design II of the rectangular coaxial Marchand balun is proposed to better meet the necessary requirements for integration with the sinuous antenna. The new design, shown in Fig. 5.26, is again based on the rectangular Marchand balun shown in Fig. 5.15. Refer to Appendix C.2 for the table of relevant design parameters.

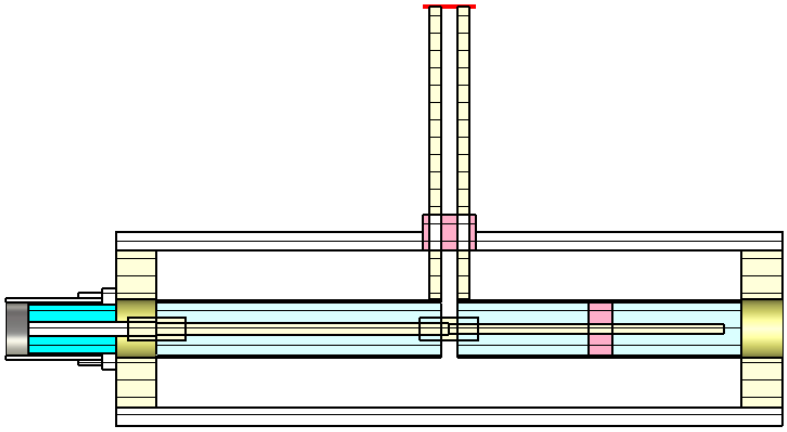

Figure 5.26: Sectioned side-view structure of Design II.

The optimizer function in CST MWS was used to tune certain parameters of the balun to compensate for the same mechanical shortcomings as described in Design I. The optimized parameters are shown in comparison to the standard rectangular coaxial balun in Table 5.4. Note that impedances Z_1 and Z_4 are not made tunable parameters, as this would require new combinations of brass tubes and rods for manufacturing.

Table 5.4: Comparison between design parameters of the standard design and Design II.

Parameter	**Description**	**Standard Design**	**Design II**
Z_{ab}	Cavity impedance	137 Ω	127.61 Ω
Z_4	Balanced-line impedance	165 Ω	185 Ω
L_4	Balanced-line length	25 mm	25.05 mm
r_o	Top Teflon support radius	2.5 mm	2.26 mm

The return and insertion loss results are presented in Fig. 5.27a and 5.27b respectively. The return loss is better than -10 dB across the band from 1.1 GHz to 4.8 GHz, but the ideal equi-ripple response is mostly lost. The back-to-back insertion loss is better than -0.91 dB across the same band as the return loss which is consistent with previous results.

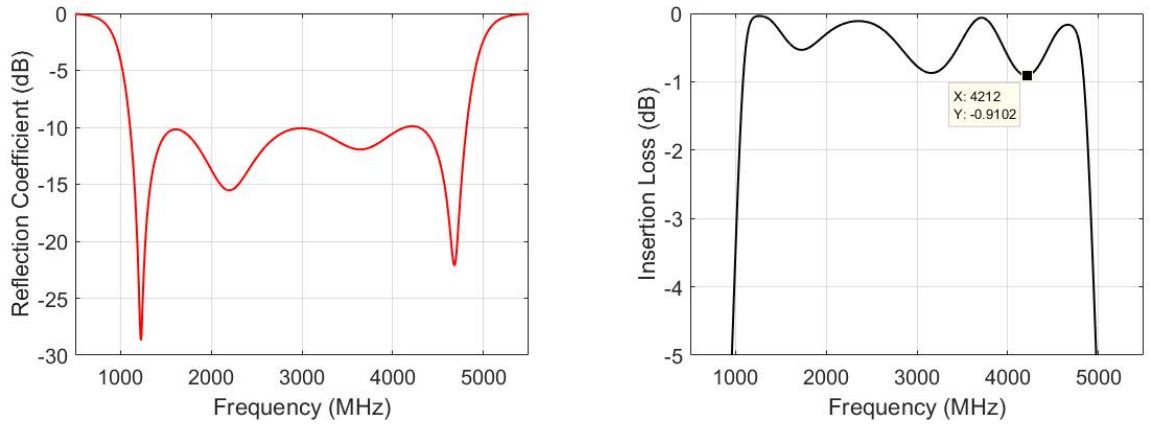

(a) (b)

Figure 5.27: Simulated performance of Design II (a) Reflection coefficient (b) Back-to-back insertion loss.

In contrast to Design I, the respective lengths of Z_1, Z_b and Z_{ab} are left unchanged in order to preserve the symmetry of the balun around the balun junction. The amplitude and phase balance of Design II are therefore expected to be better than Design I. This is confirmed by the simulation results shown in Fig. 5.28a and 5.28b respectively. The amplitude balance is better than ± 0.2 dB across the desired 1-5 GHz band, which displays marked improvement against Design I. Similarly, the phase balance of Design II is better than 1.5° across the same band.

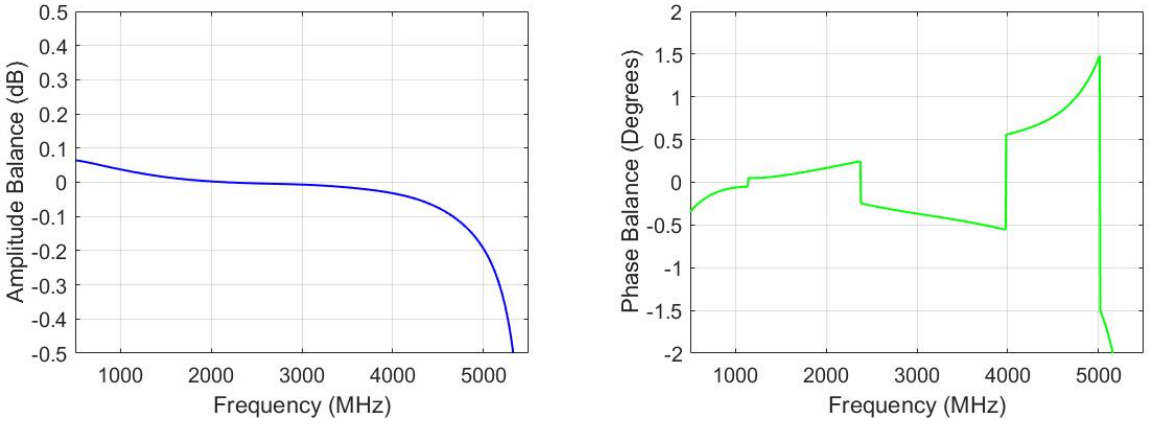

(a) (b)

Figure 5.28: Simulated performance of Design II (a) Amplitude balance (b) Phase balance.

Design II, with its various mechanical improvements, performs exceptionally well when compared to Design I and the standard rectangular Marchand balun in Section 4.3.3. The return and insertion loss results of Design II are similar to that of Design I, but the amplitude and phase balance are significantly better. Design II of the rectangular coaxial Marchand balun is therefore selected for integration with the sinuous antenna.

5.4 Summary

A fourth order Marchand balun was designed to enable best possible reflection coefficient performance. The simulated reflection coefficient was better than -10 dB across the band from 1.1-4.8 GHz, with an insertion loss better than 0.85 dB. The amplitude balance result was better than ± 0.4 dB across the band, and the phase balance was within 9.8°. The balun was fabricated and tested, and the measured reflection coefficient results were compared to the simulated results. A second fourth order balun was also designed to improve the balance performance of the first design. The simulated reflection coefficient was also better than -10 dB across the band, but displayed a significant improvement in balance performance, achieving an amplitude balance of ± 0.2 dB and a phase balance of 1.5°.

Chapter 6

Integration

This chapter presents the basic integration of the planar and coaxial Marchand baluns with the pyramidal sinuous antenna. The integration step serves as proof of concept for the proposed feeding methods while further verifying the effectiveness of the designed baluns. A two-arm pyramidal sinuous antenna, capable of single linear-polarization, is selected for integration. The single antenna arm-pair is sufficient for classifying the effectiveness of the balun in question, and the layout of the feeding region of this antenna makes it easy to integrate with the balun. The return loss and radiation characteristics of the balun and antenna are used as performance specifications for the system.

6.1 Planar Marchand Balun Integration

6.1.1 Geometry

A single linearly polarized pyramidal sinuous antenna, with design parameters listed in Table 6.1, is generated in CST MWS and attached to the balanced output lines of the planar Marchand balun via parallel circular conductors. The balanced output lines of the balun are slightly adjusted to align with the feeding points of the antenna.

Table 6.1: Design parameters of the pyramidal sinuous antenna for planar integration.

Design Parameter	**Value**
Angular width (α)	24.85°
Rotation angle (δ)	14.95°
Growth rate (τ)	0.842
Height (h)	5 mm
Offset angle (θ)	56.48°
f_{min}	2 GHz
f_{max}	6 GHz

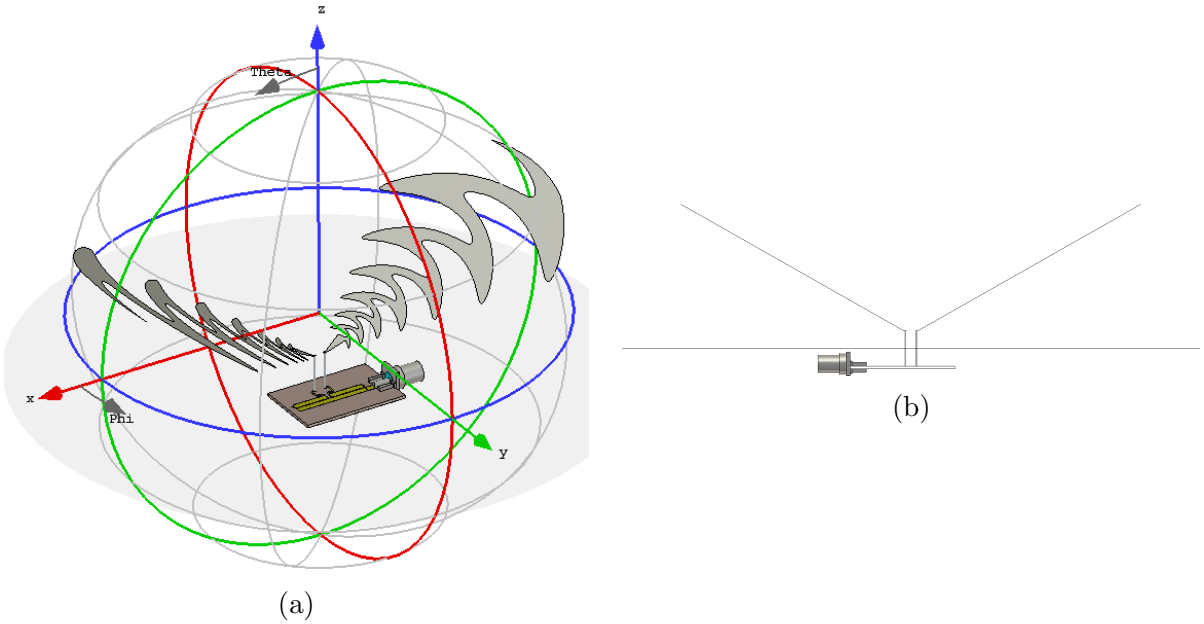

(a) (b)

Figure 6.1: The integrated balun and antenna system. (a) Isometric view (b) Side-view.

The impedance of the d=0.5 mm parallel circular conductors for a separation of D=2.7 mm, is approximately 305 Ω which matches the input impedance of the antenna. The parallel lines are 10 mm in length - which is the shortest that they can be made to accommodate the balun beneath the ground plane.

6.1.2 Simulated Results

The normalized farfield E-field as a function of the elevation angle, θ, is given in Fig. 6.2. The fields for the principle azimuth cuts $\phi = 0°$ and 180° at 2, 4 and 6 GHz are given in Fig. 6.2a. Reasonably symmetric, unidirectional radiation fields are obtained at 4 GHz and 6 GHz. The radiation field at 2 GHz is slightly asymmetric, which is inconsistent with the other presented fields. The asymmetry is caused by the non-ideal phase balance of the planar balun feeding the antenna. The fields for the principle azimuth cuts $\phi = 90°$ and 270° at 2, 4 and 6 GHz is given in Fig. 6.2b. The fields are shown to be symmetric and uni-directional.

The simulated antenna gain with respect to frequency is shown in Fig. 6.3. It shows the maximum gain at broadside for an ideally excited antenna, and the balun and antenna system. Unlike the gain of the dual polarized antenna in Chapter 3.4.2, the gain of the single linearly polarized antenna will not be influenced by the effects of cross polarization. The gain of the integrated system follows a similar trend to the ideal antenna gain, however, the trend deteriorates between 5-6 GHz. The gain of the integrated system is shown to fluctuate around the 9.5 dB mark, with a maximum value of 11 dB at 2 GHz, and a minimum value of 8 dB at 5.9 GHz. The dip at 5.9 GHz is due to the degraded balance of the planar Marchand balun at 5 GHz and higher.

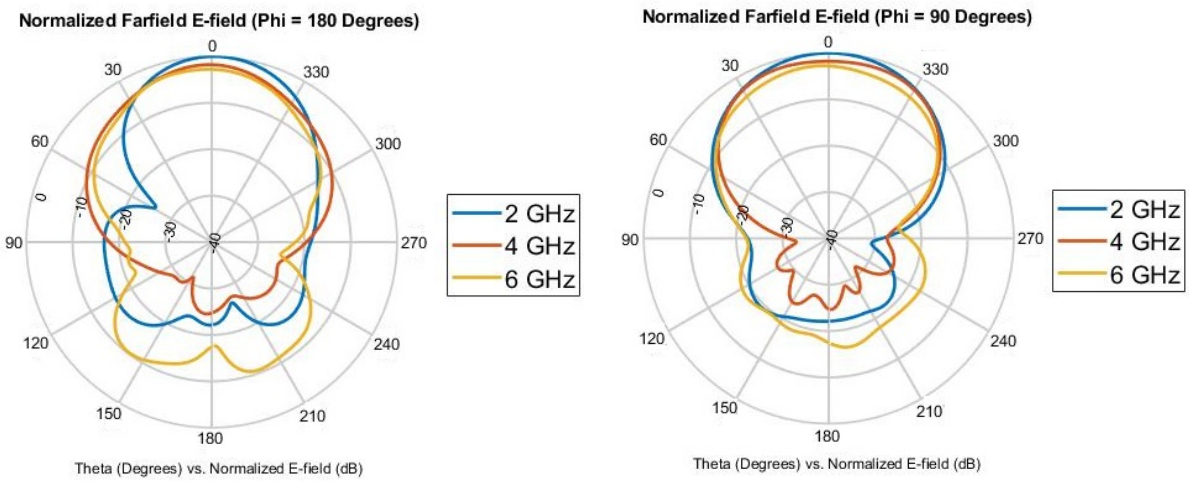

(a) (b)

Figure 6.2: Radiation characteristics of planar integration (a) Normalized magnitude of farfield E-field for ϕ=180° (b) Normalized magnitude of farfield E-field for ϕ=90°.

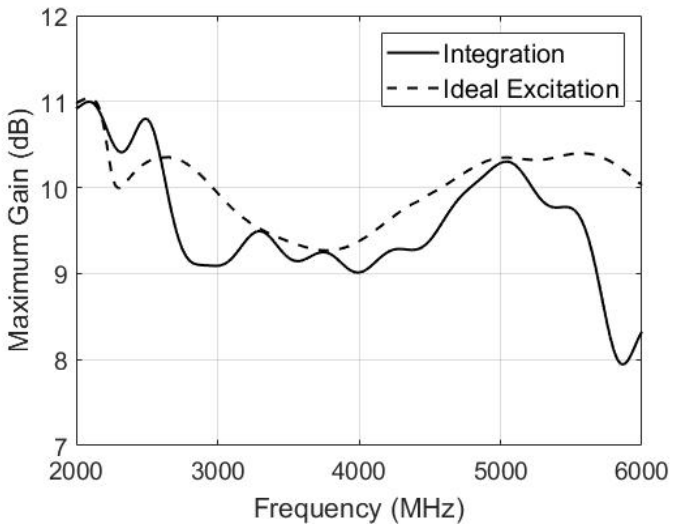

Figure 6.3: Maximum simulated gain at broadside for planar integration.

The simulated reflection coefficient for the balun and antenna system is shown in Fig. 6.4. The result is positive given that it is generally better than -12 dB across most of the band from 2 - 6 GHz.

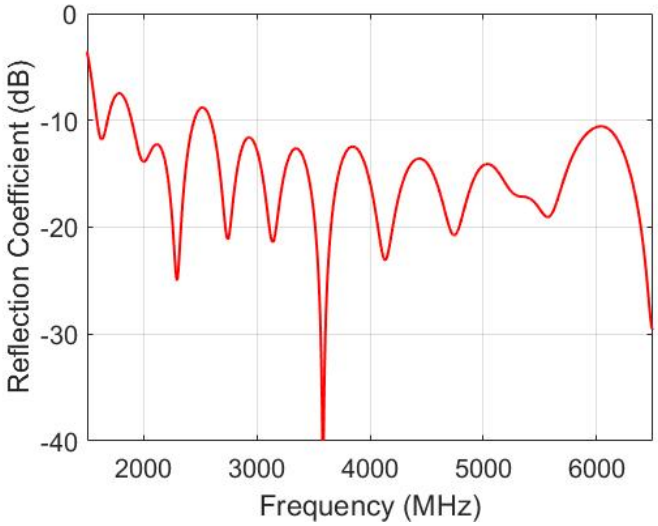

Figure 6.4: Reflection coefficient of planar balun and antenna system.

6.2 Coaxial Marchand Balun Integration

6.2.1 Geometry

A pyramidal sinuous antenna with the design parameters listed in Table 6.2 is generated in CST MWS and attached to the balanced line end of the rectangular coaxial Marchand balun as seen in Fig. 6.5.

Table 6.2: Design parameters of the pyramidal sinuous antenna for coaxial integration.

Design Parameter	**Value**
Angular width (α)	24.85°
Rotation angle (δ)	14.95°
Growth rate (τ)	0.842
Height (h)	5 mm
Offset angle (θ)	56.48°
f_{min}	1 GHz
f_{max}	5 GHz

The position of the reflecting plane of the antenna is expected to influence the functionality of the balun. This is because of the unpredictable effect of the antenna and ground plane on the impedance of Z_4. The effect will be investigated in Section 6.2.3.

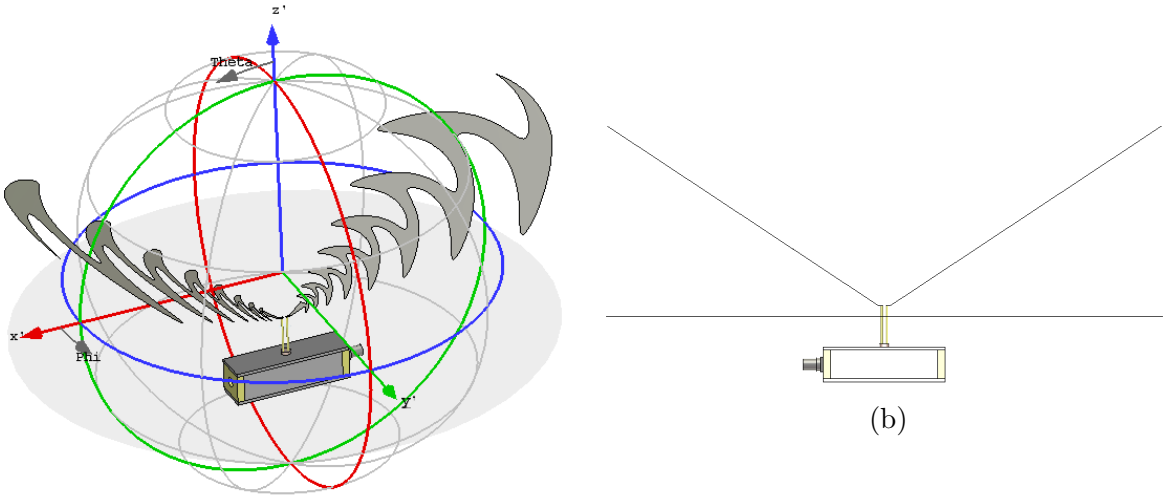

(a) (b)

Figure 6.5: The integrated balun and antenna system. (a) Isometric view (b) Side-view.

6.2.2 Simulated Results

The normalized farfield E-field as a function of the elevation angle, θ, is given in Fig. 6.6. The fields for the principle azimuth cuts $\phi = 0°$ and $180°$ are given in Fig. 6.6a, and the fields for the principle azimuth cuts $\phi = 90°$ and $270°$ are given in Fig. 6.6b for 2, 4 and 6 GHz. The equal magnitude, symmetric radiation fields show a marked improvement compared to the planar balun and antenna system. This is attributed to the superior amplitude and phase balance of the coaxial balun.

The simulated antenna gain with respect to frequency is analyzed in Fig. 6.7. It shows the maximum gain at broadside for an ideally excited antenna, and a balun and antenna system. The gain is exceptionally consistent with the ideally excited pyramidal sinuous antenna and this is attributed to the balance performance of the coaxial balun. The maximum gain for the integrated case is shown to be consistent around the 10 dB mark up to 4 GHz where it decreases to approximately 8.2 dB at 4.9 GHz. This dip at 4.9 GHz is likely due truncation of the surface currents, similar to Chapter 3.4.2. The maximum total gain is constant within 2 dB for the entire band.

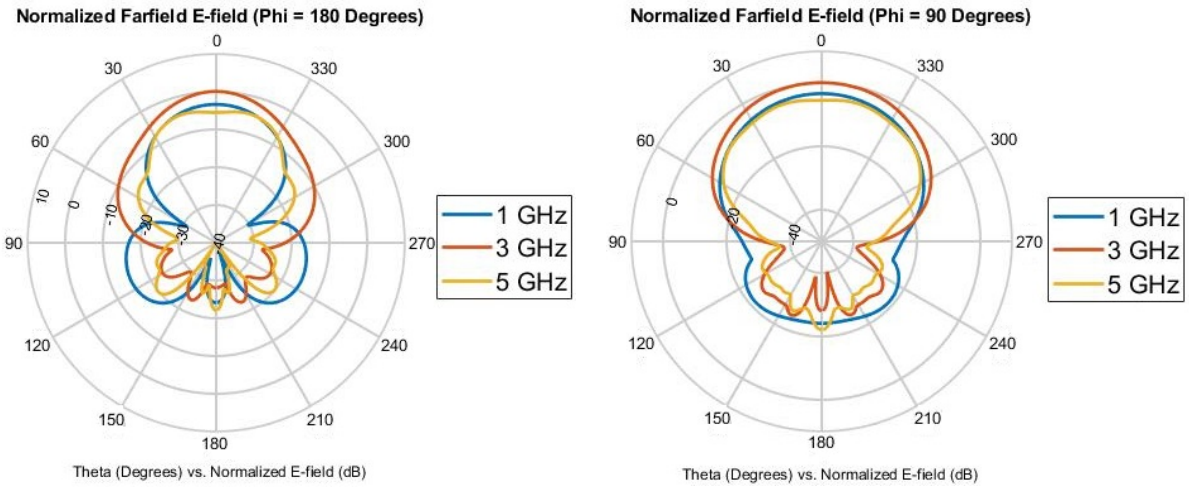

(a) (b)

Figure 6.6: Radiation characteristics of coaxial integration (a) Normalized farfield E-field for $\phi = 180°$ (b) Normalized farfield E-field for $\phi = 90°$.

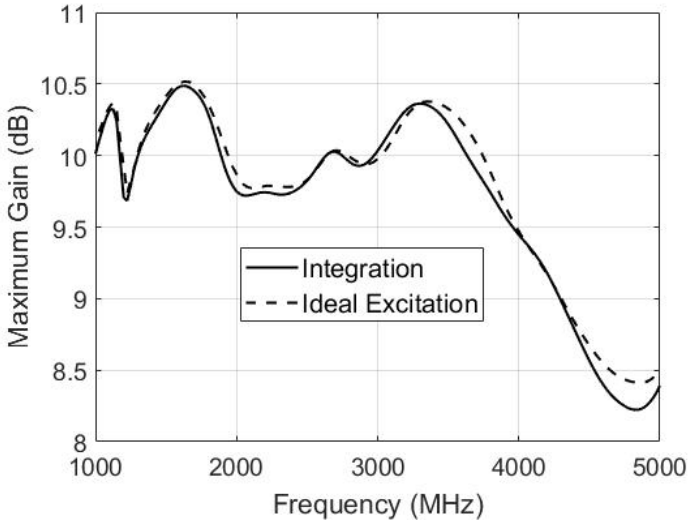

Figure 6.7: Maximum simulated gain at broadside for coaxial integration.

The simulated reflection coefficient for the balun and antenna system is shown in Fig. 6.8. It is generally better than -10 dB across most of the band from 1.1-4.8 GHz. However, the reflection coefficient at some locations reaches a maximum of -7.4 dB, which is not ideal. The suspected cause is related to the input impedance change from the added presence of the reflecting plane.

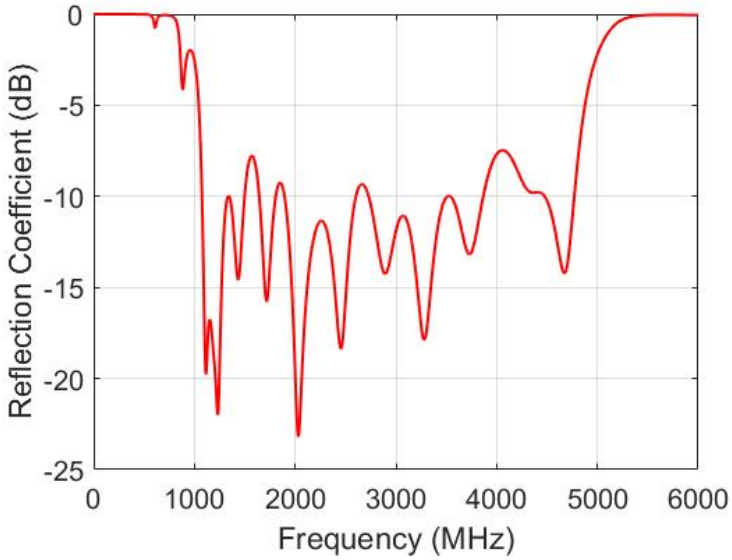

Figure 6.8: Reflection coefficient of coaxial balun and antenna system.

6.2.3 Effect of the Reflecting Plane

The addition of the reflecting plane between the antenna and balun is investigated in this section. Presence of the reflecting plane beneath the antenna destroys the self-complementarity of the antenna and causes impedance variation over frequency. However, it is necessary to determine the effect of the reflecting plane on the balanced balun output, as well as the integrated system as a whole. This is enabled by dividing the integration step into parts; new sections are added to the rectangular Marchand balun in a step-by-step manner and the input impedance is studied.

Case A is the first configuration and represents the rectangular Marchand balun with an equivalent 300 Ω load. The second configuration, Case B, includes the reflecting plane placed at a distance h from the balanced line ends with an equivalent 300 Ω load. Finally, the third configuration, Case C, is depicted in Fig. 6.5 where the 300 Ω load is replaced by the actual sinuous antenna.

A comparison between the input impedance for Case A and B is shown in Fig. 6.9. The magnitudes of the input impedance for Case A and B are shown in Fig. 6.9a. The input impedances follow a similar trend with notable difference between 3-4.5 GHz. The complex representation of the input impedance is shown in Fig. 6.9b, where the input impedance is analyzed for a 2-4.5 GHz sweep. Again, notable differences are also observed between the real and imaginary part for increasing frequencies. These differences correspond closely to the decreased reflection coefficient between 2.9-3.8 GHz, and the increased reflection coefficient between 3.8-4.5 GHz as shown in Fig. 6.9c.

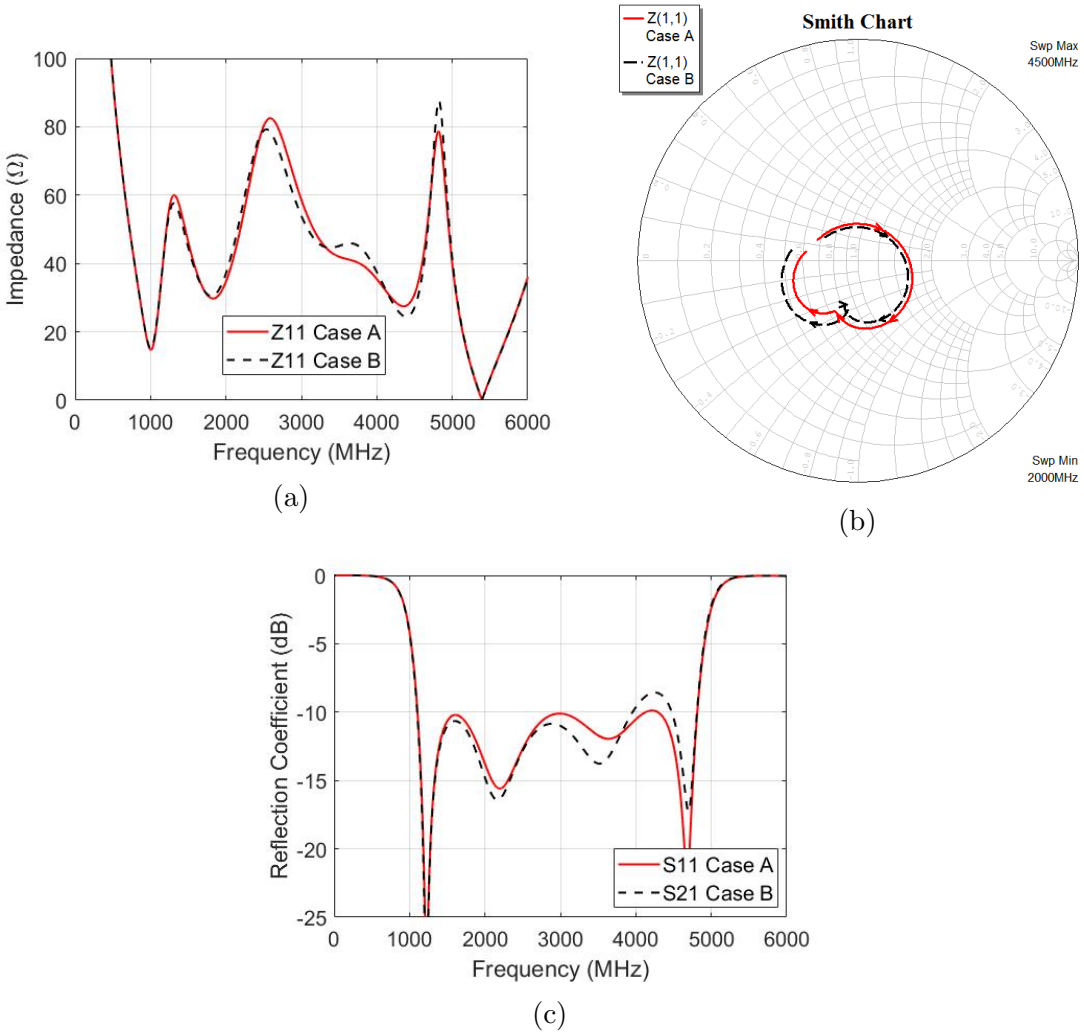

Figure 6.9: Comparison of Case A and Case B input impedance.

A comparison between the input impedance of Case A and C is shown in Fig. 6.10. The magnitudes of the input impedance for Case A and C are shown in Fig. 6.10a. Again, the input impedances follow a similar trend with the exception that the impedance for Case C shows multiple additional resonances. These resonances relate to the impedance variation of the antenna over frequency. The resonances also appear in the complex representation of the input impedance as shown in Fig. 6.10b for a 1-4.5 GHz sweep. The resonances are mostly centred around the middle of the Smith chart which coincides with the reflection coefficient across most of the band. The Smith chart representation of the input impedances also shows clearly where the differences between the real and imaginary parts of the input impedances for Case A and C are the biggest. This corresponds to the differences in the reflection coefficient results shown in Fig. 6.10c.

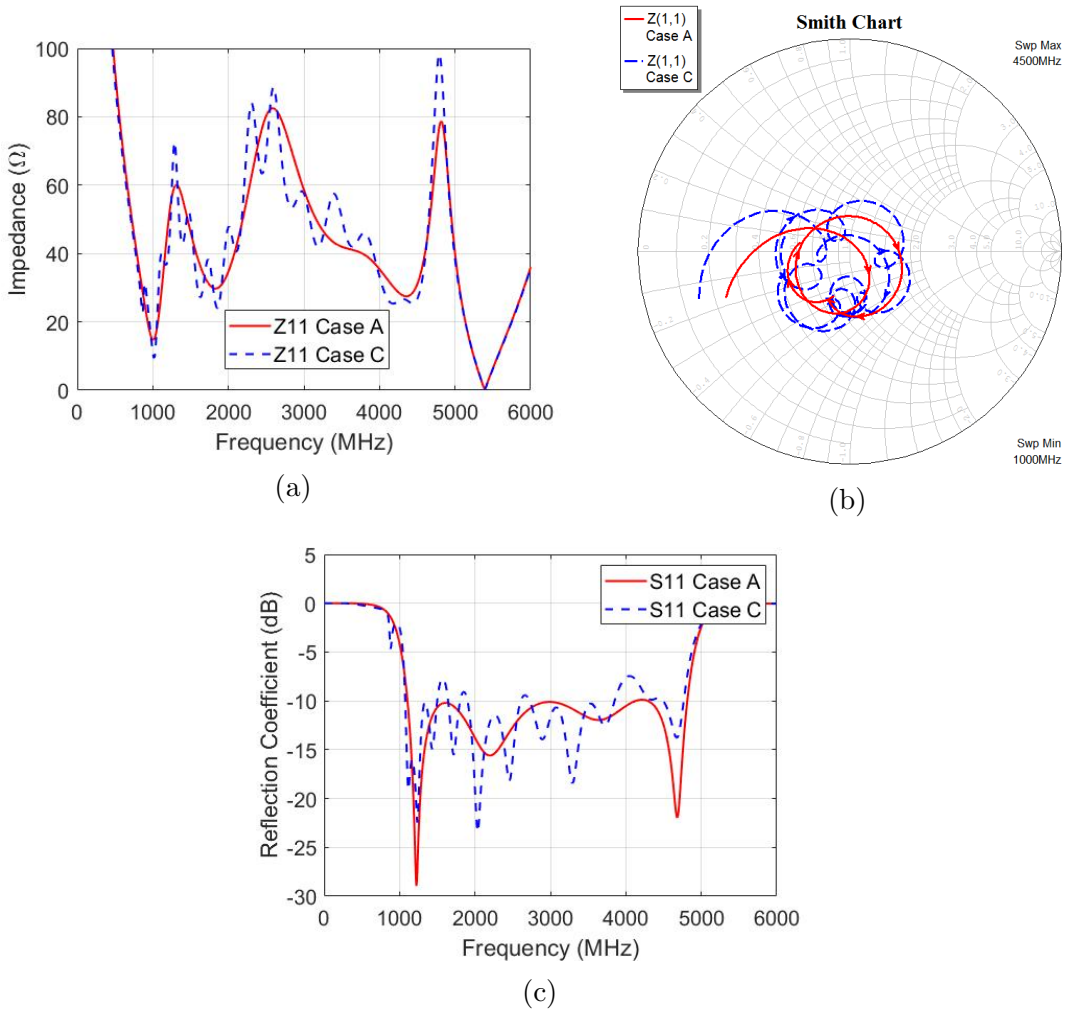

Figure 6.10: Comparison of Case A and Case C input impedance.

The study confirms that the presence of the reflecting plane between the antenna and balun has a non-negligible effect on the input impedance of the the system. Tuning or modifying some aspects of the balun, like the impedance and length of the balanced line outputs, to compensate for the change in impedance may provide better reflection coefficient results.

Practical verification and measurements of the balun and antenna system was considered, but early experiments in a simulated environment inferred that significant effort would be required to prepare the pyramidal sinuous antenna, single and dual polarization, for manufacturing. Specifically, the feeding region of the antenna used in simulation is not practically feasible and has to be revisited. Therefore, the practical integration of the balun and antenna is left for future work.

6.3 Summary

The performance and design procedure of the planar and rectangular Marchand baluns are further verified in this chapter via integration with a two-arm pyramidal sinuous antenna. The radiation patterns, gain and reflection coefficients of the integrated systems are simulated and the results are presented. Both balun and antenna systems returned acceptable results, confirming the suitability of the designed baluns.

The planar Marchand balun and antenna system returned reasonably symmetric, unidirectional radiation patterns given the poor balance of the balun. The simulated gain for the system is better than 9.5 dB on average across the entire 2-6 GHz band, and the reflection coefficient is better than -12 dB across the same band.

The rectangular coaxial Marchand balun and antenna system displayed improved symmetric, uni-directional radiation fields with its improved balance performance. The simulated gain for the system is better than 9.6 dB across the band from 1-4 GHz, after which it decreases slightly. The reflection coefficient is approximately -10 dB across the same band with some exceptions.

Chapter 7

Conclusion

7.1 Summary

This thesis presented the analysis, design and fabrication of Marchand baluns for the pyramidal sinuous antenna. A planar low-profile Marchand balun, manufactured using standard PCB printing techniques, was designed for use with a 2-6 GHz antenna. A fourth order rectangular coaxial Marchand balun was also designed in order to extend the operating frequency range of the antenna across 1-5 GHz.

A microstrip coupled-line Marchand balun with a modified ground plane was considered for the purpose of bandwidth enhancement. To that end, the influence of ground plane apertures in microstrip coupled-line structures was investigated. Ground plane apertures beneath coupled lines result in tight coupling and consequently wide bandwidth. This was verified through simulation. A detailed description of the full-wave simulation design procedure for the balun was provided which can be used to design a balun with an arbitrary impedance transformation. Special attention was given to the configuration of the modified balun to ensure simple and open-ended integration with the sinuous antenna. Prototype test devices of the planar balun were manufactured and compared to simulated results and good correlation was achieved. Further tweaking and optimization of the prototype baluns to produce a measured return loss of better than 10 dB is suggested.

A fourth order rectangular Marchand balun was considered in order to further extend the potential bandwidth of the system. Closed-form impedance design expressions resulting in a Chebyshev passband response were provided for the design of second, third and fourth order Marchand baluns. The existence of higher order modes in the coaxial cavity was discovered and a study to counteract them was also conducted. A prototype of the designed balun was manufactured and tested, and the reflection coefficient results were compared. The balun performed reasonably well and the differences between the simulated and measured results were attributed to manufacturing error. However, this iteration of the balun gave unacceptable balance results. A second design of the balun was introduced to better meet the requirements for integration with the sinuous antenna. The updated design achieved an amplitude and phase balance better than ± 0.2 dB and

1.5° respectively, while meeting the required specifications for the return and insertion loss. Sourcing components for the inner coaxial lines of the coaxial balun is an arduous process, as the necessary rods and tube diameters are small and the available combinations of rods/tubes provide the desired impedances are limited. Therefore, the dimensions of the resulting balun are determined by the available rod/tube dimensions that make up the inner coaxial lines.

Finally, the designed planar and coaxial baluns were simulated alongside the pyramidal sinuous antenna. The basic integration procedure and the accompanying challenges were discussed. In particular, the integration of the coaxial balun and antenna can be revisited in order to try minimize the effects of the reflecting plane on balun performance. Overall, the simulated return loss and radiation characteristics of both balun and antenna systems lends credibility to the design of the baluns and their use with the pyramidal sinuous antenna.

7.2 Recommendations for Future Work

Future projects related to the work of this project may include:

- The optimization of the feeding region, or implementation of an existing feeding region solution, for the pyramidal sinuous antenna as explained in Chapter 2.3.4. This would simplify the integration procedure of the dual polarized antenna and the Marchand baluns required for each polarization.
- Practical implementation of the balun and antenna system for single and dual-polarized systems.
- Optimization of the planar Marchand balun with modified ground structures with the aim of improving the phase balance of the balun.
- The design and co-optimization of an integrated fourth order coaxial Marchand balun and impedance transforming network with the purpose of extending the bandwidth of the system to 10:1. The path length of the solution should be kept as short as possible to reduce system noise temperature.

Bibliography

[1] A. R. Taylor, "The Square Kilometre Array," *Proceedings of the International Astronomical Union*, vol. 8, no. S291, p. 337–341, 2012.

[2] P. E. Dewdney, W. Turner, R. Millenaar, R. McCool, J. Lazio, and T. J. Cornwell, "SKA-1 system baseline design," mar 2013. [Online]. Available: https://www.skatelescope.org/

[3] G. Engargiola, "Non-planar log-periodic antenna feed for integration with a cryogenic microwave amplifier," in *IEEE Antennas and Propagation Society International Symposium (IEEE Cat. No.02CH37313)*, vol. 4, 2002, pp. 140–143 vol.4.

[4] J. Yang, M. Pantaleev, P. S. Kildal, B. Klein, Y. Karandikar, L. Helldner, N. Wadefalk, and C. Beaudoin, "Cryogenic 2-13 GHz eleven feed for reflector antennas in future wideband radio telescopes," *IEEE Transactions on Antennas and Propagation*, vol. 59, no. 6, pp. 1918–1934, June 2011.

[5] R. Gawande and R. Bradley, "Towards an ultra wideband low noise active sinuous feed for next generation radio telescopes," *IEEE Transactions on Antennas and Propagation*, vol. 59, no. 6, pp. 1945–1953, June 2011.

[6] G. Cortes-Medellin, "Novel non planar ultra wide band quasi self-complementary antenna," in *2007 IEEE Antennas and Propagation Society International Symposium*, June 2007, pp. 5733–5736.

[7] D. I. L. de Villiers, "Initial study of a pyramidal sinuous antenna as a feed for the SKA reflector system in band-1," in *2017 IEEE International Symposium on Antennas and Propagation USNC/URSI National Radio Science Meeting*, July 2017, pp. 555–556.

[8] N. Steenkamp, D. I. L. de Villiers, and N. Mutonkole, "Wideband pyramidal sinuous antenna for reflector antenna applications," in *2017 11th European Conference on Antennas and Propagation (EUCAP)*, March 2017, pp. 2291–2295.

[9] N. Steenkamp, "Design of a wideband sinuous antenna for radio telescope applications," Master's thesis, Stellenbosch University, 2017.

[10] D. de Villiers, personal communication, 11 2018.

[11] C. Balanis, *Antenna Theory: Analysis and Design*, ser. A Wiley-interscience publication. Harper & Row, 1982.

[12] H. Raza, J. Yang, and M. Pantaleev, "Integration of ultra-wideband planar baluns into the eleven feed," *IET Microwaves, Antennas Propagation*, vol. 8, no. 1, pp. 22–28, January 2014.

[13] G. Engargiola, "Tapered microstrip balun for integrating a low noise amplifier with a nonplanar log periodic antenna," *Review of Scientific Instruments*, vol. 74, no. 12, pp. 5197–5200, 2003. [Online]. Available: https://doi.org/10.1063/1.1622975

[14] P. Gonnet, A. Sharaiha, C. Terret, and A. Skrivervik, "Feeding networks for sinuous antennas," *Microwave and Optical Technology Letters*, vol. 20, no. 3, pp. 195–200, 1999. [Online]. Available: https://onlinelibrary.wiley.com/doi/abs/10.1002

[15] A. Jafargholi and M. Kamyab, "A new approach for feeding sinuous antenna," *AEU - International Journal of Electronics and Communications*, vol. 65, no. 4, pp. 312 – 319, 2011. [Online]. Available: http://www.sciencedirect.com/science/article/pii/S1434841110001032

[16] K. M. P. Aghdam, R. Faraji-Dana, and J. Rashed-Mohassel, "The sinuous antenna-a dual polarized feed for reflector-based searching systems," *AEU - International Journal of Electronics and Communications*, vol. 59, no. 7, pp. 392 – 400, 2005. [Online]. Available: http://www.sciencedirect.com/science/article/pii/S1434841104000639

[17] D. Pozar, *Microwave Engineering, 4th Edition*. Wiley, 2011.

[18] A. M. Pavio and A. Kikel, "A monolithic or hybrid broadband compensated balun," in *IEEE International Digest on Microwave Symposium*, May 1990, pp. 483–486 vol.1.

[19] K. S. Ang and I. D. Robertson, "Analysis and design of impedance-transforming planar Marchand baluns," *IEEE Transactions on Microwave Theory and Techniques*, vol. 49, no. 2, pp. 402–406, Feb 2001.

[20] R. Mongia, I. Bahl, P. Bhartia, and S. Hong, *RF and Microwave Coupled-line Circuits*, ser. Artech House microwave library. Artech House, Norwood, United States, 2007. [Online]. Available: https://books.google.co.za/books?id=XN5kQgAACAAJ

[21] D. E. Baker and J. B. du Toit, "A compact 1 to 18 GHz planar spiral antenna for interferometer and other direction finding applications," in *2012 IEEE-APS Topical Conference on Antennas and Propagation in Wireless Communications (APWC)*, Sept 2012, pp. 1016–1019.

[22] M. C. Tsai, "A new compact wideband balun," in *IEEE 1993 Microwave and Millimeter-Wave Monolithic Circuits Symposium Digest of Papers*, Atlanta, United States, June 1993, pp. 123–125.

[23] Z.-Y. Zhang, Y.-X. Guo, L. C. Ong, and M. Y. W. Chia, "A new planar Marchand balun," in *IEEE MTT-S International Microwave Symposium Digest, 2005.*, Long Beach, United States, June 2005, pp. 1207–1210.

[24] C. Tseng and Y. Hsiao, "A new broadband marchand balun using slot-coupled microstrip lines," *IEEE Microwave and Wireless Components Letters*, vol. 20, no. 3, pp. 157–159, March 2010.

[25] H. R. Phelan, "A wide-band parallel-connected balun," *IEEE Transactions on Microwave Theory and Techniques*, vol. 18, no. 5, pp. 259–263, May 1970.

[26] R. H. DuHamel, "Dual polarized sinuous antennas," apr 1987, US Patent 4,658,262.

[27] R. DuHamel and D. Isbell, "Broadband logarithmically periodic antenna structures," in *1958 IRE International Convention Record*, vol. 5, New York, United States, June 1957, pp. 119–128.

[28] R. DuHamel and F. Ore, "Logarithmically periodic antenna designs," in *1958 IRE International Convention Record*, vol. 6, New York, United States, June 1958, pp. 139–151.

[29] R. DuHamel and D. Berry, "A new concept in high frequency antenna design," in *1958 IRE International Convention Record*, vol. 7, New York, United States, June 1959, pp. 42–50.

[30] J. Volakis, *Antenna Engineering Handbook*. McGraw-Hill Education, New York, United States, 2018. [Online]. Available: https://books.google.co.za/books?id=2ytcswEACAAJ

[31] V. Rumsey, *Frequency Independent Antennas*. Academic Press, Cambridge, United States, 1966. [Online]. Available: http://www.sciencedirect.com/science/article/pii/B9781483229690500097

[32] Y. Mushiake, "Self-complementary antennas," *IEEE Antennas and Propagation Magazine*, vol. 34, no. 6, pp. 23–29, Dec 1992.

[33] N. Mutonkole, "Study of a wideband sinuous feed for reflector antenna applications applications," Master's thesis, Stellenbosch University, 2013.

[34] J. H. Cloete and T. Sickel, "The planar dual-polarized cavity backed sinuous antenna - a design summary," in *2012 IEEE-APS Topical Conference on Antennas and Propagation in Wireless Communications (APWC)*, Cape Town, South Africa, Sept 2012, pp. 1169–1172.

[35] G. Deschamps, "Impedance properties of complementary multiterminal planar structures," *IRE Transactions on Antennas and Propagation*, vol. 7, no. 5, pp. 371–378, December 1959.

[36] N. Mutonkole and D. I. L. de Villiers, "A 3:1 bandwidth planar, lossless cavity backed sinuous antenna for reflector feed applications," in *2013 AFRICON*, Pointe-Aux-Piments, Mauritius, Sept 2013, pp. 1–5.

[37] HyperWorks FEKO 14.0. [Online]. Available: https://altairhyperworks.com/product/FEKO

[38] CST Microwave Studio. [Online]. Available: https://www.cst.com/products/cstmws

[39] C. C. S. Technology, "Frequency domain solver," jun 2017. [Online]. Available: https://www.cst.com/products/cstmws/solvers/frequencydomainsolver/

[40] ——, "Transient solver," jun 2017. [Online]. Available: https://www.cst.com/products/cstmws/solvers/transientsolver/

[41] M. C. Horton and R. J. Wenzel, "General theory and design of optimum quarter-wave tem filters," *IEEE Transactions on Microwave Theory and Techniques*, vol. 13, no. 3, pp. 316–327, May 1965.

[42] AWR Microwave Office. [Online]. Available: https://www.awrcorp.com/products/ni-awr-design-environment/microwave-office-software

[43] M. C. Velazquez-Ahumada, J. Martel, and F. Medina, "Parallel coupled microstrip filters with floating ground-plane conductor for spurious-band suppression," *IEEE Transactions on Microwave Theory and Techniques*, vol. 53, no. 5, pp. 1823–1828, May 2005.

[44] K. H. Yusof, N. Seman, and M. H. Jamaluddin, "Design and analysis of wideband 3 and 6 db coupled-line coupler with different grounding techniques," in *2013 IEEE International RF and Microwave Conference (RFM)*, Penang, Malaysia, Dec 2013, pp. 34–38.

[45] J. H. Cloete, "Exact design of the Marchand balun," in *1979 9th European Microwave Conference*, Brighton, United Kingdom, Sept 1979, pp. 480–484.

[46] V. Trifunovic and B. Jokanovic, "Review of printed Marchand and Double Y baluns: characteristics and application," *IEEE Transactions on Microwave Theory and Techniques*, vol. 42, no. 8, pp. 1454–1462, Aug 1994.

[47] D. Bachrathy and G. Stépán, "Bisection method in higher dimensions and the efficiency number," *Periodica Polytechnica Mechanical Engineering*, vol. 56, no. 2, pp. 81–86, 2012.

[48] W. L. Barrow and W. W. Mieher, "Natural oscillations of electrical cavity resonators," *Proceedings of the IRE*, vol. 28, no. 4, pp. 184–191, April 1940.

[49] Y. A. Omar and C. F. Miller, "Characteristic impedance of rectangular coaxial transmission lines," *Transactions of the American Institute of Electrical Engineers, Part I: Communication and Electronics*, vol. 71, no. 1, pp. 81–89, Jan 1952.

[50] F. Sabath, E. L. Mokole, and S. N. Samaddar, "Definition and classification of ultra-wideband signals and devices," *URSI Radio Science Bulletin*, vol. 2005, no. 313, pp. 12–26, June 2005.

Appendices

Appendix A

Balun Performance Specifications

The performance of a balun can be largely classified by its relevant scattering or S-parameter matrix. The S-parameters expressed here simply describe the ratio of incident to reflected waves at each port of a device after stimulation of a single port.

$$S = \begin{bmatrix} S_{11} & S_{12} & S_{13} \\ S_{21} & S_{22} & S_{23} \\ S_{31} & S_{32} & S_{33} \end{bmatrix} \tag{A.1}$$

The baluns considered in this work are passive microwave devices, meaning that the device is reciprocal and can be used bidirectionally. Its S-parameter matrix will therefore be symmetric ($S_{ij} = S_{ji}$) [17]. Many applicable performance characteristics are derived from these parameters while some are common microwave specifications.

Return and Insertion Loss

A high performance balun is characterized by a high return loss, typically better than 10 dB, and a low insertion loss. This is necessary to ensure sufficient power for cascaded devices. These measures are dependant on S_{11}, S_{21} and S_{31} in the scattering matrix. The balanced ports of a balun may be excited in common-mode or differential mode. If there is no isolation between the balanced ports, if S_{23} is finite, then the return loss for either mode will be different. In the ideal case, the common-mode signal is perfectly reflected, while the differential signal return loss is infinite. Therefore, the return loss of single-ended ports, S_{22} and S_{33}, that make up the balanced ports is somewhat trivial as those ports are combined and excited in a differential manner. Mixed-mode S-parameters can be used to properly characterize this effect, instead of the commonly used single-ended S-parameters.

Amplitude and Phase Balance

The amplitude and phase balance of a balun are a measure of how accurately the signal power and phase are matched between the balanced ports of a balun. Amplitude balance is a measure of the similarity of the output power magnitude between the two balanced ports. It is given by

$$AB = |S_{21}| - |S_{31}|. \tag{A.2}$$

The amplitude balance for an ideal balun is 0 dB. The phase balance is the measure of how closely the inverted output is to 180° out of phase with the non-inverted output specified in degrees which is given by

$$PB = \angle S_{21} - \angle S_{31}. \tag{A.3}$$

The phase balance can also be expressed around 0° which represents perfect anti-phase outputs. These measures are dependant on S_{21} and S_{31} in the scattering matrix. The quality of the balun structure, as well as the lengths of the output lines contribute to the balance.

Bandwidth

Frequency coverage or bandwidth is an important measure for signal and device classification. The proposed interpretation of bandwidth in this work is loosely based on the standard set by the United States Federal Communications Commission (FCC). The FCC definition specifies the bandwidth as the frequency band bounded by the points that are 10 dB below the highest radiation transmission [50]. However, in this work, it makes more sense to specify the bandwidth as the frequency where the reflection coefficient of the device is less than -10 dB. Bandwidth can be defined as fractional or proportional:

$$\text{Fractional Bandwidth}(B_f) = \frac{2(f_{upper} - f_{lower})}{(f_{centre})}, \tag{A.4}$$

$$\text{Proportional Bandwidth}(B) = \frac{f_{upper}}{f_{lower}}. \tag{A.5}$$

The centre frequency is specified by f_{centre} and the upper and lower frequency cutoffs are given by f_{upper} and f_{lower} respectively. The fractional bandwidth, the ratio of a signal's energy bandwidth to its centre frequency, can also be specified as a percentage. Ideal baluns have infinite bandwidths, and the bandwidth of practical baluns is dependant on their application.

Appendix B

Closed-form Impedance Expressions

Second-order Marchand balun

The transmission line equivalent circuit for the second order Marchand balun is shown in Fig. B.1. It consists of a $\lambda/4$ open-circuit stub Z_b and the $\lambda/4$ shunted resonant line impedance Z_{ab}.

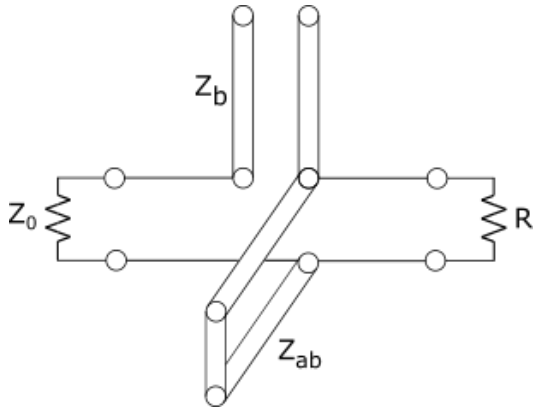

Figure B.1: Transmission line equivalent for the second order Marchand balun.

The procedure for determining the location of the nulls was discussed in Chapter 5. Setting $M_n(\theta, \theta_c) = 0$ and solving for θ results in (B.1) where $\theta = \theta_{n0}^i$ represents the ith null of an nth order balun. Fig. B.2 depicts the dependence of θ_{20}^1 versus B.

$$\theta_{20}^1 = \tan^{-1}[\sqrt{2}\tan(\theta_c)]. \tag{B.1}$$

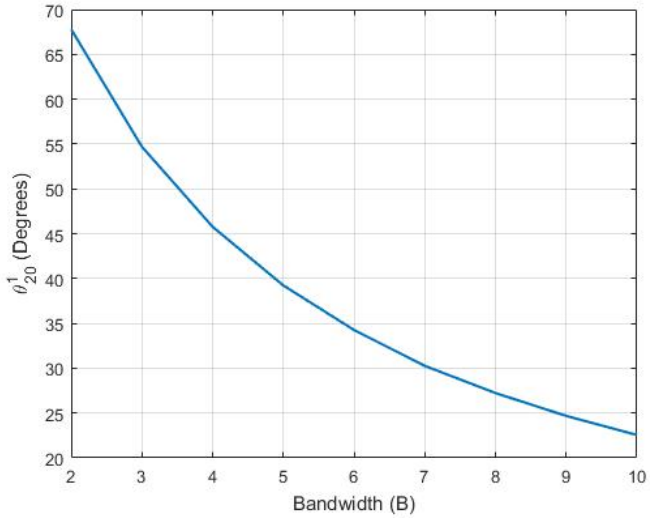

Figure B.2: Dependence of θ_{20}^1 vs. B

The closed-form expressions for the element values are as follows [46]:

$$z_{ab} = \frac{r}{\sqrt{2(r-1)}\tan(\frac{\pi}{B+1})}, \tag{B.2}$$

$$z_b = \frac{r}{z_{ab}}, \tag{B.3}$$

where B indicates the specified proportional bandwidth.

Third-order Marchand balun (Case A)

The transmission line equivalent circuit for the third order Marchand balun (Case A) is shown in Fig. B.3. It consists of a $\lambda/4$ open-circuit stub Z_b, the $\lambda/4$ shunted resonant line impedance Z_{ab} and the $\lambda/4$ transforming section Z_4.

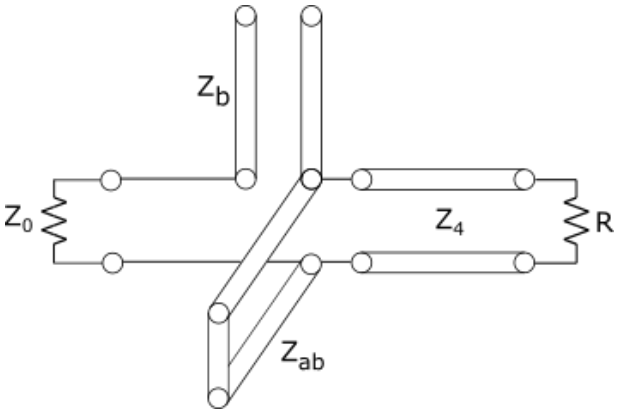

Figure B.3: Transmission line equivalent for the third order Marchand balun (Case A).

Unlike θ_{20}^1, which has a closed-form solution, θ_{30}^1 needs to be solved numerically. The dependence of θ_{30}^1 versus bandwidth is depicted in Fig. B.4.

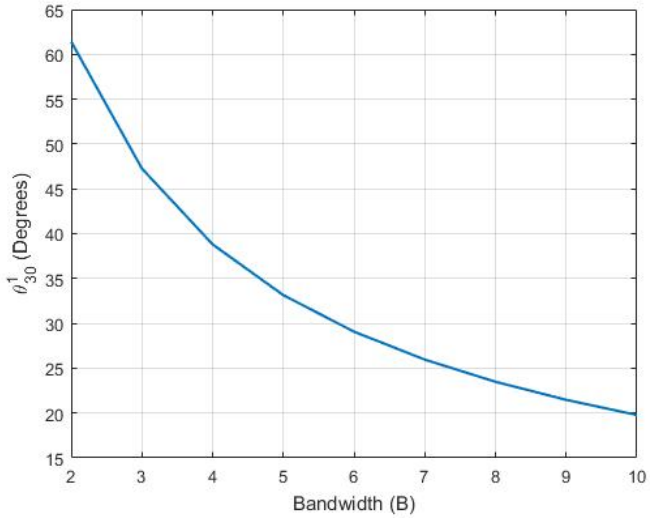

Figure B.4: Dependence of θ_{30}^1 vs. B

It is important to mention that the values of θ_{30}^1 obtained in Fig. B.4 are slightly different to those obtained by [46] as shown in Table B.1.

Table B.1: Comparison between θ_{30}^1 values.

B	θ_{30}^1(Degrees)	θ_{30}^1 (Degrees) [46]
2	61.42	63.71
4	38.81	41.28
6	29.07	30.83
8	23.49	24.58
10	19.78	20.61

The closed-form expressions for the element values are as follows [46]:

$$z_4 = \sqrt{r}, \tag{B.4}$$

$$z_{ab} = -b + \sqrt{b^2 + c}, \tag{B.5}$$

where b and c are given by

$$b = \sqrt{r}, \tag{B.6a}$$

$$c = \frac{r_{i4}^2 + x_{i4}^2}{(r_{i4} - 1)\tan^2\theta_{30}^1}, \tag{B.6b}$$

$$z_b = \frac{r_{i4}^2 + x_{i4}(x_{i4} + z_{ab}\tan\theta_{30}^1)}{r_{i4}^2 + (x_{i4} + z_{ab}\tan\theta_{30}^1)^2} z_{ab}\tan^2\theta_{30}^1, \tag{B.7}$$

$$r_{i4} = r\frac{1 + \tan^2\theta_{30}^1}{1 + r\tan^2\theta_{30}^1}, \tag{B.8a}$$

$$x_{i4} = \sqrt{r}(1 - r)\frac{\tan\theta_{30}^1}{1 + r\tan^2\theta_{30}^1}. \tag{B.8b}$$

Third-order Marchand balun (Case B)

The transmission line equivalent circuit for the third order Marchand balun (Case B) is shown in Fig. B.5. It consists of a $\lambda/4$ transforming section Z_1, the $\lambda/4$ open-circuit stub Z_b, the shunted resonant line impedance Z_{ab}.

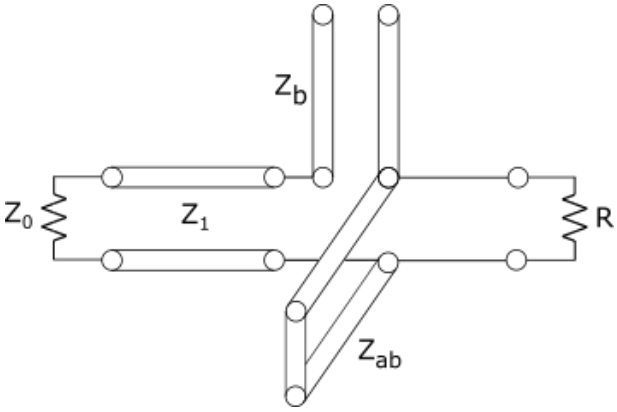

Figure B.5: Transmission line equivalent circuit for the third order Marchand balun (Case B).

The θ_{30}^1 values for Case A and Case B are the same. The second null is specified as $\theta_{30}^2 = \pi/2$ due to the inherent symmetry of the passband. The closed-form expressions for the element values are as follows [46]:

$$z_4 = \sqrt{r}, \tag{B.9}$$

$$z_{ab} = \frac{r}{\sqrt{r-1}\sin^2\theta_{30}^1}, \tag{B.10}$$

$$z_b = \frac{r^2 + z_{ab}\tan\theta_{30}^1}{r^2 + z_{ab}^2\tan^2\theta_{30}^1} z_{ab}\tan^2\theta_{30}^2 - x_{i1}\tan\theta_{30}^1. \tag{B.11}$$

Appendix C

Rectangular Coaxial Marchand Balun

C.1 Table of Design Parameters

Parameter List

Name	Expression	Value	Description	Type
d	1	1	Diameter of twin lines	Undefined
D_centres	2.106	2.106		Undefined
eps	eps0*eps_r	0.000000000018585		Undefined
eps0	8.85e-12	8.85e-12		Undefined
eps_r	2.1	2.1		Undefined
excess	0	0		Undefined
mu	100	100	Wavelength	Length
mu0	1.254e-6	1.254e-6		Undefined
psi	sqr(mu0/eps0)	376.423850538508		Undefined
psi_alt	sqr(mu0/eps)	259.757134971659		Undefined
r	2.5	2.5		Undefined
s	D_centres-d	1.106		Undefined
shield_thickness	0.035	0.035		Undefined
Z0	50	50	Characteristic Impedance of Z0	Undefined
Z0_a	Z0_b/exp(2*pi*Z0/psi)	0.65107915633812		Length
Z0_b	1.5	1.5		Length
Z0_length	5	5		Length
Z1	90	90	Characteristic Impedance of Z1	Undefined
Z1_a	Z1_b/exp(2*pi*Z1/psi)	0.333939519904271		Length
Z1_b	Z0_b	1.5		Length
Z1_length	mu/4	25		Undefined
Z1_thickness	0.1	0.1		Undefined
Z4	165	165	Characteristic Impedance of Z4	Undefined
Z4_length	mu/4	25		Undefined
Zab	137	137	Characteristic Impedance of ...	Undefined
Zab_a	Zb_b + Z1_thickness	1.6		Length
Zab_b	Zab_a * (10^((Zab/2)/138))* (...	4.6502398078701		Undefined
Zab_thickness	1.5	1.5	Thickness of outer conductor...	Length
Zb	104	104	Characteristic Impedance of Zb	Undefined
Zb_a	Z1_b/exp(2*pi*Zb/psi)	0.264350251362064		Length
Zb_b	Z0_b	1.5		Length
Zb_length	mu/4	25		Undefined

Figure C.1: Design I parameter list as seen in CST.

Parameter List

Name	Expression	Value	Description	Type
center_pin_length	10.02+1	11.02		Undefined
d	1	1	Diameter of twin lines	Undefined
D_centres	2.4237	2.4237		Undefined
eps	eps0*eps_r	0.000000000018585		Undefined
eps0	8.85e-12	8.85e-12		Undefined
eps_r	2.1	2.1		Undefined
excess	0	0		Undefined
length_support	0.99402660275669	0.99402660275669		Undefined
lid_1_thick	3.5	3.5		Undefined
mu	100	100	Wavelength	Length
mu0	1.254e-6	1.254e-6		Undefined
pin_diameter	1	1		Undefined
psi	sqr(mu0/eps0)	376.423850538508		Undefined
psi_alt	sqr(mu0/eps)	259.757134971659		Undefined
r	2.268074537875	2.268074537875		Undefined
s	D_centres-d	1.4237		Undefined
sleeve_diameter	2	2		Undefined
twin_lead_length	25.04012116508	25.04012116508		Undefined
Z0	50	50	Characteristic Impedan...	Undefined
Z0_a	Z0_b/exp(2*pi*Z0/psi)	0.987470053779482		Length
Z0_b	4.55/2	2.275		Length
Z0_length	5	5		Length
Z1	90	90	Characteristic Impedan...	Undefined
Z1_a	Z1_b/exp(2*pi*Z1/psi)	0.506474938521477		Length
Z1_b	Z0_b	2.275		Length
Z1_length	mu/4	25		Undefined
Z1_thickness	0.225	0.225		Undefined
Z4	165	165	Characteristic Impedan...	Undefined
Z4_length	mu/4	25		Undefined
Zab	127.6780471943	127.6780471943		Undefined
Zab_a	Zb_b + Z1_thickness	2.5		Undefined
Zab_b	(Zb_b + Z1_thickness) * ...	6.72233551093489		Undefined
Zab_thickness	1.5261873914713	1.5261873914713		Undefined
Zb	104	104	Characteristic Impedan...	Undefined
Zb_a	Z1_b/exp(2*pi*Zb/psi)	0.400931214565797		Length
Zb_b	Z0_b	2.275		Length
Zb_length	mu/4	25		Undefined

Figure C.2: Design II parameter list as seen in CST.